
Doctoral Dissertations

Student Theses and Dissertations

Fall 2012

Modeling multi-layer via structure using PEEC method

Hanfeng Wang

Follow this and additional works at: https://scholarsmine.mst.edu/doctoral_dissertations



Part of the [Electrical and Computer Engineering Commons](#)

Department: **Electrical and Computer Engineering**

Recommended Citation

Wang, Hanfeng, "Modeling multi-layer via structure using PEEC method" (2012). *Doctoral Dissertations*. 1973.

https://scholarsmine.mst.edu/doctoral_dissertations/1973

This thesis is brought to you by Scholars' Mine, a service of the Missouri S&T Library and Learning Resources. This work is protected by U. S. Copyright Law. Unauthorized use including reproduction for redistribution requires the permission of the copyright holder. For more information, please contact scholarsmine@mst.edu.

MODELING MULTI-LAYER VIA STRUCTURE USING PEEC METHOD

by

HANFENG WANG

A DISSERTATION

Presented to the Faculty of the Graduate School of the
MISSOURI UNIVERSITY OF SCIENCE AND TECHNOLOGY

In Partial Fulfillment of the Requirements for the Degree

DOCTOR OF PHILOSOPHY

in

ELECTRICAL ENGINEERING

2012

Approved by:

Jun Fan, Advisor
James Drewniak
Richard DuBroff
David Pommerenke
Daryl Beetner
Barbara Hale
Albert Ruehli

PUBLICATION DISSERTATION OPTION

This dissertation has been prepared in the form of three papers for publication.

The first paper consisting of pages 3 to 39 is Capacitance Calculation for Via Structures Using an Integral Equation Method Based on Partial Capacitance. This extended work has been submitted to IEEE Transaction on Microwave Theory and Techniques. The second paper consisting of pages from 40 to 89 is focused on the Surface PEEC Modeling for Shared-Antipad Via Structure Using Cavity Green's Function and Wave Port Excitation, and has been submitted to IEEE Transaction on Microwave Theory and Techniques. The third paper consisting of pages from 90 to 107 is Estimating Radio-Frequency Interference to an Antenna Due to Near-Field Coupling Using Divide-And-Conquer Method Based on Reciprocity, and is to be submitted to IEEE Transaction on Electromagnetic Compatibility.

ABSTRACT

In this dissertation, a new integral equation formulation for via structures is developed for the capacitance extraction between vias and planes. The proposed method can be used to calculate the shared-antipad via structure which is widely used in high-speed differential signal interconnects. In addition, we use the image theory to handle inhomogeneous media. Further, a new technique is given to reduce computational resources for via-to-plane structures based on properties of the matrix coefficient. The extracted capacitance is also incorporated into the physics-based circuit model to characterize the overall performance of the via transition.

In the second paper, a rigorous modeling of the shared-antipad via structure is developed using surface partial element equivalent circuit (PEEC). The cavity Green's function is used to evaluate the equivalent circuit elements, thereby requiring fewer cells for numerical computation. The non-orthogonal, quadrilateral cell is used in the mesh to better accommodate the non-rectangular shape of the via and the antipad. A novel wave port excitation method is applied to the equivalent circuit to obtain the network parameters of the via transition. The Z-parameters of the via structure are calculated using the proposed method, and the results are validated with the finite element solution obtained from commercial software.

In the third paper, an effective methodology is proposed to estimate the RF interference received by an antenna due to near-field coupling using divide-and-conquer based on reciprocity. The proposed methodology fits well with engineering practice, and is particularly suitable for pre-layout wireless system design and planning.

ACKNOWLEDGMENTS

I would like to thank my advisor, Dr. Jun Fan for his advice, guidance, and patience. Special thanks to my committee members, Dr. James Drewniak, Dr. Richard DuBroff, Dr. David Pommerenke, Dr. Daryl Beetner and Dr. Barbara Hale and Dr. Albert Ruehli for their time and effort in reviewing this dissertation.

I also would like to thank other lab members, Dr. Yaojiang Zhang, Dr. Victor Khilkevich, our former secretary Yvonne Hardesty, and all the other faculty and students for their collaboration, resilience, and hard work on the research projects and creating the good research and work environment in our lab.

My heartfelt gratitude goes to my parents and my wife for their support and encouragement towards achieving this goal.

TABLE OF CONTENTS

	Page
PUBLICATION DISSERTATION OPTION.....	iii
ABSTRACT.....	iv
ACKNOWLEDGMENTS.....	v
LIST OF ILLUSTRATIONS.....	x
LIST OF TABLES.....	xiii
 SECTION	
1. INTRODUCTION.....	1
 PAPER	
I. Capacitance Calculation for Via Structures Using an Integral Equation Method Based on Partial Capacitance.....	3
Abstract.....	3
I. INTRODUCTION.....	3
II. AXIALLY SYMMETRIC VIA GEOMETRIES	6
A. Geometry Definition and Mesh.....	6
B. Solution of Partial Capacitance.....	7
C. Evaluation of \mathbf{P}_s	9
III. AXIALLY ASYMMETRIC VIA GEOMETRIES	11
A. Geometry Definition and Mesh	11
B. Evaluation of \mathbf{P}_s	13
IV. DISCUSSIONS ON VIA-PLANE CAPACITANCE CALCULATION	16
A. Green's Function for Inhomogeneous Media.....	16

B. A Mesh Technique to Improve Computational Efficiency	18
V. RESULTS AND DISCUSSIONS	20
A. One Via Capacitance.....	20
B. Differential Vias Through A Plane with Shared-Antipad	21
C. Differential Vias Embedded in a Two Layer PCB.....	22
VI. INCORPORATION INTO PHYSICS-BASED CIRCUIT VIA MODEL.....	24
VII. CONCLUSIONS.....	26
APPENDICES.....	27
A. Integrals for Axially Symmetric Case	27
B. Integrals for Axially Asymmetric Case.....	34
REFERENCES.....	37
II. Surface PEEC Modeling for Shared-Antipad Via Structure Using Cavity Green's Function and Wave Port Excitation	40
Abstract.....	40
I. INTRODUCTION.....	40
II. FORMULATIONS.....	44
A. Equivalent Problem.....	44
B. Handling of Excitations.....	45
C. PEEC Formulations.....	45
D. Wave Port Excitation.....	51
III. GREEN'S FUNCTIONS.....	53
A. Spectral Representation of Cavity Green's Function	53
B. Fast Algorithm.....	54
C. Singularity Subtraction of Scalar Green's Function.....	56

D. Singularity Subtraction of Vector Green's Function.....	59
E. Derivative of Vector Green's Function.....	60
IV. RESULTS AND VALIDATIONS.....	61
V. CONCLUSIONS.....	68
APPENDICES.....	69
A. Non-Orthogonal Quadrilateral and Local Coordinates.....	69
B. Mesh Creation.....	73
C. Generate Capacitance Cells and Inductance Cells.....	75
D. Derivation of Equivalent Circuit Elements.....	77
E. Approximation Study.....	81
F. Create SPICE Netlist File.....	84
REFERENCES.....	87
III. Estimating Radio-Frequency Interference to an Antenna Due to Near-Field Coupling Using Divide-and-Conquer Method Based on Reciprocity.....	90
Abstract.....	90
I. INTRODUCTION.....	90
II. DIVIDE AND CONQUER METHOD	93
III. RECIPROCITY THEOREM AND INTERFERENCE ESTIMATION.....	95
IV. RESULTS AND VALIDATIONS.....	98
A. Simple Model.....	98
B. Trace+ PIFA.....	101
C. DECT + IC.....	104
V.CONCLUSIONS.....	106
ACKNOWLEDGMENT.....	107

REFERENCES.....	107
SECTION	
2. CONCLUSIONS.....	108
VITA.....	110

LIST OF ILLUSTRATIONS

Figure	Page
PAPER I	
1 Via going through a plane with illustration of a horizontal cell and a vertical cell.....	6
2 A typical shared-antipad differential via structure penetrating a horizontal plane.....	12
3 Mesh on the vertical surfaces of the vias	12
4 Mesh on the horizontal surfaces of the plane.....	13
5 Mutual coefficients between two arc cells.....	14
6 3-layer dielectric media problem with source in the middle layer.....	16
7 Multiple images of a source in the middle layer when the observation point is also located in the middle layer	17
8 Differential vias in a plane pair cavity.....	23
9 Test geometry of two differential vias in a 3-layered PCB	24
10 Physics-based circuit model for the test geometry.....	25
11 Comparison of differential return loss	26
12 Comparison of differential insertion loss.....	26
PAPER II	
1 Differential Via with shared-antipad inside plane pair cavities	42
2 Illustration of solving the local via region problem.....	44
3 Illustration of the non-orthogonal mesh on the via structure.....	47
4 Mesh for antipad generated using MATLAB.....	48
5 Electric equivalent circuit.....	50
6 Magnetic equivalent circuit.....	50
7 Illustration of magnetic current to electric voltage drop conversion.....	51

8 Create a parallelogram based on the observation point inside a quadrilateral.....	57
9 Illustration of vector definitions for the $1/R_p$ surface integral.....	58
10 Simple one via structure with circular antipad.....	62
11 Z-parameter comparison for one-via structure.....	63
12 Illustration of the differential voltage calculation for shared-antipad structure.....	65
13 Differential Z-parameter comparison for shared-antipad structure.....	66
14 Common Z-parameter comparison for shared-antipad structure.....	67
15 Local coordinates of a quadrilateral.....	70
16 Illustrations of different mesh density in the shared-antipad.....	74
17 Illustration of a quarter capacitance cell in a quadrilateral.....	75
18 Illustration of a half inductance cell in a quadrilateral.....	76
19 Distance to ratio definition.....	82
20 Illustration of naming rule of the inductance branch.....	84
21 Illustration of naming rule of the capacitance branch.....	86
PAPER III	
1 RF interference from digital units to analog units.....	91
2 Simplified model to illustrate the divide-and-conquer method	94
3 Divide the whole model into two parts.....	95
4 Output power comparison between the proposed method and the direct full-wave simulation for the simplified model shown in Fig. 2.....	101
5 Near-field coupling from a microstrip trace to a PIFA antenna.....	102
6 Output power comparisons between the proposed method and the direct method for the trace+PIFA structure shown in Fig. 5.....	103
7 Near-field coupling from an IC to a DECT antenna on a real printed circuit board ...	105
8 Detailed dimensions of the DECT antenna.....	105

9 Output power comparisons between the proposed method and the direct method for the DECT+IC structure shown in Fig.7.....106

LIST OF TABLES

Table	Page
PAPER II	
I Results Comparison for One Via Structure.....	62
II Results Comparison for Shared-Antipad Via Structure.....	65
PAPER III	
I Comparison of Friis Transformation, Full-wave Simulation, and the proposed divide-and-conquer method	99

1. INTRODUCTION

Vias are an important part of modern printed circuit boards (PCBs) since they are used to connect traces on different layers of the board. The vias represent discontinuities for the transmission line models of traces along signal paths. These discontinuities, in turn, cause frequency-dependent degradation and distortion of high-speed signals. The modeling and simulation of vias is therefore essential to correctly design today's high-speed circuit boards beyond 10Gbits/s.

Meanwhile, intra-System electromagnetic compatibility (EMC) problems are becoming increasingly common in mobile devices with radio frequency (RF)/wireless capabilities, such as notebook PCs and cell phones. With speeds increasing in the digital integrated circuits (ICs) and space decreasing on the printed circuit boards (PCBs) used in these compact mobile devices, the RF interference from the digital noise source (mostly from high speed ICs and traces) to the RF antenna becomes very critical in the system design process. Since the space between the digital circuits and the antenna in mobile devices is becoming extremely small, the traditional far-field theories may not work for the coupling study. The near-field coupling mechanism of the RF antenna needs to be studied.

This dissertation consists of three papers which focus on the above two topics. Paper 1 proposes a new integral equation formulation for via structures for the capacitance extraction between vias and planes. Paper 2 proposes a rigorous modeling of the shared-antipad via structure using surface partial element equivalent circuit (PEEC). Paper 3 proposes a method to estimate the noise voltage coupled to the RF antenna from the digital IC using the divide and conquer method together with the reciprocity theorem.

The primary contributions of this dissertation include:

A new integral equation formulation for via structures is developed in this paper for the capacitance extraction between vias and planes (paper 1).

Image theory is used to handle inhomogeneous media (paper 1).

A new technique is given to reduce computational resources for via-to-plane structures based on properties of the matrix coefficient (paper 1).

A rigorous modeling of the shared-antipad via structure is developed using surface partial element equivalent circuit (PEEC) (paper 2).

The cavity Green's function is used to evaluate the equivalent circuit elements which leads to much less cells needed in the numerical calculation (paper 2).

The non-orthogonal quadrilateral cell is used in the mesh to better accommodate the non-rectangular shape of the via and antipad (paper 2).

A novel wave port excitation method is applied to the equivalent circuit to obtain the network parameters of the via transition (paper 2).

A divide and conquer method together with the reciprocity theorem is used to estimate the near-field coupling from the digital IC to the RF antenna. A Huygens box, which divides the local region of the antenna and the rest of the system, is created to enclose the RF antenna (paper 3).

The method can be used in the RF interference estimation at the pre-design stage. The benefit of the proposed method is that if several antenna designs are available for the system, the system level simulation only needs to be done once, and the antenna design can be implemented based on the fields on the Huygens box. This makes the design process more flexible and efficient (paper 3).

PAPER

I. Capacitance Calculation for Via Structures Using an Integral Equation Method Based on Partial Capacitance

Hanfeng Wang, *Student Member, IEEE*, Siming Pan, Albert E. Ruehli, *Life Fellow, IEEE*, and

Jun Fan, *Senior Member, IEEE*

Abstract—A new integral equation formulation for via structures is developed in this paper for the capacitance extraction between vias and planes. The formulation is first developed for axially symmetric geometries and then extended to axially asymmetric geometries by changing the circular ring cells to arc cells. The extended method can be used to calculate the shared- antipad via structure which is widely used in high-speed differential signal interconnects. In addition, we use the image theory to handle inhomogeneous media. Further, a new technique is given to reduce computational resources for via-to-plane structures based on properties of the matrix coefficient. The proposed method is validated with a commercial finite element method based tool for several practical via structures. The extracted capacitance is also incorporated into the physics-based circuit model and validated with full wave simulations.

Index Terms— via-to-plane capacitance, integral equation method, shared-antipad, partial capacitance, image theory.

I. INTRODUCTION

Vias are an important part of modern printed circuit boards (PCBs) to connect traces on different layers. The vias represent discontinuities for the transmission lines along the signal paths. This causes frequency-dependent degradation and distortion for high-speed signals. The modeling and simulation of vias becomes essential to correctly design today's high-speed circuit boards beyond 10Gbits/s [1]. A physics-based circuit

model has recently been developed in [2][3] to analyze the via structure in a much more efficient way compared to traditional 3D full wave methods. Also, an equivalent transmission line model is further developed for the via structure based on the physics-based circuit model [4][5]. For all these via models, via-to-plane capacitances play an important role, to match the equivalent via impedance to the trace impedance. Thus, accurate via-to-plane capacitance evaluation is critical to guide engineering design and optimization.

Several methods have been developed to compute the via-to-plane capacitance. Commercial tools based on 3D finite element method (FEM) are commonly used to extract the via-to-plane capacitances for arbitrary via geometries. The disadvantage of these tools is that they are usually time and memory consuming. Analytical formulae have also been developed for the via-to-plane capacitance extraction in [6][7]. However, the analytical methods are limited to specific via geometries which are axially symmetric. Further, it is difficult to include important geometrical details like signal pads inside a plane pair cavity, etc. To bridge this gap between the analytical formulae and 3D FEM numerical solutions, the integral equation method based on partial capacitance method can be used. The partial capacitance method was developed in [8][9][14] for regular rectangular cells. The circular shape cells are first introduced in [10] to accommodate the circular shape of the via structure. With this, the via-to-plane capacitance for any arbitrary axially symmetric structures can be extracted accurately and efficiently. Further, the method in [10] has been extended to deal with axially asymmetric via geometries by changing the circular ring cells to arc cells in [11]. Using this method, the via-to-plane capacitance can be efficiently calculated for the shared-antipad geometry, which is

widely used in today's high-speed differential signal transitions [12]. The shared-antipad structure is used to increase the equivalent characteristic impedance of the via to match 100 Ohms differential trace impedance. The method in [11] can also be used to handle the offset via structures caused by manufacturing tolerance.

In this paper, the integral equation methods based on partial capacitance for both axially symmetric and axially asymmetric cases are summarized in Section II and Section III. In Section IV, we apply the image theory to extend the integral equation method with inhomogeneous media. We also consider the computation of the matrix coefficient for different sizes of conductors and propose an efficient mesh method. In Section V, via-to-plane capacitances for several examples are calculated using the proposed method. Further, the results are validated with the 3D FEM solutions. The compute time and possible ways to improve the efficiency are also discussed. Finally, in Section VI, the calculated via-to-plane capacitances are incorporated into the physics-based circuit via model and are validated with other 3D full-wave solutions. In summary, the main contributions of the paper are as follows.

- 1) The special ring cells are used for axially symmetric via geometries and arc cells are used for axially asymmetric via geometries. These shapes are more natural for via geometries. The integrals are solved semi-analytically based on these circular shapes.
- 2) Image theory is applied to the circular-cell based integral equation method and modified Green's function for inhomogeneous problems is developed.
- 3) A new technique is given to reduce computational resources for via-to-plane structures based on properties of the matrix coefficient.

4) The capacitance calculated using the proposed partial capacitance method is incorporated into the physics-based model to characterize the transition for differential vias in a shared-antipad structure.

II. AXIALLY SYMMETRIC VIA GEOMETRIES

A. Geometry Definition and Mesh

Fig. 1 shows an axially symmetric via structure with a via going through a plane. For this case where the conductors are axially symmetric, the charge distribution is also axially symmetric. The zero potential is assumed at infinity, and the potential on each conductor is constant. However, the charge distribution is highly non-uniform in the radial direction on the surface with a rotational symmetry. Ring cells are chosen to subdivide the conductor surfaces to take advantage of the axial symmetry of the charge distribution. The dashed lines illustrate the horizontal oriented cell and the solid lines illustrate the vertical oriented cell in Fig. 1.

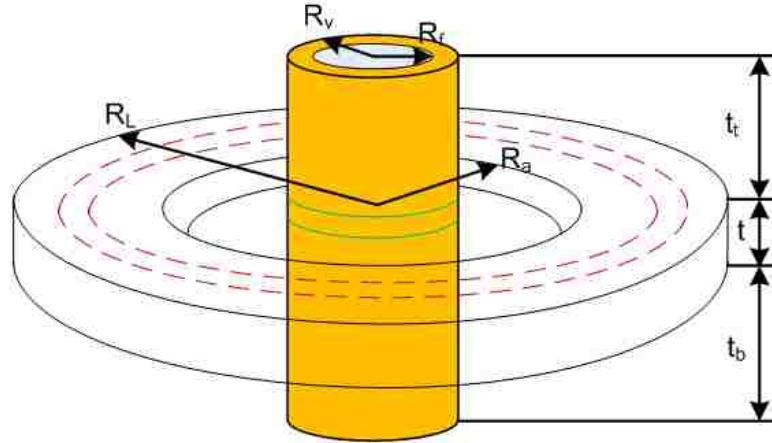


Fig. 1 Via going through a plane with illustration of a horizontal cell and a vertical cell

The so called short circuit capacitance [13] is defined in the following equation as,

$$\mathbf{Q} = \mathbf{C}_s \Phi, \quad (1)$$

where \mathbf{C}_s is the short circuit capacitance, \mathbf{Q} is the vector of total charge on each conductor; and Φ is the vector of potential of each conductor relative to infinity.

Therefore, for the two conductor case in Fig. 1, we have

$$\begin{bmatrix} Q_1 \\ Q_2 \end{bmatrix} = \begin{bmatrix} C_{s11} & C_{s12} \\ C_{s21} & C_{s22} \end{bmatrix} \begin{bmatrix} \Phi_1 \\ \Phi_2 \end{bmatrix}. \quad (2)$$

It is obvious that the via-to-plane capacitance can be evaluated by the following expression as,

$$C_{\text{via-to-plane}} = C_{s21} = \frac{Q_2}{\Phi_1} \text{ when } \Phi_2 = 0. \quad (3)$$

In other words, the plane is shorted to zero potential at infinity.

B. Solution of Partial Capacitance

The relationship between the charge density and the potential is given by the integral solution of Maxwell's equations as [14][15]

$$\Phi(\mathbf{r}) = \int G(\mathbf{r}, \mathbf{r}') q(\mathbf{r}') ds', \quad (4)$$

where q is the charge density on the conductor surfaces, and G is the free space Green's function given by

$$G(\mathbf{r}, \mathbf{r}') = \frac{1}{4\pi\epsilon_0} \frac{1}{|\mathbf{r} - \mathbf{r}'|}, \quad (5)$$

where \mathbf{r} and \mathbf{r}' are the position vectors of the source and observation points. The conductor surfaces are discretized into ring cells and the charge density in each ring cell is assumed to be constant, (4) can be re-written as

$$\Phi(\mathbf{r}) = \sum_j \frac{Q_j}{S_j} \int_{\text{cell}j} G(\mathbf{r}, \mathbf{r}') ds', \quad (6)$$

where Q_j represents the charge on the circular surface ring cell j and S_j is the area of that

cell. The total charge on each cell is used to avoid singular behaviour of the charge density at the edge of the conductor surfaces since Q_j is finite [14]. This improves the conditioning of the matrix resulting from Galerkin's method. Next, (6) can be written as

$$\Phi(\mathbf{r}) = \sum_j Q_j ps_j(\mathbf{r}), \quad (7)$$

where

$$ps_j(\mathbf{r}) = \frac{1}{S_j} \int_{cellj} G(\mathbf{r}, \mathbf{r}') ds'. \quad (8)$$

Finally, a similar method is used as in [14] to find all the charge on the cells by setting up a system of equations. In this Galerkin's approach, it is accomplished by matching the potential of each ring cell by averaging (8) over the surface of each ring cell, which can be expressed as

$$\Phi_i = Q_j ps_{ij}, \quad (9)$$

where

$$ps_{ij} = \frac{1}{S_j S_i} \int_{celli} \int_{cellj} G(\mathbf{r}, \mathbf{r}') ds' ds. \quad (10)$$

Assuming there are R ring cells, the system of equations with a size of R x R can be shown as,

$$\Phi = \mathbf{P}_s \mathbf{Q}_s, \quad (11)$$

where \mathbf{Q}_s is the vector of charge on all the conductor surface cells, Φ is the vector of potentials of the cells, and \mathbf{P}_s is the matrix of ps_{ij} terms. In the next subsection, the method to evaluate \mathbf{P}_s will be introduced so that the charge on the cells can be calculated and the short circuit capacitance can be obtained.

C. Evaluation of \mathbf{P}_s

The coefficient ps_{ij} in (10) involves surface integrals. The original form is a quadruple integral with double integrals either in the radial direction or longitudinal direction and double integrals in the angular direction. However, the double integrals in the angular direction can be simplified to a single integral since the cells are axially symmetric. Thus, the integral in (10) can be reduced to a triple integral as shown in the following paragraphs.

When i equals to j , the integrals are evaluated on the same surface cell. This corresponds to the diagonal terms in the \mathbf{P}_s matrix, which are called the self-integrals. In typical via geometry, two types of surface cells exist: vertical and horizontal ones. The vertical cell self-integral can be expressed as

$$ps_{ii} = \frac{1}{8\pi^2 \varepsilon_0 h^2} \int_0^h \int_0^h \int_0^{2\pi} \frac{d\phi' dz' dz}{\sqrt{2\rho^2(1 - \cos\phi') + (z - z')^2}}, \quad (12)$$

where ρ is the radius of the vertical cell and h is the height of the vertical cell.

The horizontal cell self-integral can be expressed as

$$ps_{ii} = \frac{1}{2\pi^2 \varepsilon_0 (b^2 - a^2)^2} \int_a^b \int_a^b \int_0^{2\pi} \frac{\rho' d\phi' d\rho' d\rho}{\sqrt{\rho^2 + \rho'^2 - 2\rho\rho' \cos\phi'}}, \quad (13)$$

where a is the inner radius and b is the outer radius of the horizontal cell. Both types of the self terms involve singularities in evaluating the integrals. However, by analytically carrying out integrations, the singularity behavior can be eliminated. For brevity, details are included in the Appendix.

In addition to the diagonal terms in the \mathbf{P}_s matrix, the off-diagonal mutual terms also need to be evaluated. There are three different types of mutual terms: vertical cell to vertical cell; horizontal cell to horizontal cell and horizontal cell to vertical cell.

For the vertical cell to vertical cell mutual term, the integral can be expressed as

$$p^{S_{ij}} = \frac{1}{8\pi^2 \varepsilon_0 h (l_2 - l_1)} \int_{l_1}^{l_2} \int_0^h \int_0^{2\pi} \frac{d\phi' dz' dz}{\sqrt{\rho^2 + \rho'^2 - 2\rho\rho' \cos \phi' + (z - z')^2}}, \quad (14)$$

where h is the height of the source cell and l_1, l_2 are the relative bottom and top elevations of the observation cell to the bottom elevation to the source cell; and, ρ' and ρ are the radii of the source and observation cells, respectively.

For the horizontal cell to horizontal cell mutual term, the integral can be expressed as

$$p^{S_{ij}} = \frac{1}{2\pi^2 \varepsilon_0 (b^2 - a^2)(d^2 - c^2)} \int_a^b \int_c^d \int_0^{2\pi} \frac{\rho\rho' d\phi' d\rho' d\rho}{\sqrt{\rho^2 + \rho'^2 - 2\rho\rho' \cos \phi' + (z - z')^2}}, \quad (15)$$

where a and b are the inner and outer radii of the observation cell; c and d are inner and outer radii of the source cell; z and z' are the z -coordinates of the observation and source horizontal cells, respectively.

For the horizontal cell to vertical cell mutual term, the integral can be expressed as

$$p^{S_{ij}} = \frac{1}{4\pi^2 \varepsilon_0 h (b^2 - a^2)} \int_a^b \int_0^h \int_0^{2\pi} \frac{\rho d\phi' dz' d\rho}{\sqrt{\rho^2 + \rho'^2 - 2\rho\rho' \cos \phi' + (z - z')^2}}, \quad (16)$$

where a and b are inner and outer radii of the horizontal cell; h is the height of the vertical cell; ρ' is the radius of the vertical cell; and, z is the relative elevation of the horizontal cell to the bottom of the vertical cell.

If the two ring cells are sufficiently far away, approximations can be used to simplify the integral of the mutual term. The first stage is to approximate the surface integral as a line integral. Then the mutual term is simplified to

$$pS_{ij} = \frac{1}{8\pi^2 \epsilon_0} \int_0^{2\pi} \frac{d\phi'}{\sqrt{\rho^2 + \rho'^2 - 2\rho\rho' \cos \phi' + (z - z')^2}}, \quad (17)$$

where ρ' and ρ are the center radii of the source and observation cells.

If the vertical distance between two cells is very large in comparison to the cell sizes, the two cells can be approximated as two points. Then the mutual term is simplified to

$$pS_{ij} = G(z, z'). \quad (18)$$

The mutual terms (14)-(17) can also be simplified from triple integrals to single integrals. By analytically carrying out some integrals, the single integrals are then solved numerically using a quadrature method. The details are again shown in the Appendix.

III. AXIALLY ASYMMETRIC VIA GEOMETRIES

A. Geometry Definition and Mesh

One axially asymmetric via structure is shown in Fig. 2 which is a shared-antipad geometry typical for differential signaling. The antipad is formed by two intersecting circular holes in the plane. Since the geometry is no longer axially symmetric, the charge distribution also varies along the azimuthal direction. Thus, the ring cells proposed in the previous section are not effective in this case. They are further divided into smaller arc cells along the angular direction. Then, the charge distribution is assumed to be uniform on each arc cell.

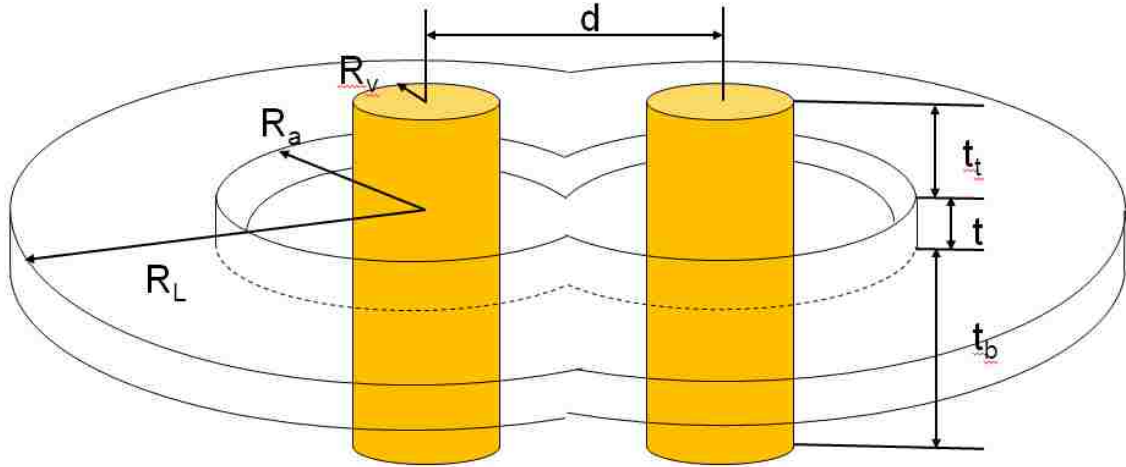


Fig. 2 A typical shared-antipad differential via structure penetrating a horizontal plane

The mesh on the vertical surface of the vias is shown in Fig. 3.

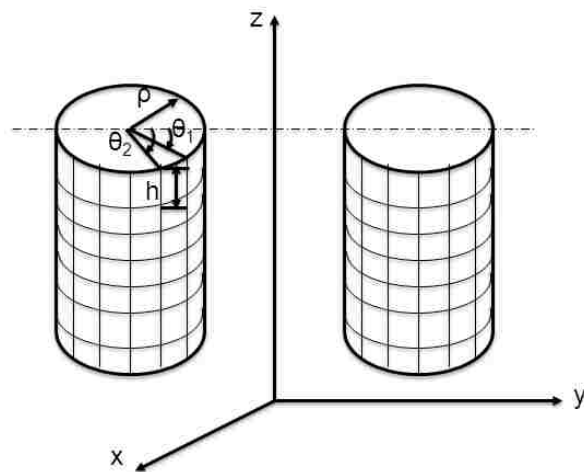


Fig. 3 Mesh on the vertical surfaces of the vias

The mesh for the horizontal surfaces of top and bottom for a finite-thickness plane is illustrated in Fig. 4. The mesh on the inner and outer vertical surfaces of the finite-thickness plane is similar to the one shown in Fig. 3.

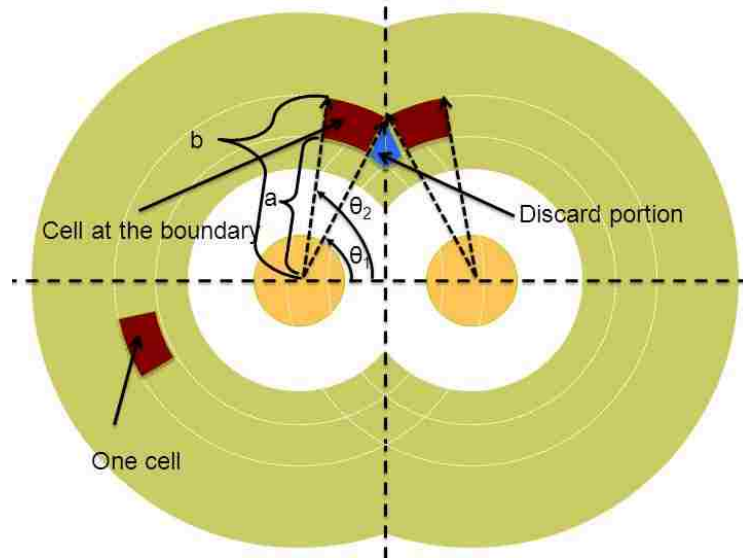


Fig. 4 Mesh on the horizontal surfaces of the plane

B. Evaluation of \mathbf{P}_s

The approach for handling the axially asymmetric case is the same as the one for the axially symmetric case. In other words, the same system of equations as (11) needs to be solved. Since arc cells are used for the axially asymmetric case, the expressions to evaluate the elements in the \mathbf{P}_s matrix are different, and quadruple integrals are needed to evaluate both diagonal (self) and off-diagonal (mutual) terms in the \mathbf{P}_s matrix.

The expression to evaluate the self term of a horizontal cell is shown as

$$p_{s_{ii}} = \frac{1}{\pi \epsilon_0 \theta^2 (b^2 - a^2)^2} \int_a^b \int_a^b \int_0^\theta \int_0^\theta \frac{\rho \rho' d\phi' d\phi d\rho' d\rho}{\sqrt{\rho^2 + \rho'^2 - 2\rho\rho' \cos(\phi - \phi')}} , \quad (19)$$

where a and b are the inner and outer radii of the horizontal cell; and, θ is the angle of the arc cell relative to the center.

The expression for the self term of a vertical cell is similarly shown as

$$p_{s_{ii}} = \frac{1}{4\pi \epsilon_0 \theta^2 h^2} \int_0^h \int_0^h \int_0^\theta \int_0^\theta \frac{d\phi' d\phi dz' dz}{\sqrt{2\rho^2 [1 - \cos(\phi - \phi')] + (z - z')^2}} , \quad (20)$$

where h and ρ are the height and radius of the vertical arc cell, respectively; and, θ is the angle of the arc cell relative to the center. Both (19) and (20) involve singularities.

However, they can be eliminated by analytically carrying out the two integrals over either the radial direction or the longitudinal direction. The details can be found in the Appendix.

The mutual terms in the Ps matrix also have three different kinds. In many cases, the arc cells are not concentric. Thus, a new parameter d , for the offset between the centers of the two cells as illustrated in Fig. 5, needs to be added into the expressions for the mutual terms. The distance between the source and observation points can be obtained using the cosine law twice as

$$L(\rho, \rho', \phi, \phi', d) = |\bar{r} - \bar{r}' + \bar{d}| = \sqrt{\rho^2 + \rho'^2 - 2\rho\rho'\cos(\phi' - \phi) - 2d(\rho\cos\phi - \rho'\cos\phi') + d^2}. \quad (21)$$

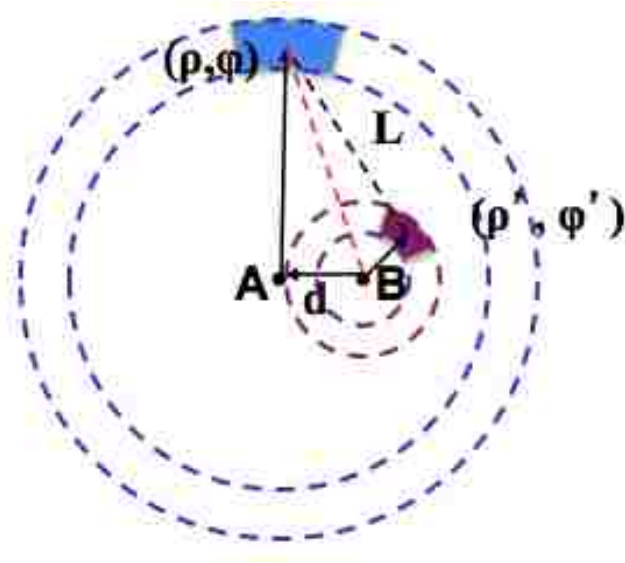


Fig. 5 Mutual coefficients between two arc cells

The expression for the mutual coefficient between two vertical cells is

$$pS_{ij} = \frac{1}{4\pi\epsilon_0 h(l_2 - l_1)(\theta_2 - \theta_1)(\theta_4 - \theta_3)} \int_{l_1}^{l_2} \int_0^h \int_{\theta_1}^{\theta_2} \int_{\theta_3}^{\theta_4} \frac{d\phi d\phi' dz' dz}{\sqrt{L^2 + (z - z')^2}}, \quad (22)$$

where h is the height of the source cell; l_1 and l_2 are the bottom and top z -coordinates of the observation cell relative to the bottom of the source cell.

The expression for the mutual term between two horizontal cells is

$$p^{S_{ij}} = \frac{1}{\pi\epsilon_0(\theta_2 - \theta_1)(\theta_4 - \theta_3)(b^2 - a^2)(d^2 - c^2)} \int_a^b \int_c^f \int_{\theta_1}^{\theta_2} \int_{\theta_3}^{\theta_4} \frac{\rho\rho' d\phi d\phi' d\rho' d\rho}{\sqrt{L^2 + (z - z')^2}}, \quad (23)$$

where a and b are the inner and outer radii of the source cell; and, c and f are the inner and outer radii of the observation cell.

The expression for the mutual term $p^{S_{ij}}$ between a vertical and a horizontal cell is

$$p^{S_{ij}} = \frac{1}{2\pi\epsilon_0 h(b^2 - a^2)(\theta_2 - \theta_1)(\theta_4 - \theta_3)} \int_a^b \int_0^h \int_{\theta_1}^{\theta_2} \int_{\theta_3}^{\theta_4} \frac{\rho d\phi d\phi' dz' d\rho}{\sqrt{L^2 + (z - z')^2}}, \quad (24)$$

where h is the height of the vertical cell; ρ is the radius of the vertical cell; a and b are the inner and outer radii of the horizontal cell.

In (22)~(24), θ_1 , θ_2 , θ_3 , and θ_4 represent the starting and ending angles of the source and observation cells. The integrals over the non-angular variables (ρ , ρ' , z , z') in (22) and (24) can be carried out analytically and the remaining ones are calculated numerically. In (23), only the integral over ρ can be carried out analytically and the rest has to be calculated numerically. The efficiency of the proposed method is limited by this triple numerical integration.

Similar as in the axially symmetric case, if the two arc cells are sufficiently far away from each other, both cells can be approximated as points. Then, the integral is simplified to the point-to-point approximation as

$$p^{S_{ij}} = \frac{1}{4\pi\epsilon_0} \frac{1}{|\mathbf{r} - \mathbf{r}'|}, \quad (25)$$

where \mathbf{r} and \mathbf{r}' are the position vectors of the centers of the source and observation cells. This leads to a significant speed-up in the computation of the coefficients.

IV. DISCUSSIONS ON VIA-PLANE CAPACITANCE CALCULATION

A. Green's Function for Inhomogeneous Media

The above derivations are all based on the free space Green's function, which is only valid for a homogeneous dielectric medium. In practical PCB designs, inhomogeneous media are usually involved. Assuming the dielectric materials in a multilayer PCB have approximately the same properties, a typical via structure involves the 3-layer dielectric media, as illustrated in Fig. 6, with the PCB dielectric material in the middle and air in the top and bottom. The Green's function for this layered media can be derived from the free space Green's function using the image theory [16].

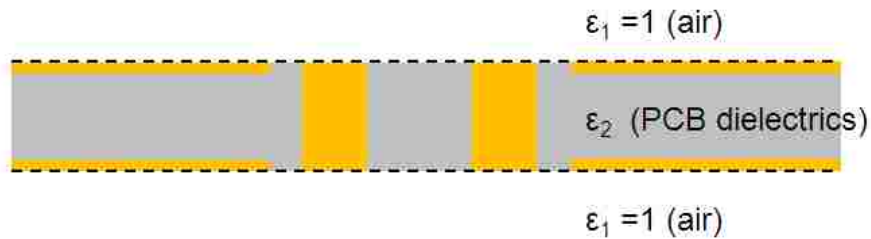


Fig. 6 3-layer dielectric media problem with source in the middle layer

For the middle layer, the original problem is equivalent to a homogeneous problem with infinite number of images of the original source, as illustrated in Fig. 7.

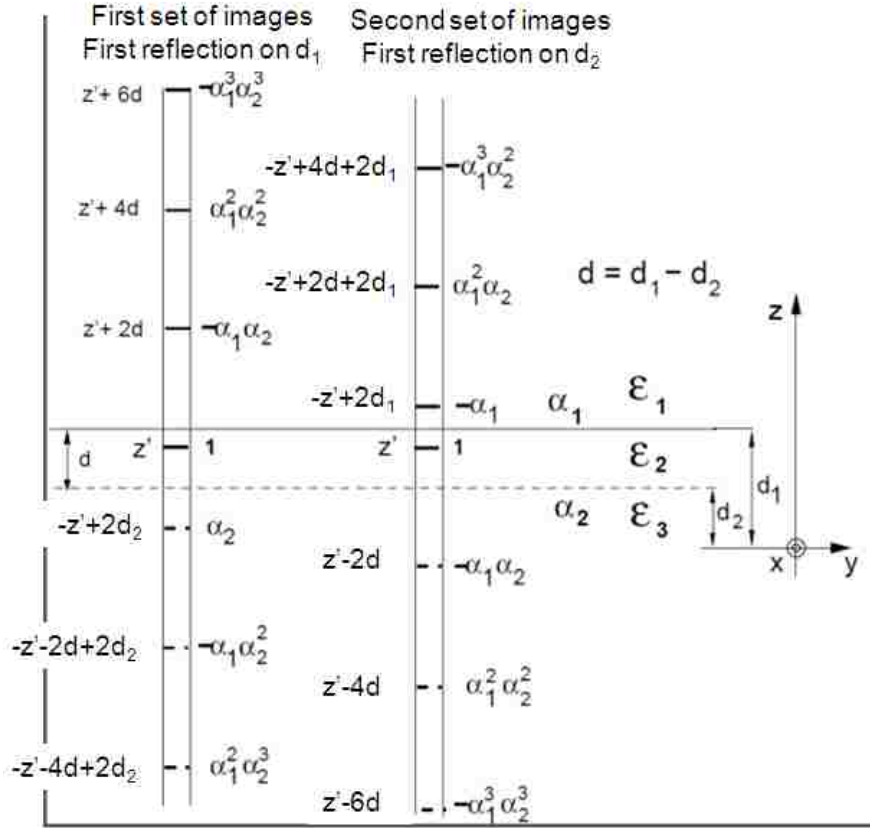


Fig. 7 Multiple images of a source in the middle layer when the observation point is also located in the middle layer

Theoretically, infinite number of the images need to be included in the modified Green's function as

$$G(r, r') = \frac{1}{4\pi\epsilon_2} \frac{1}{R(z, z')} + \frac{1}{4\pi\epsilon_2} \sum_{n=0}^{\infty} \left\{ \begin{array}{l} \alpha^{1+2n} \left[\frac{1}{R(z, -z'+2d_1+2nd)} + \frac{1}{R(z, -z'+2d_2-2nd)} \right] \\ + \alpha^{2+2n} \left[\frac{1}{R(z, z'-2(n+1)d)} + \frac{1}{R(z, z'+2(n+1)d)} \right] \end{array} \right\}, \quad (26)$$

where $\alpha = \frac{\epsilon_2 - \epsilon_1}{\epsilon_2 + \epsilon_1}$ is the coefficient of the first image, and $R(z, x)$ represents the distance

between the source or image of the source and the observation point, which is located in the middle layer. The expression involves an infinite summation. However, as the distance between the image and the observation point becomes sufficiently large, the

image term can be ignored. As a result, only a few terms are needed to evaluate the modified Green's function. For most cases, choosing $n \leq 1$ is sufficient for the result to converge.

B. A Mesh Technique to Improve Computational Efficiency

Once the \mathbf{P}_s matrix with all the elements is obtained through the methods discussed in Sections II and III, the via-to-plane capacitances can be calculated using (1) by assuming all the cells in each conductor have the same potential. Let's assume there are m conductors, and conductor i ($i = 1, 2, \dots, m$) is discretized into n_i cells. Further, the cells are numbered in such a way that the first n_1 cells are those on the surface of conductor 1, followed by the n_2 cells on conductor 2, and so on. Then, the short circuit capacitance equation (1) for this m -conductor system becomes

$$\mathbf{Q}_{m \times 1} = \mathbf{A}' \mathbf{P}_s^{-1} \mathbf{A} \Phi_{m \times 1}, \quad (27)$$

where

$$\mathbf{A} = \begin{bmatrix} \mathbf{1}_{n_1 \times 1} & \mathbf{0} & \mathbf{0} & \mathbf{0} \\ \mathbf{0} & \mathbf{1}_{n_2 \times 1} & \mathbf{0} & \mathbf{0} \\ \mathbf{0} & \mathbf{0} & \dots & \mathbf{0} \\ \mathbf{0} & \mathbf{0} & \mathbf{0} & \mathbf{1}_{n_m \times 1} \end{bmatrix}, \quad (28)$$

$\mathbf{1}_{n_i \times 1}$ is an $n_i \times 1$ vector with all the elements equal to 1, and $i = 1, 2, \dots, m$.

The computational complexities as a function of the total number of cells N ($N = \sum_{i=1}^m n_i$) are $O(N^2)$ to generate the elements in the \mathbf{P}_s matrix, and $O(N^3)$ to obtain the short circuit capacitance matrix $\mathbf{A}' \mathbf{P}_s^{-1} \mathbf{A}$, respectively. Therefore, reducing the total number of cells can significantly improve the computational efficiency. The sizes of the

mesh cells should be determined in such a way that the charge distribution does not change much on each cell. Otherwise, smaller cell sizes are necessary.

Let's focus on the via structure under study in this paper. Assuming the m^{th} conductor is a large plane, the potential of this metal plane can be derived from (27) and (28) as

$$\Phi_{plane} = -\sum_{i=1}^{m-1} \frac{(\sum_{j=1}^{n_i} \sum_{k=1}^{n_i} [\mathbf{C}_{ii}]_{jk} + \sum_{j=1}^{n_m} \sum_{k=1}^{n_i} [\mathbf{C}_{mi}]_{jk})}{(\sum_{j=1}^{n_m} \sum_{k=1}^{n_m} [\mathbf{C}_{mm}]_{jk} + \sum_{j=1}^{n_i} \sum_{k=1}^{n_m} [\mathbf{C}_{im}]_{jk})} \Phi_i, \quad (29)$$

where Φ_i is the potential on conductor i , and

$$\mathbf{P}_s^{-1} = \begin{bmatrix} [\mathbf{C}_{11}]_{n_1 \times n_1} & \cdot & [\mathbf{C}_{1i}]_{n_1 \times n_i} & [\mathbf{C}_{1m}]_{n_1 \times n_m} \\ \cdot & \cdots & \cdot & \cdot \\ [\mathbf{C}_{i1}]_{n_i \times n_1} & \cdot & [\mathbf{C}_{ii}]_{n_i \times n_i} & [\mathbf{C}_{im}]_{n_i \times n_m} \\ [\mathbf{C}_{m1}]_{n_m \times n_1} & \cdot & [\mathbf{C}_{mi}]_{n_m \times n_i} & [\mathbf{C}_{mm}]_{n_m \times n_m} \end{bmatrix}. \quad (30)$$

In the derivation of (29), the total charge of the m -conductor system is assumed to be zero.

When the plane is much larger than all other conductors, and the mutual capacitive coupling between the plane and other conductors is relatively small (both are true for typical via structures in printed circuit boards), the following relationship is valid as

$$(\sum_{j=1}^{n_m} \sum_{k=1}^{n_m} [\mathbf{C}_{mm}]_{jk} + \sum_{j=1}^{n_i} \sum_{k=1}^{n_m} [\mathbf{C}_{im}]_{jk}) \gg (\sum_{j=1}^{n_i} \sum_{k=1}^{n_i} [\mathbf{C}_{ii}]_{jk} + \sum_{j=1}^{n_m} \sum_{k=1}^{n_i} [\mathbf{C}_{mi}]_{jk}), \quad (31)$$

which results in

$$\Phi_{plane} \approx 0. \quad (32)$$

Thus, the large metal plane can be inherently considered as “Ground” as the potential for the large metal plane is approximately zero, but only with respect to the

electrostatic field. Then, the total charge on each of the other conductors can be represented as

$$Q_i = \sum_{j=1}^{m-1} (\Phi_j \sum_{p=1}^{n_i} \sum_{q=1}^{n_j} [C_{ij}]_{pq}), \quad i = 1, 2, \dots, m-1. \quad (33)$$

It can be clearly seen in (33) that the total charge on conductor i ($i \neq m$) is not related to the cell number nm of the large metal plane if the potential of the plane is approximately zero. In other words, the mesh density on the large metal plane has little impact on the calculated charge values, and thus the final via-to-plane capacitance values. Therefore, only very few cells are needed on the large metal plane in the structure under study in this paper. This proposed mesh technique can significantly improve the computational efficiency of the proposed methods

V. RESULTS AND DISCUSSIONS

A. One Via Capacitance

The via-to-plane capacitance is calculated based on the method proposed in Section II for the axially symmetric geometry shown in Fig. 1 and the result is compared with the capacitance extracted by Q3D from Ansys [17].

The via structure is embedded in the air. The via outer radius R_v is 9 mils while the inner radius R_f is 7.2 mils. The plane inner radius R_a is 23 mils, which is also called the antipad radius, while outer radius R_L is 100 mils. The top and bottom portions (t_t , t_b) of the via separated by the plane are 8 mils and 10 mils, respectively. The plane has a thickness (t) of 1 mil.

The via-to-plane capacitance calculated by the proposed method is 41.0 fF while Q3D gives the result of 41.1 fF with a relative difference of 0.25%. The computational time of the proposed method is only 1.6 seconds compared to 19 seconds using Q3D.

The main advantage of the proposed method is that it needs very few cells to get a good result. Only 20 ring cells are assigned to the vertical surfaces of the via and only 5 ring cells are assigned to the horizontal surfaces of the plane. For the thin surfaces, like the top and bottom via surfaces and the side surfaces of the plane, only one ring cell is needed for each surface.

B. Differential Vias Through A Plane with Shared-Antipad

The via geometry shown in Fig. 2 is used to validate the proposed method for axially asymmetric case. In the example, the via structure is assumed to be embedded in the air.

The radius of both vias R_v is 9 mils, and the pitch size d between the two vias (center-to-center) is 40 mils. The antipad region is formed by two intersecting holes with a radius R_a of 30 mils each. The size of the plane is not too critical for the capacitance calculations as long as it is sufficiently large. In this example, we assume that the shape is the same as the antipad formed by two intersection circles with a radius R_L of 100 mils each. The plane thickness t is 1 mil. The via portions above the plane (t_t) are 8 mils long, while the via portions below the plane (t_b) are 10 mils.

All the metal surfaces of the vias and the plane in the geometry are supposed to be meshed into arc cells. However, only the outer surfaces of the vias, the inner vertical as well as the horizontal surfaces of the plane are critical in the via-to-plane capacitance calculations since most of the E-field lines terminate on these surfaces. Thus, only these

critical surfaces are included in the calculation, which does improve calculation efficiency while preserving the accuracy of the result.

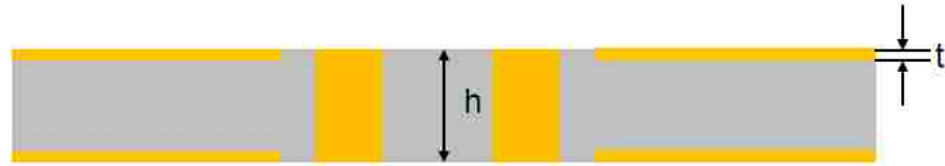
Similar to the axially symmetric case, very few cells are needed to converge to a result for this shared-antipad geometry. Totally 6 x 6 cells (6 in the z-direction and 6 in the angular direction) are used on the outer surface of each via. On the top and bottom surfaces of the plane, 6 x 3 cells (6 in the angular direction and 3 in the radial direction) are used in each half of the plane. The inner surface of the plane is segmented into 6 cells in the angular direction in each of the left and the right portions.

The calculated capacitance of the proposed method is 30.0 fF, while the Q3D gives the result of 30.6 fF. The relative difference is less than 2%. The simulation time of Q3D is 17 seconds, while the simulation time of the proposed method is only 9 seconds on the same dual core, 3 GB memory machine.

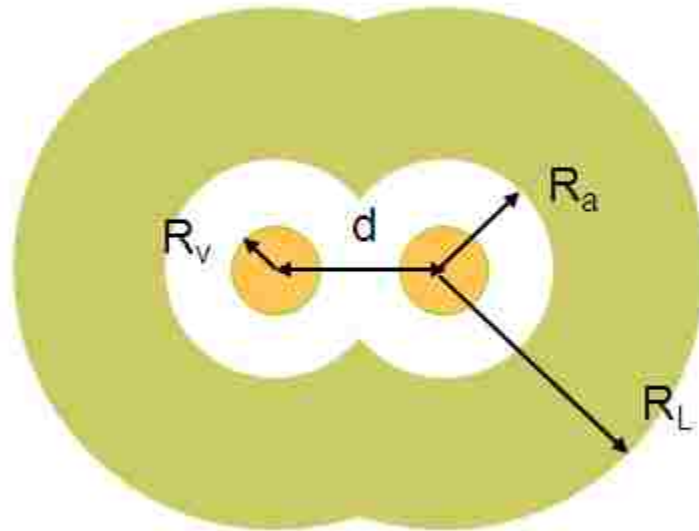
We exploit the symmetry of the geometry in the evaluation of the \mathbf{P}_s matrix so that only about a quarter of the matrix terms need to be calculated using the integrals in the Appendix. Further cell number reduction can be done on the plane surfaces based on the discussion in Section B. If only 4 cells are assigned on each surface of the planes (1 cell in radial direction and 2 cells in angular direction on each half of the plane), the calculation time is only 4.2 seconds and the via-to-plane capacitance is still 30.0 fF.

C. Differential Vias Embedded in a Two Layer PCB

A more realistic case is shown in Fig. 8, which involves a pair of differential vias in a plane pair cavity.



(a) side view



(b) Top view

Fig. 8 Differential vias in a plane pair cavity

The via-to-plane capacitance for this inhomogeneous problem is calculated using the combination of the method in Section III and the image method proposed in Section A. The dimensions of the vias and plane are exactly the same as in the previous example except the via length h is 19.5 mils. The material of the dielectric layer between the two planes is assigned to be FR-4 which has a permittivity of 4.4. We assume that media above and below the PCB structure are air. The mesh remains the same as in the previous example.

The calculated capacitance using our proposed method is 47.4 fF, compared to the Q3D result of 48.0 fF. The relative difference is less than 2%. The computational time of

the proposed method is 13 minutes 20 seconds, while Q3D takes 27 minutes 29 seconds. Since the two planes and two vias have the exact same shape and meshing, quite a lot of terms in the \mathbf{P}_s matrix are evaluated redundantly. More careful programming may lead to further time saving for the proposed method.

As mentioned in Section III, the most time consuming part is the evaluation of the triple numerical integral in (23). Thus, if this numerical integral can be solved more efficiently, the overall efficiency of the proposed method will improve dramatically. Memory cost of the proposed method is also much smaller since only a small number of cells are needed for this integral equation based method.

VI. INCORPORATION INTO PHYSICS-BASED CIRCUIT VIA MODEL

In this section, the extracted via-to-plane capacitance is incorporated into the physics based via model [2][3] to obtain the S-parameters which describe the via transition in a multi-layer PCB. The test via structure is shown in Fig. 9 with two ports set at the top and bottom antipad regions. The screenshot of HFSS is captured in Fig. 9 and the dotted pattern illustrates the wave port defined between the vias and the plane.

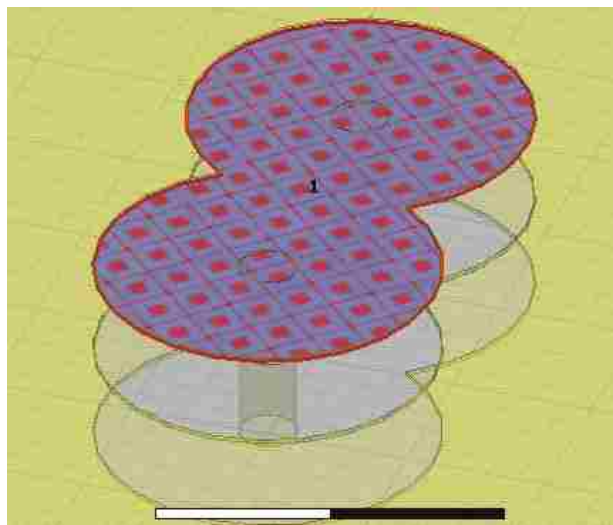


Fig. 9 Test geometry of two differential vias in a 3-layered PCB

There are 3 conductor layers forming two cavities in the test via structure. The permittivity of the dielectric is 4.0. The radius of the via is 5 mils; the pitch between two vias is 50 mils. Two circles with a radius of 30 mils each intersect and form the shared-antipad structure. The plane thickness is 0.7 mils, and the lengths of the top and bottom cavities are 15.77 mils and 16.27 mils, respectively.

The above geometry is modeled as a physics-based circuit and also simulated using a full wave method. Port definitions of the corresponding physics-based via model are shown in Fig. 10.

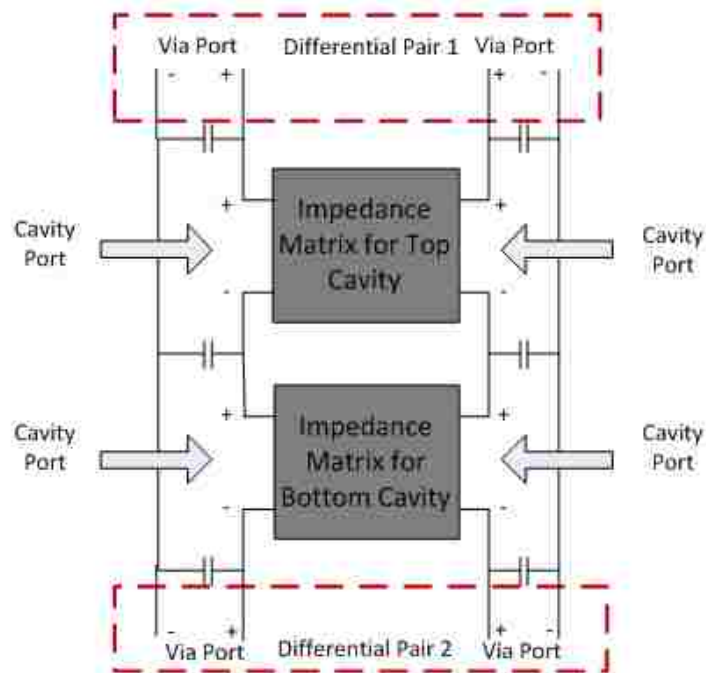


Fig. 10 Physics-based circuit model for the test geometry

The capacitances in the circuit model above are calculated by the proposed methods. The capacitance values are 31.0 fF, 31.5 fF and 43.6 fF, for the capacitances between the via to top, bottom and middle planes. The S-parameter results of the physics-

based circuit model are then compared with the full wave simulation done by HFSS from Ansys, in Fig.11 and Fig.12. The results show a good correlation up to 20GHz.

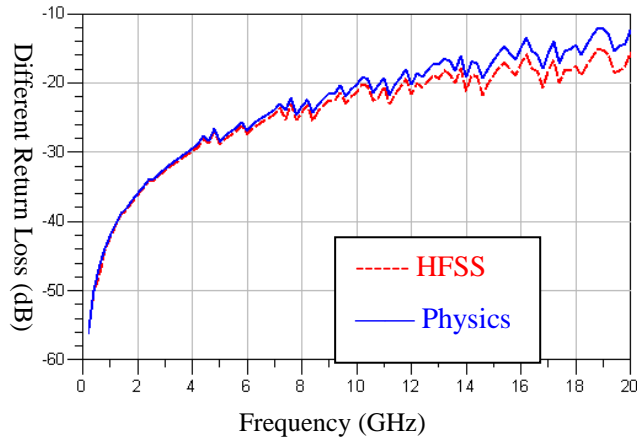


Fig.11. Comparison of differential return loss

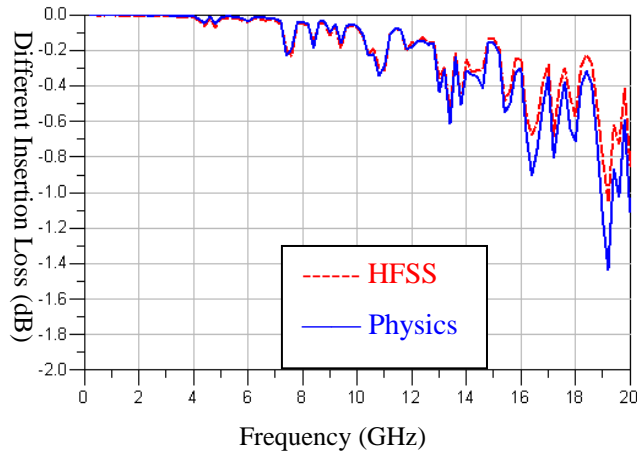


Fig.12. Comparison of differential insertion loss

VII. CONCLUSIONS

An integral equation method based on partial capacitance is introduced in this paper to calculate the via-to-plane capacitance of different via structures. The axially symmetric structure is analysed first and then the method is extended to the axially asymmetric via geometry. The image theory is used to deal with the inhomogeneous

dielectric media which is common for PCB applications. The via-to-plane capacitances are extracted for several different via geometries and the results are validated with the finite element solution using Q3D. The accuracy of the proposed method is also validated through the comparison of the physics-based via modeling and the full wave simulation.

The main advantage of the proposed capacitance calculation method is that very few mesh cells are needed which leads to a low computational time and memory cost. The computational efficiency of the proposed method can be further improved by increasing the speed of evaluation of the numerical triple integral in (24).

APPENDICES

A. Integrals for Axially Symmetric Case

1) Self Term for Vertical Cells

The final solution of (12) for the self term of a vertical cell is shown as

$$ps_{ii} = \frac{1}{2\pi^2 \epsilon_0 h^2} \left[2h \int_0^{\pi/2} \ln \left(h + \sqrt{h^2 + 4\rho^2 \sin^2 \theta} \right) d\theta - 2\sqrt{h^2 + 4\rho^2} E \left(\frac{2\rho}{\sqrt{h^2 + 4\rho^2}} \right) + 4a - \pi h \ln \rho \right], \quad (34)$$

where $E(x)$ is the complete elliptical integral of the second kind. There is still one more integral which needs to be evaluated numerically. The singularity is already removed in the final (34).

The detailed derivation is shown as

$$\begin{aligned}
pS_{ii} &= \frac{1}{S_i S_i} \int \int G(\mathbf{r}, \mathbf{r}') ds' ds = \frac{1}{8\pi^2 \epsilon_0 h^2} \int_0^h \int_0^h \int_0^{2\pi} \frac{d\phi' dz' dz}{\sqrt{\rho^2 + \rho'^2 - 2\rho\rho' \cos \phi' + (z - z')^2}} \\
&= A_{coef} \int_0^h \int_0^h \int_0^{2\pi} \frac{d\phi' dz' dz}{\sqrt{w^2 + (z - z')^2}} \quad (w^2 = \rho^2 + \rho'^2 - 2\rho\rho' \cos \phi') \\
&= A_{coef} \int_0^{2\pi} \int_0^h \left[\ln \left((h - z') + \sqrt{(h - z')^2 + w^2} \right) - \ln \left(-z' + \sqrt{z'^2 + w^2} \right) \right] dz' d\phi' \\
&= A_{coef} \int_0^{2\pi} \left\{ \left[x \ln \left(x + \sqrt{x^2 + w^2} \right) - \sqrt{x^2 + w^2} \right] \Big|_0^h - \left[y \ln \left(y + \sqrt{y^2 + w^2} \right) - \sqrt{y^2 + w^2} \right] \Big|_{-h}^0 \right\} d\phi' \\
&\quad (x = h - z' \quad y = -z') \\
&= A_{coef} \int_0^{2\pi} \left\{ \left[h \ln \left(h + \sqrt{h^2 + w^2} \right) - \sqrt{h^2 + w^2} + w \right] - \left[-w + h \ln \left(-h + \sqrt{h^2 + w^2} \right) + \sqrt{h^2 + w^2} \right] \right\} d\phi' \\
&= A_{coef} \int_0^{2\pi} \left\{ \left[h \ln \left(\frac{h + \sqrt{h^2 + w^2}}{-h + \sqrt{h^2 + w^2}} \right) - 2\sqrt{h^2 + w^2} + 2w \right] \right\} d\phi' \\
&= 4A_{coef} \int_0^\pi \left\{ \left[h \ln \left(h + \sqrt{h^2 + w^2} \right) - \sqrt{h^2 + w^2} + w \right] - h \ln w \right\} d\phi'
\end{aligned}$$

The four terms of the integrand can be further derived as

$$\begin{aligned}
\int_0^\pi h \ln \left(h + \sqrt{h^2 + w^2} \right) d\phi' &= h \int_0^\pi \ln \left(h + \sqrt{h^2 + 2a^2 (1 - \cos \phi')} \right) d\phi' \\
&= 2h \int_0^{\pi/2} \ln \left(h + \sqrt{h^2 + 4a^2 \sin^2 \theta} \right) d\theta \\
\int_0^\pi \sqrt{h^2 + w^2} d\phi' &= \int_0^\pi \sqrt{h^2 + 2a^2 (1 - \cos \phi')} d\phi' = 2 \int_0^{\pi/2} \sqrt{h^2 + 4a^2 \sin^2 \theta} d\theta \\
&= 2 \int_0^{\pi/2} \sqrt{h^2 + 4a^2 - 4a^2 \sin^2 \theta} d\theta = 2\sqrt{h^2 + 4a^2} \int_0^{\pi/2} \sqrt{1 - \frac{4a^2}{h^2 + 4a^2} \sin^2 \theta} d\theta \\
&= 2\sqrt{h^2 + 4a^2} E \left(\frac{2a}{\sqrt{h^2 + 4a^2}} \right) \\
\int_0^\pi w d\phi' &= \int_0^\pi \sqrt{2a^2 (1 - \cos \phi')} d\phi' = 2 \int_0^{\pi/2} 2a \sin \theta d\theta = 4a \\
h \int_0^\pi \ln w d\phi' &= h \int_0^\pi \ln \sqrt{2a^2 (1 - \cos \phi')} d\phi' = h \int_0^{\pi/2} \ln [4a^2 \sin^2 \theta] d\theta \\
&= 2h \int_0^{\pi/2} \ln [2a \sin \theta] d\theta = 2h \left[\frac{\pi}{2} \ln (2a) + \int_0^{\pi/2} \ln [\sin \theta] d\theta \right] = \pi h \ln a
\end{aligned}$$

where $\rho = \rho' = a$.

2) Self Term for Horizontal Cells

The final solution of (13) for the self term of a horizontal cell is shown as

$$p^{S_{ii}} = \frac{1}{2\pi^2 \varepsilon_0 (b^2 - a^2)^2} \int_0^{2\pi} \left\{ \begin{aligned} &P(b, b, \phi) - P(a, b, \phi) - P(b, a, \phi) + P(a, a, \phi) \\ &\cos \phi [Q(b, b, \phi) - Q(a, b, \phi) - Q(b, a, \phi) + Q(a, a, \phi)] \end{aligned} \right\} d\phi, \quad (35)$$

where $P(x, y, \phi)$ and $Q(x, y, \phi)$ are defined as

$$P(x, y, \phi) = \frac{1}{6} \left\{ \begin{aligned} &[(2 - 3\cos^2 \phi)y^2 - xy \cos \phi + 2x^2]v(x, y, \phi) \\ &+ 3y^3 \cos \phi \sin^2 \phi \ln[x - y \cos \phi + v(x, y, \phi)] \end{aligned} \right\}, \quad (36)$$

$$Q(x, y, \phi) = \frac{1}{18} \left\{ \begin{aligned} &3y(3y \cos \phi + x)v(x, y, \phi) + 3(3\cos^2 \phi - 1)y^3 \ln[x - y \cos \phi + v(x, y, \phi)] \\ &+ 6x^3 \ln[y - x \cos \phi + v(x, y, \phi)] \end{aligned} \right\}, \quad (37)$$

and $v(x, y, \phi) = \sqrt{x^2 + y^2 - 2xy \cos \phi}$. (35) only involves a single integral which needs to

be solved numerically. Singularity occurs when $\phi=0$, which can be solved using

appropriate an quadrature method when doing the numerical integral. The adaptive

Gauss-Kronrod quadrature function in MATLAB [19] is used in this work.

The detailed derivation is shown as

$$\begin{aligned} p^{S_{ij}} &= \frac{1}{2\pi^2 \varepsilon_0 (b^2 - a^2)^2} \int_a^b \int_a^b \int_0^{2\pi} \frac{\rho \rho' d\phi' d\rho' d\rho}{\sqrt{\rho^2 + \rho'^2 - 2\rho\rho' \cos \phi'}} \\ &= \frac{1}{2\pi^2 \varepsilon_0 (b^2 - a^2)^2} \int_0^{2\pi} \int_a^b \rho \left\{ \begin{aligned} &\sqrt{\rho^2 + b^2 - 2\rho b \cos \phi'} - \sqrt{\rho^2 + a^2 - 2\rho a \cos \phi'} \\ &+ \rho \cos \phi' \ln \left[\frac{\sqrt{\rho^2 + b^2 - 2\rho b \cos \phi'} + b - \rho \cos \phi'}{\sqrt{\rho^2 + a^2 - 2\rho a \cos \phi'} + a - \rho \cos \phi'} \right] \end{aligned} \right\} d\rho d\phi' \end{aligned}$$

There are two types of integrals need to be evaluated analytically for ρ as

$$\int_a^b \rho \sqrt{\rho^2 + \alpha^2 - 2\rho\alpha \cos \phi'} d\rho \text{ and } \int_a^b \rho^2 \ln \left[\sqrt{\rho^2 + \alpha^2 - 2\rho\alpha \cos \phi'} + \alpha - \rho \cos \phi' \right] d\rho,$$

where $\alpha = a, b$. Their analytical solutions are solved using Mathematica [20] and the results are just (36) and (37).

3) Mutual Term Between Vertical Cells

The final solution of (14) for the mutual term between vertical cells is shown as

$$pS_{ij} = \frac{1}{8\pi^2 \varepsilon_0 h(l_2 - l_1)} \int_0^{2\pi} \left[R(h-l_1, \phi) - R(h-l_2, \phi) - R(-l_1, \phi) + R(-l_2, \phi) \right] d\phi, \quad (38)$$

where $R(x, \phi)$ is defined as

$$R(x, \phi) = x \ln \left(x + \sqrt{w(\phi)^2 + x^2} \right) - \sqrt{x^2 + w(\phi)^2}, \quad (39)$$

$$\text{and } w(\phi) = \sqrt{\rho^2 + \rho'^2 - 2\rho\rho' \cos \phi}.$$

The detailed derivation is shown as

$$\begin{aligned} pS_{ij} &= \frac{1}{8\pi^2 \varepsilon_0 h(l_2 - l_1)} \int_{l_1}^{l_2} \int_0^h \int_0^{2\pi} \frac{d\phi' dz' dz}{\sqrt{\rho^2 + \rho'^2 - 2\rho\rho' \cos \phi' + (z - z')^2}} \\ &= \frac{1}{8\pi^2 \varepsilon_0 h(l_2 - l_1)} \int_0^{2\pi} \int_{l_1}^{l_2} \ln \left\{ \frac{h - z + \sqrt{\rho^2 + \rho'^2 - 2\rho\rho' \cos \phi' + (h - z)^2}}{-z + \sqrt{\rho^2 + \rho'^2 - 2\rho\rho' \cos \phi' + z^2}} \right\} dz d\phi' \\ &= A_{coef} \int_0^{2\pi} \int_{l_1}^{l_2} \left\{ \ln \left(h - z + \sqrt{w^2 + (h - z)^2} \right) - \ln \left(-z + \sqrt{w^2 + z^2} \right) \right\} dz d\phi' \\ &\quad (w^2 = \rho^2 + \rho'^2 - 2\rho\rho' \cos \phi') \\ &= A_{coef} \int_0^{2\pi} \left\{ \left[x \ln \left(x + \sqrt{w^2 + x^2} \right) - \sqrt{x^2 + w^2} \right] \Big|_{h-l_2}^{h-l_1} - \left[y \ln \left(y + \sqrt{w^2 + y^2} \right) - \sqrt{y^2 + w^2} \right] \Big|_{-l_2}^{-l_1} \right\} d\phi' \\ &\quad (x = h - z' \quad y = -z') \end{aligned}$$

4) Mutual Term Between Horizontal Cells

The final solution of (15) for the mutual term between horizontal cells depends on the elevation of the two cells. If the two cells have the same elevation, meaning their z-coordinates are the same, the expression is similar as the self term as

$$pS_{ij} = \frac{\int_0^{2\pi} \left\{ \begin{array}{l} P(d,b,\phi) - P(c,b,\phi) - P(d,a,\phi) + P(c,a,\phi) \\ \cos \phi [Q(d,b,\phi) - Q(c,b,\phi) - Q(d,a,\phi) + Q(c,a,\phi)] \end{array} \right\} d\phi}{2\pi^2 \varepsilon_0 (d^2 - c^2)(b^2 - a^2)}. \quad (40)$$

If the elevations of the two cells are different, the final expression is shown as

$$pS_{ij} = \frac{\int_0^{2\pi} \left\{ \begin{array}{l} S(d,b,\phi) - S(c,b,\phi) - S(d,a,\phi) + S(c,a,\phi) \\ \cos \phi [T(d,b,\phi) - T(c,b,\phi) - T(d,a,\phi) + T(c,a,\phi)] \end{array} \right\} d\phi}{2\pi^2 \varepsilon_0 (d^2 - c^2)(b^2 - a^2)}. \quad (41)$$

where $S(x,y,\phi)$ and $T(x,y,\phi)$ are defined as

$$S(x,y,\phi) = \frac{1}{6} \left\{ \begin{array}{l} [(2 - 3\cos^2 \phi)y^2 - xy \cos \phi + 2(x^2 + z_d^2)]u(x,y,\phi) \\ + 3y \cos \phi (y^2 \sin^2 \phi + z_d^2) \ln [x - y \cos \phi + u(x,y,\phi)] \end{array} \right\}, \quad (42)$$

$$T(x,y,\phi) = \frac{1}{18} \left\{ \begin{array}{l} 3 \left(3y^2 \cos \phi + xy + 2z_d^2 \frac{\cos \phi}{\sin^2 \phi} \right) u(x,y,\phi) + 6x^3 \ln [u(x,y,\phi) + y - x \cos \phi] \\ + 3y [(3\cos^2 \phi - 1)y^2 - 3z_d^2] \ln [x - y \cos \phi + u(x,y,\phi)] \\ - \frac{3z_d^3}{\sin^3 \phi} \text{angle} \left\{ \begin{array}{l} \left[\begin{array}{l} z_d (-x + y \cos \phi - \cos \phi u(x,y,\phi)) \\ + j \sin \phi (xy \cos \phi - y^2 - z_d^2 + yu(x,y,\phi)) \end{array} \right] \\ * \left[\begin{array}{l} z_d (-x + y \cos \phi + \cos \phi u(x,y,\phi)) \\ - j \sin \phi (xy \cos \phi - y^2 - z_d^2 - yu(x,y,\phi)) \end{array} \right] \end{array} \right\} \end{array} \right\} \quad (43)$$

and $u(x,y,\phi) = \sqrt{x^2 + y^2 - 2xy \cos \phi + z_d^2}$, and $z_d = z - z'$.

The detailed derivation is shown as

$$pS_{ij} = \frac{1}{2\pi^2 \varepsilon_0 (b^2 - a^2)(d^2 - c^2)} \int_a^b \int_c^d \int_0^{2\pi} \frac{\rho \rho' d\phi' d\rho' d\rho}{\sqrt{\rho^2 + \rho'^2 - 2\rho\rho' \cos \phi' + (z - z')^2}}$$

$$= \frac{\int_0^{2\pi} \int_c^d \rho \left\{ \begin{aligned} & \left[\sqrt{\rho^2 + b^2 - 2\rho b \cos \phi' + (z - z')^2} - \sqrt{\rho^2 + a^2 - 2\rho a \cos \phi' + (z - z')^2} \right] \\ & + \rho \cos \phi' \ln \left[\frac{\sqrt{\rho^2 + b^2 - 2\rho b \cos \phi' + (z - z')^2} + b - \rho \cos \phi'}{\sqrt{\rho^2 + a^2 - 2\rho a \cos \phi' + (z - z')^2} + a - \rho \cos \phi'} \right] \end{aligned} \right\} d\rho d\phi'}{2\pi^2 \varepsilon_0 (b^2 - a^2)(d^2 - c^2)}$$

and $S(x,y, \phi)$, $T(x,y, \phi)$ are the solution obtained from Mathematica for the following two integrals, which are the solutions of the ρ integral in the above equation.

$$\int x \sqrt{x^2 + y^2 - 2xy \cos \phi' + (z - z')^2} dx,$$

$$\int x^2 \ln \left[\sqrt{x^2 + y^2 - 2xy \cos \phi' + (z - z')^2} + y - x \cos \phi' \right] dx.$$

5) Mutual Term Between Horizontal and Vertical Cells

The solution of (16) for the mutual term between a horizontal and a vertical cell is shown as

$$pS_{ij} = \frac{\int_0^{2\pi} \left\{ \begin{aligned} & M(b', p_1, q_1, \phi) - M(a', p_1, q_1, \phi) - M(b', p_2, q_2, \phi) + M(a', p_2, q_2, \phi) \\ & + \cos \phi \left[N(b', p_1, q_1, \phi) - N(a', p_1, q_1, \phi) - N(b', p_2, q_2, \phi) + N(a', p_2, q_2, \phi) \right] \end{aligned} \right\} d\phi}{4\pi^2 \varepsilon_0 h (b^2 - a^2)}, \quad (44)$$

where,

$$b' = b - \rho' \cos \phi, \quad a' = a - \rho' \cos \phi;$$

$$p_1 = h - z, \quad p_2 = -z;$$

$$q_1 = \sqrt{p_1^2 + \rho'^2 \sin^2 \phi}, \quad q_2 = \sqrt{p_2^2 + \rho'^2 \sin^2 \phi},$$

and $M(x,p,q, \phi)$ and $N(x,p,q, \phi)$ are defined as

$$M(x, p, q, \phi) = \frac{1}{4} \left\{ 2(q^2 - p^2 + x^2) \ln \left[p + \sqrt{x^2 + q^2} \right] + 2p\sqrt{x^2 + q^2} \right\}, \quad (45)$$

$$N(x, p, q, \phi) = \left\{ \begin{array}{l} x \ln \left[p + \sqrt{x^2 + q^2} \right] + p \ln \left[x + \sqrt{x^2 + q^2} \right] \\ -\sqrt{q^2 - p^2} \tan^{-1} \left(\frac{xp}{\sqrt{q^2 - p^2} \sqrt{x^2 + q^2}} \right) \end{array} \right\}. \quad (46)$$

The detailed derivation is shown as

$$\begin{aligned} p_{ij}^s &= \frac{1}{4\pi^2 \varepsilon_0 h(b^2 - a^2)} \int_a^b \int_0^h \int_0^{2\pi} \frac{\rho d\phi' dz' d\rho}{\sqrt{\rho^2 + \rho'^2 - 2\rho\rho' \cos \phi' + (z - z')^2}} \\ &= \frac{1}{4\pi^2 \varepsilon_0 h(b^2 - a^2)} \int_a^b \int_{-z}^{h-z} \int_0^{2\pi} \frac{\rho d\phi' dz' d\rho}{\sqrt{\rho^2 + \rho'^2 - 2\rho\rho' \cos \phi' + z'^2}} \\ &= \frac{1}{4\pi^2 \varepsilon_0 h(b^2 - a^2)} \int_0^{2\pi} \int_a^b \rho \ln \left(\frac{h - z + \sqrt{\rho^2 + \rho'^2 - 2\rho\rho' \cos \phi' + (h - z)^2}}{-z + \sqrt{\rho^2 + \rho'^2 - 2\rho\rho' \cos \phi' + z^2}} \right) d\rho d\phi' \\ &= A_{coef} \int_0^{2\pi} \int_a^b \rho \ln \left(\frac{h - z + \sqrt{(\rho - \rho' \cos \phi')^2 + \rho'^2 \sin^2 \phi' + (h - z)^2}}{-z + \sqrt{(\rho - \rho' \cos \phi')^2 + \rho'^2 \sin^2 \phi' + z^2}} \right) d\rho d\phi' \\ &= A_{coef} \int_0^{2\pi} \int_{a-\rho' \cos \phi'}^{b-\rho' \cos \phi'} (x + \rho' \cos \phi') \left[\ln \left(a + \sqrt{x^2 + b^2} \right) - \ln \left(c + \sqrt{x^2 + d^2} \right) \right] dx d\phi' \\ &\quad \left\{ \begin{array}{l} a = h - z; b^2 = \rho'^2 \sin^2 \phi' + (h - z)^2 \\ c = -z; d^2 = \rho'^2 \sin^2 \phi' + z^2 \end{array} \right\} \\ &= A_{coef} \int_0^{2\pi} d\phi' \left\{ \begin{array}{l} \int_{a-\rho' \cos \phi'}^{b-\rho' \cos \phi'} x \ln \left(a + \sqrt{x^2 + b^2} \right) dx - \int_{a-\rho' \cos \phi'}^{b-\rho' \cos \phi'} x \ln \left(c + \sqrt{x^2 + d^2} \right) dx \\ + \rho' \cos \phi' \int_{a-\rho' \cos \phi'}^{b-\rho' \cos \phi'} \ln \left(a + \sqrt{x^2 + b^2} \right) dx - \rho' \cos \phi' \int_{a-\rho' \cos \phi'}^{b-\rho' \cos \phi'} \ln \left(c + \sqrt{x^2 + d^2} \right) dx \end{array} \right\}. \end{aligned}$$

There are two types of integrals and they can be solved analytically through Mathematica

as

$$\begin{aligned} &\int_{a-\rho' \cos \phi'}^{b-\rho' \cos \phi'} x \ln \left(c + \sqrt{x^2 + d^2} \right) dx \\ &= \frac{1}{4} \left\{ 2(\rho'^2 \sin^2 \phi' + x^2) \ln \left[c + \sqrt{d^2 + x^2} \right] + 2c\sqrt{d^2 + x^2} - x^2 \right\} \Big|_{a-\rho' \cos \phi'}^{b-\rho' \cos \phi'}, \end{aligned}$$

$$\int_{a-\rho'\cos\phi'}^{b-\rho'\cos\phi'} \ln\left(c + \sqrt{x^2 + d^2}\right) dx$$

$$= \left\{ \begin{array}{l} -x + \rho' \sin \phi' \arctan\left(\frac{x}{\rho' \sin \phi'}\right) - \rho' \sin \phi' \arctan\left(\frac{cx}{\rho' \sin \phi' \sqrt{d^2 + x^2}}\right) \\ + x \ln\left(c + \sqrt{x^2 + d^2}\right) + c \ln\left(\sqrt{d^2 + x^2} + x\right) \end{array} \right\} \Big|_{a-\rho'\cos\phi'}^{b-\rho'\cos\phi'}$$

6) Integral for Line Approximation

The approximation integral (17) can also be evaluated analytically as

$$ps_{ij} = \frac{1}{4\pi^2 \varepsilon_0} \frac{\alpha}{\sqrt{\rho\rho'}} K(\alpha), \quad (47)$$

where $\alpha^2 = \frac{4\rho\rho'}{(\rho + \rho')^2 + (z - z')^2}$ and $K(\alpha)$ is the first kind complete elliptical integral.

The detailed derivation is shown as

$$ps_{ij} = \frac{1}{8\pi^2 \varepsilon_0} \int_0^{2\pi} \frac{d\phi'}{\sqrt{\rho^2 + \rho'^2 - 2\rho\rho' \cos \phi' + (z - z')^2}} \quad \phi' = 2\theta$$

$$= \frac{1}{4\pi^2 \varepsilon_0} \int_0^{\pi/2} \frac{2d\theta}{\sqrt{(\rho + \rho')^2 + (z - z')^2 - 4\rho\rho' \cos^2 \theta}}$$

$$= \frac{1}{4\pi^2 \varepsilon_0} \frac{\alpha}{\sqrt{\rho\rho'}} \int_0^{\pi/2} \frac{d\theta}{\sqrt{1 - \alpha^2 \cos^2 \theta}}$$

The solution of the integral in the last line is just the complete elliptical integral, which can be evaluated from Mathematica.

B. Integrals for Axially Asymmetric Case

1) Self Term for Horizontal Cells

The integral (19) of the self term for a horizontal cell can be analytically evaluated to a double integral as

$$pS_{ii} = \frac{1}{\pi\epsilon_0\theta^2(b^2 - a^2)^2} \int_0^\theta \int_0^\theta \left\{ P(b,b,\tau) - P(a,b,\tau) - P(b,a,\tau) + P(a,a,\tau) \right. \\ \left. \cos \tau [Q(b,b,\tau) - Q(a,b,\tau) - Q(b,a,\tau) + Q(a,a,\tau)] \right\} d\phi d\phi', \quad (48)$$

where $\tau = \phi - \phi'$ and $P(x,y,\tau)$, $Q(x,y,\tau)$ have the same definitions as in (36) and (37). The detailed derivation is similar as the axially symmetric case. The singularity is removed using the method in [18] as

$$\int_0^\theta \int_0^\theta F(\phi - \phi') d\phi d\phi' = 2 \left[\int_0^\theta \int_0^{\sqrt{\phi'}} t F(\phi' - t^2) dt d\phi' + \int_0^\theta \int_0^{\sqrt{\theta - \phi'}} t F(\phi' + t^2) dt d\phi' \right], \quad (49)$$

where $F(\phi - \phi')$ represents the integrand in (48). The numerical integral function over a planar region in MATLAB [19] is used to evaluate (49).

2) Self Term for Vertical Cells

The integral (20) of the self term for a vertical cell can be evaluated as

$$pS_{ii} = \frac{1}{4\pi\epsilon_0\phi^2 h^2} \int_0^\theta \int_0^\theta \left[2h \ln \left(h + \sqrt{h^2 + w^2} \right) - 2\sqrt{h^2 + w^2} + 2w - h \ln w^2 \right] d\phi d\phi', \quad (50)$$

where $w^2 = 2\rho^2 [1 - \cos(\phi - \phi')]$. The detailed derivation is similar as the axially symmetric case. The singularity can be easily removed by adding a very small number (e.g. 1e-37) in the natural logarithm.

3) Mutual Term Between Vertical Cells

The integral (22) of the mutual term between vertical cells can be evaluated as

$$pS_{ij} = \frac{1}{4\pi\epsilon_0 h(l_2 - l_1)(\theta_2 - \theta_1)(\theta_4 - \theta_3)} \int_{\theta_1}^{\theta_2} \int_{\theta_3}^{\theta_4} \left[\begin{array}{l} R(h - l_1, \phi, \phi') - R(h - l_2, \phi, \phi') \\ -R(-l_1, \phi, \phi') + R(-l_2, \phi, \phi') \end{array} \right] d\phi d\phi', \quad (51)$$

where $R(x, \phi, \phi')$ has the similar definition as in (39) except $w(\phi)$ is replaced by $L(\rho, \rho', \phi, \phi', d)$ defined in (21). The detailed derivation is similar as the axially symmetric case.

4) Mutual Term Between Horizontal Cells

The integral (23) of the mutual term between horizontal cells can be evaluated to a triple integral as

$$pS_{ij} = \frac{1}{\pi\epsilon_0 (\theta_2 - \theta_1)(\theta_4 - \theta_3)(b^2 - a^2)(f^2 - c^2)} \int_{\theta_1}^{\theta_2} \int_{\theta_3}^{\theta_4} \int_a^b \rho \left\{ \sqrt{Z(f)} - \sqrt{Z(c)} + A \ln \left(\frac{\sqrt{Z(f)} - A + f}{\sqrt{Z(c)} - A + c} \right) \right\} d\rho, \quad (52)$$

where $Z(x)$ and A are defined as

$$Z(x) = L(\rho, x, \phi, \phi', d)^2 + (z - z')^2 = (x - A)^2 + B^2, \quad (53)$$

$$A = \rho \cos(\phi - \phi') - d \cos \phi', \quad (54)$$

and B is defined as

$$B = \sqrt{(\rho \sin(\phi - \phi') + d \sin \phi')^2 + (z - z')^2}, \quad (55)$$

5) Mutual Term Between Vertical and Horizontal Cells

The integral (24) of the mutual term between a vertical and a horizontal cell can be evaluated as

$$pS_{ij} = \frac{\int_{\theta_1}^{\theta_2} \int_{\theta_3}^{\theta_4} \left\{ \begin{array}{l} M(b', p_1, q_1, \phi, \phi') - M(a', p_1, q_1, \phi, \phi') \\ -M(b', p_2, q_2, \phi, \phi') + M(a', p_2, q_2, \phi, \phi') \\ + \cos \phi \left[\begin{array}{l} N(b', p_1, q_1, \phi, \phi') - N(a', p_1, q_1, \phi, \phi') \\ -N(b', p_2, q_2, \phi, \phi') + N(a', p_2, q_2, \phi, \phi') \end{array} \right] \end{array} \right\} d\phi d\phi'}{2\pi\epsilon_0 h(b^2 - a^2)(\theta_2 - \theta_1)(\theta_4 - \theta_3)}, \quad (56)$$

where,

$$b' = b - \rho' \cos(\phi - \phi') - d \cos \phi;$$

$$a' = a - \rho' \cos(\phi - \phi') - d \cos \phi;$$

$$p_1 = h - z, \quad p_2 = -z;$$

$$q_1 = \sqrt{p_1^2 + (\rho' \sin(\phi - \phi') + d \sin \phi)^2};$$

$$q_2 = \sqrt{p_2^2 + (\rho' \sin(\phi - \phi') + d \sin \phi)^2};$$

and $M(x, p, q, \phi)$ and $N(x, p, q, \phi)$ are defined as in (45) and (46).

The detailed derivation is shown as

$$\begin{aligned} pS_{ij} &= \frac{\int_a^b \int_0^h \int_{\phi_1}^{\phi_2} \int_{\phi_3}^{\phi_4} \frac{\rho d\phi d\phi' dz' d\rho}{\sqrt{\rho^2 + \rho'^2 - 2\rho\rho' \cos(\phi' - \phi) - 2d(\rho \cos \phi - \rho' \cos \phi') + d^2 + (z - z')^2}}}{2\pi\epsilon_0 h(b^2 - a^2)(\phi_2 - \phi_1)(\phi_4 - \phi_3)} \\ &= B_{coef} \int_{\phi_1}^{\phi_2} \int_{\phi_3}^{\phi_4} \int_a^b \rho \ln \left(\frac{h - z + \sqrt{(\rho - \rho' \cos(\phi - \phi') - d \cos \phi)^2 + (\rho' \sin(\phi - \phi') + d \sin \phi)^2 + (h - z)^2}}{-z + \sqrt{(\rho - \rho' \cos(\phi - \phi') - d \cos \phi)^2 + (\rho' \sin(\phi - \phi') + d \sin \phi)^2 + z^2}} \right) d\rho d\phi d\phi' \\ &= B_{coef} \int_{\phi_1}^{\phi_2} \int_{\phi_3}^{\phi_4} \int_{a - \rho' \cos(\phi - \phi') - d \cos \phi}^{b - \rho' \cos(\phi - \phi') - d \cos \phi} \left[\ln \left(a + \sqrt{x^2 + b^2} \right) - \ln \left(c + \sqrt{x^2 + d^2} \right) \right] dx d\phi d\phi' \end{aligned}$$

$$\text{where } \left\{ \begin{array}{l} a = h - z; b^2 = (\rho' \sin(\phi - \phi') + d \sin \phi)^2 + (h - z)^2 \\ c = -z; d^2 = (\rho' \sin(\phi - \phi') + d \sin \phi)^2 + z^2 \end{array} \right\} \text{ and the final results can be}$$

derived similarly as the axially symmetric case.

REFERENCES

- [1] Rimolo-Donadio, R.; Xiaoxiong Gu; Kwarq, Y.H.; Ritter, M.B.; Archambeault, B.; de Paulis, F.; Yaojiang Zhang; Jun Fan; Bruns, H.-D.; Schuster, C.; , "Physics-Based Via and Trace Models for Efficient Link Simulation on Multilayer Structures Up to 40 GHz," *Microwave Theory and Techniques, IEEE Transactions on* , vol.57, no.8, pp.2072-2083, Aug. 2009.
- [2] C. Schuster, Y. H. Kwarq, G. Selli, and P. Muthana, "Developing a physical model for vias," in *Proc. IEC Designcon Conf.*, Santa Clara, CA, Feb. 2006, pp. 1–24.
- [3] G. Selli, C. Schuster, Y. Kwarq, M. Ritter, and J. L. Drewniak, "Model-to-hardware correlation of physics based via models with the parallel plate impedance included," in *Proc. IEEE Electromagn. Compat. Symp.*, Portland, OR, Aug. 2006, pp. 781–785.

- [4] S. Pan, J. Fan, and J. L. Drewniak, "Equivalent characteristic impedance and propagation constant for multi-layer via structures," *2009 International Symposium on Electromagnetic Compatibility*, Kyoto, Japan, July 20-24, 2009.
- [5] Siming Pan; Jun Fan; , "Equivalent mixed-mode characteristic impedances for differential signal vias," *Electromagnetic Compatibility, 2009. EMC 2009. IEEE International Symposium on* , vol., no., pp.74-79, 17-21 Aug. 2009.
- [6] Y. Zhang, J. Fan, G. Selli, M. Cocchini, F. De Paulis, "Analytical Evaluation of Via-to-plane Capacitance for Multilayer Printed Circuit Boards and Packages," *IEEE Trans. Microwave Theory Tech.*, vol. 56, no. 9, pp. 2118-2128, Sep. 2008.
- [7] Pajovic, M.M.; , "A Closed-Form Equation for Estimating Capacitance of Signal Vias in Arbitrarily Multilayered PCBs," *Electromagnetic Compatibility, IEEE Transactions on* , vol.50, no.4, pp.966-973, Nov. 2008.
- [8] K. Nabors and J. White, "FastCap: A multipole accelerated 3-D capacitance extraction program," *IEEE Trans. Computer-Aided Design*, vol. 10, pp. 1447-1459, Nov. 1991.
- [9] Y. L. Le Coz and R. B. Iverson, "A stochastic algorithm for high-speed capacitance extraction in integrated circuits," *IEEE Trans. Microwave Theory Tech.*, vol. 40, pp. 1507-1516, July 1992.
- [10] Hanfeng Wang; Albert E. Ruehli; Jun Fan; , "Hybrid method used to model via transitions," *Electromagnetic Compatibility (EMC), 2010 IEEE International Symposium on* , vol., no., pp.401-406, 25-30 July 2010.
- [11] Wang, Hanfeng; Ruehli, Albert E.; Fan, Jun; , "Capacitance calculation for a shared-antipad via structure using an integral equation method based on partial capacitance," *Electrical Performance of Electronic Packaging and Systems (EPEPS), 2011 IEEE 20th Conference on* , vol., no., pp.271-274, 23-26 Oct. 2011.
- [12] B. Wu and L. Tsang, "Full-wave modeling of multiple vias using differential signaling and shared antipad in multilayered high speed vertical interconnects," *Progress In Electromagnetics Research*, Vol. 97, 129-139, 2009.
- [13] Clayton R. Paul, "Analysis of Multiconductor Transmission Lines," John Wiley & Sons, Inc. New York, 1994, pp. 69-72.
- [14] A. E. Ruehli, P. A. Brennan. "Efficient capacitance calculations for three dimensional multiconductor systems," *IEEE Transactions on Microwave Theory and Techniques*, MTT-21(2):76-82, February 1973.
- [15] Haus, Hermann A., and James R. Melcher, *Electromagnetic Fields and Energy*. (Massachusetts Institute of Technology: MIT OpenCourseWare). <http://ocw.mit.edu> (accessed 01/26/2012). License: Creative Commons Attribution-NonCommercial-Share Alike.
- [16] Silvester, P.; , "TEM wave properties of microstrip transmission lines," *Electrical Engineers, Proceedings of the Institution of* , vol.115, no.1, pp.43-48, January 1968.
- [17] Q3D Extractor 9. [Online].
Available: http://www.ansoft.com/products/si/q3d_extractor/
- [18] Ermanno Cardelli, Loris Faina, "Numerical Evaluation Of Singular Integrands In The Application Of The Charge Simulation Method With Distributed Charge Density," *Applied Computational Electromagnetics Society journal*, vol. 11, no. 3, pp. 16-24, Nov. 1996.

- [19] L.F. Shampine "Vectorized Adaptive Quadrature in MATLAB," *Journal of Computational and Applied Mathematics*, 211, 2008, pp.131–140.
- [20] Mathematica 7. [Online]. Available: <http://www.wolfram.com/mathematica/>

II. Surface PEEC Modeling for Shared-Antipad Via Structure Using Cavity Green's Function and Wave Port Excitation

Hanfeng Wang, Siming Pan, Albert Ruehli, and Jun Fan

Abstract—A rigorous modeling of the shared-antipad via structure is developed using surface partial element equivalent circuit (PEEC). The cavity Green's function is used to evaluate the equivalent circuit elements, thereby requiring fewer cells for numerical computation. The non-orthogonal, quadrilateral cell is used in the mesh to better accommodate the non-rectangular shape of the via and the antipad. A novel wave port excitation method is applied to the equivalent circuit to obtain the network parameters of the via transition. The Z-parameters of the via structure are calculated using the proposed method, and the results are validated with the finite element solution obtained from commercial software.

Index Terms—surface PEEC, cavity Green's function, wave port excitation, shared-antipad via structure.

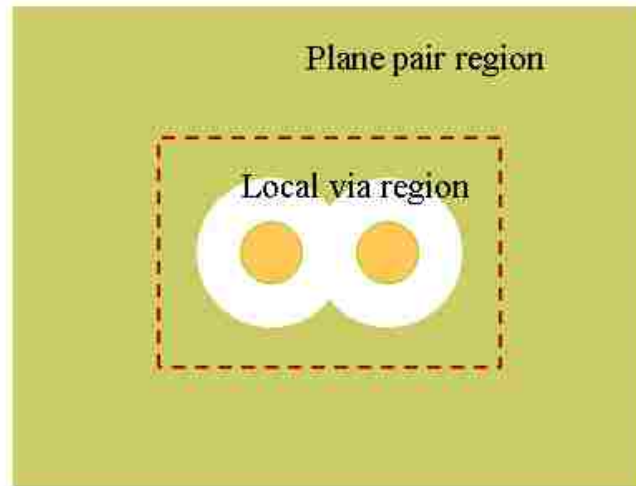
I. INTRODUCTION

Vias are an important part of modern printed circuit boards (PCBs) since they are used to connect traces on different layers of the board. The vias represent discontinuities for the transmission line models of traces along signal paths. These discontinuities, in turn, cause frequency-dependent degradation and distortion of high-speed signals. The modeling and simulation of vias is therefore essential to correctly design today's high-speed circuit boards beyond 10Gbits/s [1], [2].

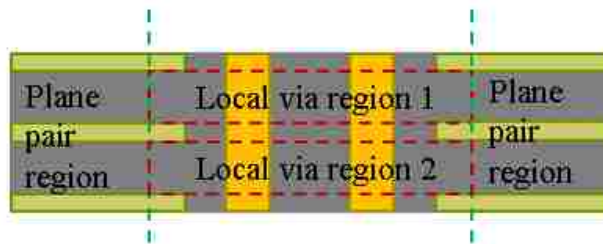
Full wave method [25] can be used for via modeling, but the disadvantage is that it's time and memory consuming. A physics-based circuit model has been developed in [3], [4] to analyze the via structure using an equivalent circuit model. Using the physics-

based circuit model, an equivalent transmission line model is further developed for the via structure [5], [6]. However, both the physics-based model and equivalent transmission line model are based on physical intuition. The boundary conditions at the vias are not satisfied by the circuit model. In addition, the coupling between vias is described by the parallel-plane impedance matrix (the TM_{z0} modes) only. Therefore, when vias are closely spaced and the coupling due to the higher order modes become non-negligible, the accuracy of the physics-based model will start to deteriorate. The multiple-scattering method [7] takes the coupling due to the higher order modes into consideration. However, both the multiple-scattering and the physics-based circuit model are also limited to the regular circular via antipad shape and cannot deal with the shared-antipad shape, which is widely used in differential via design [8]. The two methods are also layer based, thus, the coupling between layers through antipad is also ignored.

To overcome the limitations of the physics-based model and the multiple-scattering method, rigorous electromagnetic analysis needs to be derived for the local via region. Specifically, boundary conditions for the local via domains need to be explicitly enforced, as shown in [9]. The local via domain will be modeled using full-wave method and the rest of the plane region will be modeled using cavity method [11]. The separation of the local via region and the plane pair region can be illustrated in Fig. 1 for a typical structure of a differential via pair with a shared antipad inside a parallel plane cavity.



(a) Top View



(b) Side View

Fig. 1 Differential Via with shared-antipad inside plane pair cavities

The local via region in the multi-layer PCB structure in Fig. 1 can be further divided layer by layer. In this paper, we focus on the modeling of local via region for one layer as shown in Fig. 1(b). The local via region will be modeled rigorously using the PEEC method [10]. The PEEC approach has evolved over the years and has been widely used for electromagnetic modeling of various problems including electromagnetic compatibility (EMC), electromagnetic interference (EMI), signal integrity (SI) and power integrity (PI) problems associated with high speed circuits [12]-[15]. The advantage of the PEEC method, as compared to other integral-equation-based electromagnetic (EM)

methods (such as the method of moments (MoM)), is that it can convert physical geometries into SPICE-compatible, equivalent lumped circuits. Thus, this makes the PEEC approach very suitable for complex problems having large scale variations inside the system.

Surface PEEC using equivalence principle is introduced in [17], [19] to handle inhomogeneous problems such as multilayered PCB. In order to model arbitrary geometries, non-orthogonal PEEC cells are introduced in [18], which extends the traditional rectangular PEEC method to problems requiring non-rectangular geometry, such as the shared-antipad structure in our study.

The main contributions of this paper are as follows.

- 1) Instead of using the traditional free-space Green's function, the cavity Green's function is used to reduce the number of unknowns. By using the cavity Green's function, only the via surface and the antipad region need to be meshed, with no meshing needed on the plane surface.
- 2) A novel wave port excitation method is also applied to the antipad region to stimulate the equivalent circuit so that the network parameters can be obtained for the via structure.
- 3) Both surface PEEC and non-orthogonal cells are used to model the shared-antipad via structure together with the cavity Green's function. Singularity handling of the cavity Green's function for non-orthogonal cells is introduced.
- 4) The model has been validated using commercial full wave simulation tool up to 20 GHz.

II. FORMULATIONS

A. Equivalent Problem

The method used to solve the local via region in one cavity is illustrated in Fig. 2.

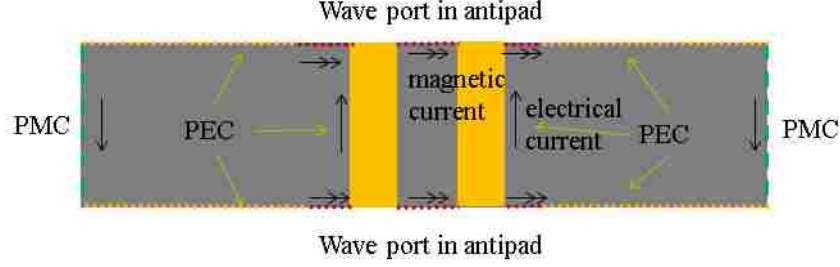


Fig. 2 Illustration of solving the local via region problem

The interface between the antipad region and the cavity is replaced with a perfect electric conductor (PEC) and a magnetic current is applied on this interface. The boundary of the local via domain and the outermost lateral boundary of the power plane pair are both treated as a perfect magnetic conductor (PMC). In addition, electrical current needs to be impressed on the side boundary. Further, if we replace the via conductor surface with an impressed electrical current, the whole cavity can be enclosed with a combination of PECs and PMCs. The Green's function for this kind of cavity is known [16], and can be used in our PEEC formulation. To validate the proposed method for this specific region with HFSS [25], wave port is defined at the top and bottom antipad region and the PMC boundary condition is assigned at the side walls. Under such condition, the equivalent electric current on the side walls can be removed.

At the via surface, since the tangential E-field is zero, we should have the following equation [26]

$$0 = \hat{n} \times \mathbf{E} = \hat{n} \times \left(-j\omega \mathbf{A} - \nabla \Phi^e - \frac{1}{\varepsilon} \nabla \times \mathbf{F} \right), \quad (1)$$

where \mathbf{A} is the vector magnetic potential; Φ is the electric scalar potential; and \mathbf{F} is the vector electric potential.

At the antipad region, similar as in (1), the magnetic field should have the following representation of auxiliary potentials [26]

$$\hat{n} \times \mathbf{H} = \hat{n} \times \left(-j\omega \mathbf{F} - \nabla \Phi^m + \frac{1}{\mu} \nabla \times \mathbf{A} \right), \quad (2)$$

where Φ^m is the scalar magnetic potential.

B. Handling of Excitations

At the wave port defined at the antipad region in Fig. 2, if 1 A current is injected into the left via and -1 A of current is injected into the right via, the H-field distribution can be calculated in the antipad region using a two-dimensional finite element analysis. Then the calculated H-field can be used in the left side of (2) as the excitation at the port. After the numerical PEEC calculation in the computation domain in Fig. 2, the magnetic current distribution can be obtained at the port region. From the magnetic current, the E-field distribution and thus the port voltage can be obtained. The port voltage, together with the excitation current injected into the via, can give the impedance matrix of the whole structure. The impedance matrix can then be compared with the commercial tool to validate the proposed method. The detailed derivation of the wave port excitation will be described in Section D.

C. PEEC Formulations

The scalar and vector potential functions in (1) and (2) are related to current and charge sources using the Green's function as

$$\mathbf{A}(\mathbf{r}) = \mu \int_S \bar{\bar{G}}^A(\mathbf{r}, \mathbf{r}') \mathbf{J}(\mathbf{r}') ds', \quad (3)$$

$$\mathbf{F}(\mathbf{r}) = \varepsilon \int_S \bar{\bar{G}}^F(\mathbf{r}, \mathbf{r}') \mathbf{M}(\mathbf{r}') ds', \quad (4)$$

$$\Phi^e(\mathbf{r}) = \frac{1}{\varepsilon} \int_S G^q(\mathbf{r}, \mathbf{r}') q(\mathbf{r}') ds', \quad (5)$$

$$\Phi^m(\mathbf{r}) = \frac{1}{\mu} \int_S G^{q^m}(\mathbf{r}, \mathbf{r}') q^m(\mathbf{r}') ds', \quad (6)$$

where surface integrals are evaluated over the surface of the source cell. The calculation of the Green's function will be discussed in detail in Section III. In order to solve the local via region using PEEC, the geometry needs to be discretized and the equivalent circuit elements, including partial inductance, partial capacitance and EM-coupling terms, are evaluated based on equations (3) through (6). Finally, all the equivalent element is composed into a full equivalent circuits according to the equations (1) and (2).

1) Mesh

The non-orthogonal mesh needs to be used for the via structure since the traditional rectangular mesh is not strictly suitable for the circular shaped via. The non-orthogonal mesh for the via structure is illustrated in Fig. 3.

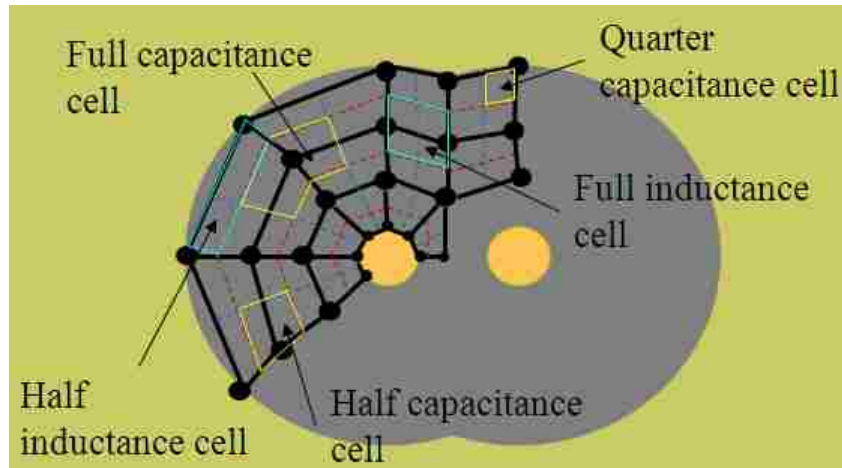


Fig. 3 Illustration of the non-orthogonal mesh on the via structure

The black dots indicate the nodes for the PEEC model and the black solid lines illustrate the basic quadrilateral cells for 2D surface cells. The red dashed lines are the boundary for inductance cells in one direction and the blue dashed lines are the boundary for inductance cells in another direction. Inductance cells are based on the connecting black line between the nodes. In the middle of the geometry, full inductance cells (two quadrilaterals stitching at the connection) have the connecting black line in the center of the cell. At the edge of the geometry, half inductance cells have the connecting black line at the edge of the cell. Capacitance cells are based on the nodes. In the middle of the geometry, full capacitance cells (four quadrilaterals stitching at the node) have nodes in the center. There are half capacitance cells (two quadrilaterals stitching) at the edge, and there are quarter capacitance cells at the corner of the geometry.

A full mesh for the antipad region is generated using the MATLAB code shown in Fig. 4. The mesh on the cylindrical via surface can be approximated with rectangles. The mesh on the outer PMC boundary surface is naturally the traditional rectangular shape.

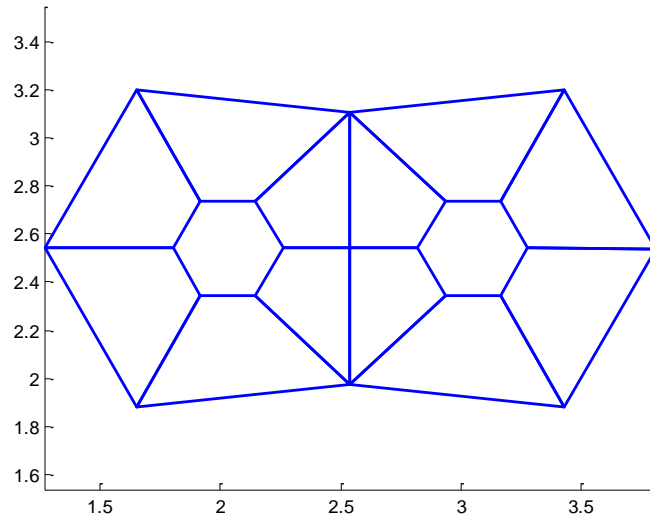


Fig. 4 Mesh for antipad generated using MATLAB

2) Formula to Calculate Equivalent Circuit Elements

By substituting equation (3) through (6) into equation (1) and (2), and applying another integral over the observation cell, the equivalent inductance, equivalent capacitance, and EM coupling term can be extracted. The first term of equation (1) corresponds to the equivalent electric inductance term. The second term of equation (1) corresponds to the equivalent electric capacitance term. The third term corresponds to the EM coupling term, which can be expressed by a current controlled voltage source (CCVS) in the equivalent SPICE circuit. The first and the second terms of (2) correspond to the magnetic equivalent inductance and capacitance, while the third term of (2) corresponds to the EM coupling term.

The extracted equivalent electric inductance, capacitance and EM coupling terms in non-orthogonal coordinates for surface cells can be expressed as

$$Lp_{aa'}^e = \mu \int_a \int_b \int_{a'} \int_{b'} \frac{1}{4} h_a \hat{a} \cdot h_{a'} \hat{a}' \bar{\bar{G}}^A(\mathbf{r}, \mathbf{r}') \hat{a}' da' db' dadb, \quad (7)$$

$$Pp^e = \frac{1}{\varepsilon} \int_a \int_b \int_{a'} \int_{b'} \frac{1}{16} G^q(\mathbf{r}, \mathbf{r}') da' db' dadb, \quad (8)$$

$$V_a^{E-M} = K_{a'} \int_a \int_b \int_{a'} \int_{b'} \frac{1}{4} h_a \hat{a} \cdot \nabla \times \bar{\bar{G}}^F(\mathbf{r}, \mathbf{r}') h_{a'} \hat{a}' da' db' dadb, \quad (9)$$

where a, b are the local coordinates of the quadrature; \mathbf{r} is the observation point vector in global Cartesian coordinates; $h_a = |\partial \mathbf{r} / \partial a|$ is the magnitude of the tangential vector along a direction; and $\hat{a} = (\partial \mathbf{r} / \partial a) / h_a$ is the position dependent unit vector along a direction [17].

The partial inductance and EM coupling terms listed above only show the coupling between a direction currents in both observation and source cells. The other terms have expressions in a similar form.

The magnetic circuit is similar to its electric counterpart by replacing the Green's function and interchanging μ and ε

$$Lp_{aa'}^m = \varepsilon \int_a \int_b \int_{a'} \int_{b'} \frac{1}{4} h_a \hat{a} \cdot h_{a'} \bar{\bar{G}}^F(\mathbf{r}, \mathbf{r}') \hat{a}' da' db' dadb, \quad (10)$$

$$Pp^m = \frac{1}{\varepsilon} \int_a \int_b \int_{a'} \int_{b'} \frac{1}{16} G^{qm}(\mathbf{r}, \mathbf{r}') da' db' dadb, \quad (11)$$

$$V_a^{M-E} = I_{a'} \int_a \int_b \int_{a'} \int_{b'} -\frac{1}{4} h_a \hat{a} \cdot \nabla \times \bar{\bar{G}}^A(\mathbf{r}, \mathbf{r}') h_{a'} \hat{a}' da' db' dadb. \quad (12)$$

3) Compose PEEC

The equivalent circuit elements derived in the previous subsections can be put together to form the equivalent circuits similar to [17]. The electric and magnetic equivalent circuits are shown in Fig. 5 and Fig. 6.

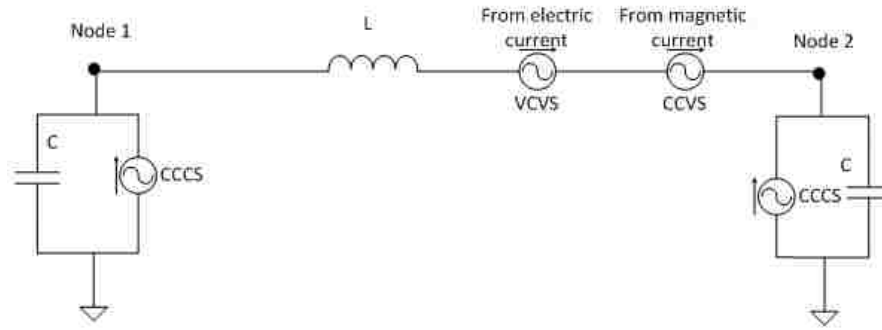


Fig. 5 Electric equivalent circuit

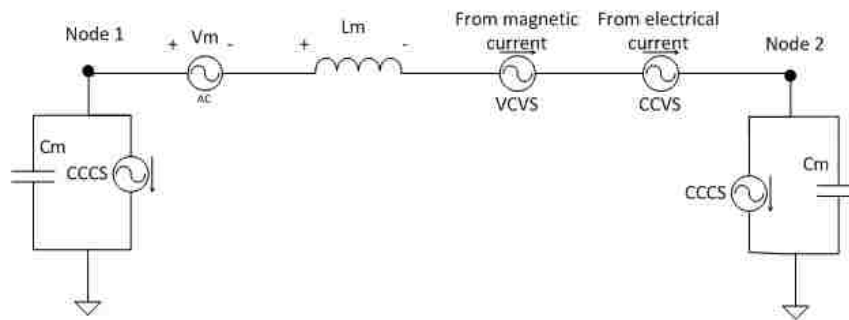


Fig. 6 Magnetic equivalent circuit

L and VCVS represent the inductive voltage drop, which can be evaluated using (7). CCVS represents the EM-coupling voltage drop, which can be evaluated using (9). L represents the self-inductor and VCVS represents the mutual inductor between two cells. The capacitor and CCCS term correspond to capacitive voltage drop which are similarly defined in [17] and the Pp terms can be evaluated using (8). The magnetic circuit elements are similarly defined as the electric ones. They can be evaluated by using (10)~(12) with an additional independent voltage source, which is related to the H-field distribution at the antipad region. The detailed information of this independent voltage source will be described in Section D.

D. Wave Port Excitation

The H-field at the left side of (2) can be similarly converted to a voltage drop in the equivalent circuit and integrated into the updated equivalent circuit as shown in Fig. 6.

The magnetic voltage source in Fig. 6 can be evaluated similarly as the electric voltage drop definition in [17] for non-orthogonal coordinates as

$$V_m = \int_a^b \int_b^a w_b \hat{b} \cdot \mathbf{H} \left| \frac{\partial \mathbf{r}}{\partial a} \times \frac{\partial \mathbf{r}}{\partial b} \right| da db = \frac{1}{2} \int_a^b \int_b^a h_b \hat{b} \cdot \mathbf{H} da db, \quad (13)$$

where $w_b = \frac{h_b}{2 \left| \frac{\partial \mathbf{r}}{\partial a} \times \frac{\partial \mathbf{r}}{\partial b} \right|}$ and assuming the voltage drop is along the b direction in the local

coordinate of the non-orthogonal cell. The integral can also be evaluated numerically using the Gaussian quadrature method.

After adding the independent magnetic voltage source to the equivalent circuit, the magnetic current along each inductance branch can be solved using a circuit solver. The magnetic current can then be converted into the electric voltage drop from via to plane as illustrated in Fig. 7.

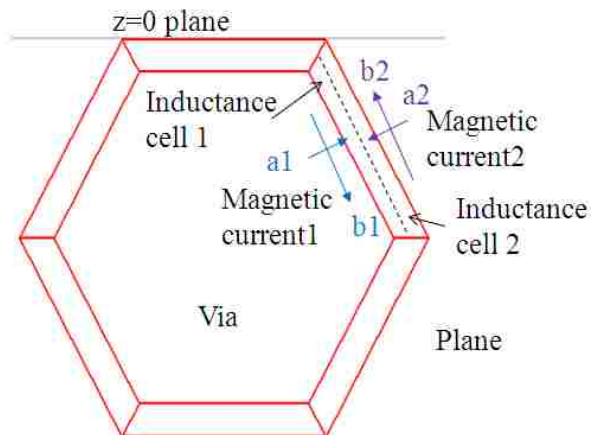


Fig. 7 illustration of magnetic current to electric voltage drop conversion

The traditional coaxial antipad structure is used as an example for the derivation of the magnetic current to electric voltage drop conversion. Both the outline of the via and the outer boundary of the antipad are approximated using hexagons and the antipad is located at the $z=0$ plane of the cavity. Two inductance cells at the top right in Fig. 7 are used as the example to calculate the electric voltage drop from the magnetic current flowing in these cells. The current in cell 1 is along the local axis b_1 and the current in cell 2 is along the local axis b_2 . a_1 and a_2 are the other axes in the local coordinate system of the two cells.

The magnetic current density and magnetic current relationship are similarly defined as in [17]

$$M_b \hat{b} \cdot \left(2\hat{n}_{ab} \times \frac{\partial \mathbf{r}}{\partial a} \right) = K_b, \quad (14)$$

where M_b is the magnetic current density, K_b is the magnetic current which has the same direction as M_b , \mathbf{r} is the position vector inside the cell, and \hat{n}_{ab} is the normal vector defined as $\hat{a} \times \hat{b}$. In this example, \hat{n}_{ab} is in the $-z$ direction. The magnetic current density is also related to the E-field in the antipad region as

$$M_b \hat{b} = \mathbf{E} \times \hat{z}. \quad (15)$$

If we substitute (15) into (14), and use the vector identity

$(\vec{a} \times \vec{b}) \cdot (\vec{c} \times \vec{d}) = (\vec{a} \cdot \vec{c})(\vec{b} \cdot \vec{d}) - (\vec{a} \cdot \vec{d})(\vec{b} \cdot \vec{c})$, the following relation can be obtained

$$2(\mathbf{E} \cdot h_a \hat{a}) = K_b. \quad (16)$$

Meanwhile, the electric voltage drop across the cell along the \hat{a} direction can be defined as

$$V_e = 2h_a \hat{a} \cdot \mathbf{E}. \quad (17)$$

Therefore, the total electric voltage drop from via to plane across inductance cell 1 and inductance cell 2 in Fig. 7 is

$$V_e^{\text{via-plane}} = K_{b1} - K_{b2}. \quad (18)$$

If the antipad is electrically small, the voltage drop from the via to the plane should be all the same around the azimuthal direction of the antipad structure. The final result of the voltage drop is evaluated using the averaged values around the antipad region in numerical implementation.

III. GREEN'S FUNCTIONS

A. Spectral Representation of Cavity Green's Function

The Green's function relating the vector magnetic potential to an impressed electric current source inside the cavity can be expressed as [16]

$$\overline{\mathbf{G}}^A(r|r') = \sum_{m=0}^{\infty} \sum_{n=0}^{\infty} \sum_{l=0}^{\infty} A_{mnp} \times \begin{bmatrix} S_x S_{x'} C_y C_{y'} S_z S_{z'} & 0 & 0 \\ 0 & C_x C_{x'} S_y S_{y'} S_z S_{z'} & 0 \\ 0 & 0 & C_x C_{x'} C_y C_{y'} C_z C_{z'} \end{bmatrix}, \quad (19)$$

where:

$$A_{mnp} = \frac{(2 - \delta_m)(2 - \delta_n)(2 - \delta_p)}{abc(k_x^2 + k_y^2 + k_z^2 - k^2)};$$

$$\delta_m = \begin{cases} 0, & m \neq 0 \\ 1, & m = 0 \end{cases};$$

$$k_x = k_{x'} = \frac{m\pi}{a}, k_y = k_{y'} = \frac{n\pi}{b}, k_z = k_{z'} = \frac{p\pi}{c};$$

$$C_\beta = \cos(k_\beta \beta), S_\beta = \sin(k_\beta \beta);$$

$$\beta = x, y, z, x', y', z';$$

and a,b, and c are the x,y, and z dimensions of the cavity.

The Green's function relating the vector electric potential to an impressed magnetic current source inside the cavity can be expressed similarly as

$$\overset{=F}{G}(r|r') = \sum_{m=0}^{\infty} \sum_{n=0}^{\infty} \sum_{l=0}^{\infty} A_{mnp} \times \begin{bmatrix} C_x C_{x'} S_y S_{y'} C_z C_{z'} & 0 & 0 \\ 0 & S_x S_{x'} C_y C_{y'} C_z C_{z'} & 0 \\ 0 & 0 & S_x S_{x'} S_y S_{y'} S_z S_{z'} \end{bmatrix}, (20)$$

The Green's function relating the scalar electric potential to the impressed electric charge density inside the cavity can be expressed as

$$G^q(r|r') = \sum_{m=0}^{\infty} \sum_{n=0}^{\infty} \sum_{l=0}^{\infty} A_{mnp} C_x C_{x'} C_y C_{y'} S_z S_{z'}, (21)$$

The Green's function relating the scalar magnetic potential to the impressed magnetic charge density inside the cavity can be expressed as

$$G^{qm}(r|r') = \sum_{m=0}^{\infty} \sum_{n=0}^{\infty} \sum_{l=0}^{\infty} A_{mnp} S_x S_{x'} S_y S_{y'} C_z C_{z'}, (22)$$

B. Fast Algorithm

The Green's function in (19)~(22) involves triple infinite summation. It is shown in [20] that a lot of terms are needed to get convergence especially when the source point and observation point are close together. Meanwhile, if the source point and the observation point coincide, we will have a singularity in the Green's function evaluation. However, the singularity is difficult to extract if we just use the Green's function expression in (19)~(22) which is called the spectral representation. Another form of Green's function for the cavity problem which is called the spatial expansion is shown in [20] as

$$\overset{=}{G}^A(r|r') = \frac{1}{4\pi} \sum_{m,n,l=-\infty}^{\infty} \sum_{i=0}^7 \begin{bmatrix} C_{Ai}^{xx} & 0 & 0 \\ 0 & C_{Ai}^{yy} & 0 \\ 0 & 0 & C_{Ai}^{zz} \end{bmatrix} \frac{e^{-jkR_{i,mnl}}}{R_{i,mnl}}, \quad (23)$$

$$\text{where } C_{Ai}^{xx} = \begin{cases} +1, i = 0, 2, 5, 7 \\ -1, i = 1, 3, 4, 6 \end{cases}, C_{Ai}^{yy} = \begin{cases} +1, i = 0, 3, 4, 7 \\ -1, i = 1, 2, 5, 6 \end{cases} \text{ and } C_{Ai}^{zz} = +1;$$

$$\overset{=}{G}^F(r|r') = \frac{1}{4\pi} \sum_{m,n,l=-\infty}^{\infty} \sum_{i=0}^7 \begin{bmatrix} C_{Fi}^{xx} & 0 & 0 \\ 0 & C_{Fi}^{yy} & 0 \\ 0 & 0 & C_{Fi}^{zz} \end{bmatrix} \frac{e^{-jkR_{i,mnl}}}{R_{i,mnl}}, \quad (24)$$

$$\text{where } C_{Fi}^{xx} = \begin{cases} +1, i = 0, 1, 4, 5 \\ -1, i = 2, 3, 6, 7 \end{cases}, C_{Fi}^{yy} = \begin{cases} +1, i = 0, 1, 2, 3 \\ -1, i = 4, 5, 6, 7 \end{cases} \text{ and } C_{Fi}^{zz} = \begin{cases} +1, i = 0, 3, 5, 6 \\ -1, i = 1, 2, 4, 7 \end{cases};$$

$$G^q(r|r') = \frac{1}{4\pi} \sum_{m,n,l=-\infty}^{\infty} \sum_{i=0}^7 C_{qi} \frac{e^{-jkR_{i,mnl}}}{R_{i,mnl}}, \quad (25)$$

$$\text{where } C_{qi} = \begin{cases} +1, i = 0, 2, 4, 6 \\ -1, i = 1, 3, 5, 7 \end{cases};$$

$$G^{qm}(r|r') = \frac{1}{4\pi} \sum_{m,n,p=-\infty}^{\infty} \sum_{i=0}^7 C_{qi}^m \frac{e^{-jkR_{i,mnp}}}{R_{i,mnp}}, \quad (26)$$

$$\text{where } C_{qi}^m = \begin{cases} +1, i = 0, 1, 6, 7 \\ -1, i = 2, 3, 4, 5 \end{cases}; \text{ and } R_{i,mnl} = \sqrt{(X_i + 2ma)^2 + (Y_i + 2nb)^2 + (Z_i + 2lc)^2},$$

$$X_i = \begin{cases} x - x', i = 0, 1, 2, 3 \\ x + x', i = 4, 5, 6, 7 \end{cases}, Y_i = \begin{cases} y - y', i = 0, 1, 4, 5 \\ y + y', i = 2, 3, 6, 7 \end{cases}, Z_i = \begin{cases} z - z', i = 0, 2, 4, 6 \\ z + z', i = 1, 3, 5, 7 \end{cases}.$$

The efficient calculation of the Green's function is the combination of the spectral representation and spatial expansion as in [20]. If G_{xx}^A is taken as an example, the expression for the combined expression is shown as

$$G_{xx}^A = G_{xx1}^A + G_{xx2}^A, \quad (27)$$

$$G_{xx1}^A = \sum_{m,n,l=0}^{\infty} A_{mnl} e^{-\frac{(k_x^2+k_y^2+k_z^2-k^2)}{4E^2}} S_x S_{x'} C_y C_{y'} S_z S_{z'}, \quad (28)$$

$$G_{xx2}^A = \frac{1}{4\pi} \sum_{m,n,l=-\infty}^{\infty} \sum_{i=0}^7 C_{Ai}^{xx} \frac{\text{Re} \left[e^{-jkR_{i,mnl}} \text{erfc} \left(R_{i,mnl} E - jk / 2E \right) \right]}{R_{i,mnl}}, \quad (29)$$

where E is a positive real value. The optimized value of E can be chosen by the following expression

$$E_{opt} = \left(\pi^2 \frac{1/a^2 + 1/b^2 + 1/c^2}{a^2 + b^2 + c^2} \right)^{\frac{1}{4}} \quad (30)$$

where a, b, c are the dimensions of the cavity [21].

This fast algorithm needs much fewer terms to achieve convergence. The singularity can also be extracted easily from the spatial expansion at the same time since there is the $1/R$ term in expression (29). A similar singularity extraction method as in [22], [23] is applied here for both scalar and dyadic Green's functions.

C. Singularity Subtraction of Scalar Green's Function

The second portion of the electric scalar Green's function is similar to (29)

$$G_2^q = \frac{1}{4\pi} \sum_{m,n,l=-\infty}^{\infty} \sum_{i=0}^7 C_{qi} f(R), \quad (31)$$

where

$$f(R) = \frac{\text{Re} \left[e^{-jkR_{i,mnl}} \text{erfc} \left(R_{i,mnl} E - jk / 2E \right) \right]}{R_{i,mnl}}. \quad (32)$$

To extract this singularity one can subtract and add a $1/R_p$ term so that $f(R) = f(R) - 1/R_p + 1/R_p$ in which $R_p = |\mathbf{r} - \mathbf{r}_p'|$ and \mathbf{r}_p' is located within the parallelogram corresponding to the original local coordinates of source point \mathbf{r}' as shown in Fig. 8. The red lines

represent the edges of the corresponding parallelogram related to the local coordinates (a_0, b_0) of the observation point.

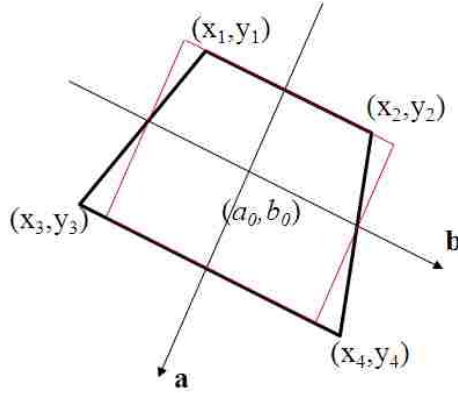


Fig. 8 Create a parallelogram based on the observation point inside a quadrilateral

Note that $1/R_p$ can be integrated analytically over the corresponding parallelogram and the remaining part has a finite value as $R_p \rightarrow 0$. The finite value can be evaluated as

$$\lim_{R_p \rightarrow R, R \rightarrow 0} (f(R) - 1/R_p) \approx f(R(a_0 + \delta, b_0 + \delta)) - \frac{1}{R_p(a_0 + \delta, b_0 + \delta)}, \quad (33)$$

where δ is a small real positive number. Theoretically, a smaller δ gives a closer result. However, if δ is too small, there is a numerical issue in the MATLAB calculation. The optimized value for δ is chosen as $1e-4$ after some numerical experiments.

Only a few terms have singularity in the quadruple summation in (31). Singular terms occur when $m = n = l = i = 0$. In addition, if the source and observation points are located at the walls of the cavity, terms other than $m = n = l = i = 0$ also become singular. For example, if source and observation points are located on the $z = 0$ plane, which is the bottom of the cavity, singular terms occur when $m = n = p = 0$ and $i = 1$. Thus, (31) can be re-written by separating the singular and non-singular terms as

$$G_2^q = G_{\text{ns-terms}} + \frac{1}{4\pi} \sum_{m,n,l,i=\{\text{singular terms}\}} C_{qi} \left[f(R) - \frac{1}{R_p} \right] + \frac{1}{4\pi} \sum_{m,n,l,i=\{\text{singular terms}\}} C_{qi} \frac{1}{R_p}, \quad (34)$$

where $G_{\text{ns-terms}}$ represents all the non-singular terms.

The integral of the $1/R_p$ term over the local coordinates (a', b') in expressions (8) and (11) can be converted to a surface integral over the parallelogram in Fig. 8 as

$$\int_{a'} \int_{b'} \frac{1}{R_p} da' db' = \frac{4}{A_p} \int_{S'} \frac{1}{R_p} ds', \quad (35)$$

where A_p is the area of the parallelogram. The surface integral can be evaluated as [24]

$$\int \frac{1}{R_p} ds' = \sum_{i=1}^4 d_i(\mathbf{r}) \ln \left(\frac{R_i^+(\mathbf{r}) + s_i^+(\mathbf{r})}{R_i^-(\mathbf{r}) + s_i^-(\mathbf{r})} \right), \quad (36)$$

where $R_i^+ = |\mathbf{r} - \vec{p}_i^+|$, $R_i^- = |\mathbf{r} - \vec{p}_i^-|$, $s_i^+ = \hat{s}_i \cdot (\vec{p}_i^+ - \mathbf{r})$ and $s_i^- = \hat{s}_i \cdot (\vec{p}_i^- - \mathbf{r})$. \mathbf{r} is the position vector of the observation point. The definitions of the above vectors are illustrated in Fig. 9.

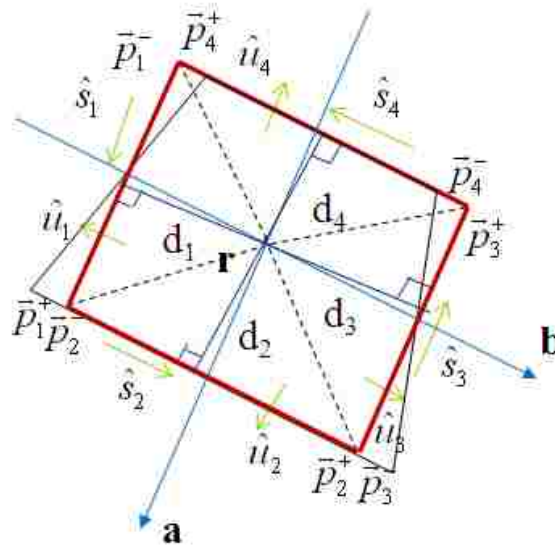


Fig. 9 Illustration of vector definitions for the $1/R_p$ surface integral

The final expression of (8) after singularity subtraction is

$$Pn^e = \frac{1}{\varepsilon} \frac{1}{16} \left\{ \begin{aligned} & \int_a \int_b \int_{a'} \int_{b'} G_1^q + G_{\text{ns-terms}} da' db' dadb \\ & + \int_a \int_b \int_{a'} \int_{b'} \frac{1}{4\pi} \sum_{m,n,l,i=\{\text{singular terms}\}} C_q^i \left[f(R) - \frac{1}{R_p} \right] da' db' dadb \\ & + \int_a \int_b \frac{1}{4\pi} \sum_{m,n,l,i=\{\text{singular terms}\}} C_q^i \frac{4}{A_p} \int_{S'} \frac{1}{R_p} ds' dadb \end{aligned} \right\}, \quad (37)$$

where G_1^q is similarly defined as (28). The rest of the integral is evaluated using the Gaussian quadrature method. The singularity of the corresponding magnetic term in (11) is also subtracted using the same method.

D. Singularity Subtraction of Vector Green's Function

For (27) through (29), the electric vector Green's function can be re-written as

$$\bar{\bar{G}}^A = \bar{\bar{G}}_1^A + \bar{\bar{G}}_2^A, \quad (38)$$

where the first term does not have singularity and the second term has singularity terms.

A similar singularity subtraction method can be used for the second term similarly as the scalar Green's function, and the integral in (7) can be re-written as

$$\begin{aligned} I_{ss'} &= \int_a \int_b \int_{a'} \int_{b'} h_a \hat{a} \cdot h_{a'} \left(\bar{\bar{G}}_1^A + \bar{\bar{G}}_{\text{ns-terms}}^A \right) \hat{a}' da' db' dadb + \int_a \int_b \int_{a'} \int_{b'} h_a \hat{a} \cdot \mathbf{H}_{\text{ns}} da' db' dadb \\ &+ \frac{1}{4\pi} \int_a \int_b h_a \hat{a} \cdot h_{a0} \bar{\bar{A}}_i \hat{a}_0 \frac{4}{A_p} \int_{S'} \frac{1}{R_p} ds' dadb \end{aligned}, \quad (39)$$

where $\bar{\bar{G}}_{\text{ns-terms}}^A$ represents all the non-singular terms in $\bar{\bar{G}}_2^A$. R_p has the same definition as for the scalar Green's function and the same parallelogram is defined as in Fig. 8. h_{a0} , \hat{a}_0 are defined by the position vector of the observation point and they are constant values inside the parallelogram. $\bar{\bar{A}}_i$ is the coefficient of the singular terms shown as

$$\bar{\bar{A}}_i = \sum_{m,n,l,i=\{\text{singular terms}\}} \begin{bmatrix} C_{Ai}^{xx} & 0 & 0 \\ 0 & C_{Ai}^{yy} & 0 \\ 0 & 0 & C_{Ai}^{zz} \end{bmatrix}, \quad (40)$$

where the singular terms are the same as the scalar Green's function. \mathbf{H}_{ns} is shown as

$$\mathbf{H}_{\text{ns}} = h_{a'} \frac{1}{4\pi} f(R) \bar{\bar{A}}_i \hat{a}' - h_{a0} \frac{1}{4\pi R_p} \bar{\bar{A}}_i \hat{a}_0, \quad (41)$$

where $f(R)$ has the same expression as in (32). \mathbf{H}_{ns} has a finite value when $R_p \rightarrow 0$ and it can be evaluated as

$$\lim_{\mathbf{r}' \rightarrow \mathbf{r}} H_{\text{ns}} \approx \frac{1}{4\pi} h_a \hat{a} \cdot \begin{bmatrix} h_{a'} f(R(a+\delta, b+\delta)) \bar{\bar{A}}_i \hat{a}'(a+\delta, b+\delta) \\ -h_{a0} \frac{1}{R_p(a+\delta, b+\delta)} \bar{\bar{A}}_i \hat{a}_0 \end{bmatrix}, \quad (42)$$

where δ is a small number and (a, b) is the local coordinate of the observation point inside the source cell. δ also has a optimized value of 1e-4, just the same as for the scalar Green's function.

The final expression of (7) after singularity subtraction is

$$Lp_{aa'}^e = \frac{\mu}{4} \left\{ \int_a^b \int_{a'}^{b'} \int_{a'}^{b'} h_a \hat{a} \cdot h_{a'} \left(\bar{\bar{G}}_1^A + \bar{\bar{G}}_{\text{ns-terms}}^A \right) \hat{a}' da' db' dadb + \int_a^b \int_{a'}^{b'} \int_{a'}^{b'} \frac{1}{4\pi} h_a \hat{a} \cdot \mathbf{H}_{\text{ns}} da' db' dadb \right. \\ \left. + \int_a^b \int_{a'}^{b'} h_a \hat{a} \cdot h_{a0} \bar{\bar{A}}_i \hat{a}_0 \frac{1}{4\pi} \frac{4}{A_p} \int_{S'} \frac{1}{R_p} ds' dadb \right\}, \quad (43)$$

The rest of the integral is evaluated using the Gaussian quadrature method. The singularity of the corresponding magnetic term in (10) is also subtracted using the same method.

E. Derivative of Vector Green's Function

The curl term in (9) and (12) can be derived as

$$\nabla \times \left(\bar{\bar{G}}^{A,F} \hat{a}' \right) = \left(\nabla \times \bar{\bar{G}}^{A,F} \right) \hat{a}' = \nabla G_{xx}^{A,F} \times x_a \hat{x} + \nabla G_{yy}^{A,F} \times y_a \hat{y} + \nabla G_{zz}^{A,F} \times z_a \hat{z}, \quad (44)$$

where $\hat{a}' = x_a \hat{x} + y_a \hat{y} + z_a \hat{z}$. Take G_{xx}^A for example, the gradient of the Green's function also needs to be decomposed into two parts as in (27). The gradient of the first part is shown as

$$\nabla G_{xx1}^A = \sum_{m,n,l=0}^{\infty} A_{mnl} e^{-\frac{(k_x^2+k_y^2+k_z^2-k^2)}{4E^2}} \nabla S_x S_x' C_y C_y' S_z S_z', \quad (45)$$

where $\nabla S_x S_x' C_y C_y' S_z S_z' = k_x C_x S_x' C_y C_y' S_z S_z' \hat{x} - S_x S_x' k_y S_y C_y' S_z S_z' \hat{y} + S_x S_x' C_y C_y' k_z C_z S_z' \hat{z}$.

The gradient of the second part is shown as

$$\nabla G_{xx2}^A = \frac{1}{4\pi} \sum_{m,n,l=-\infty}^{\infty} \sum_{i=0}^7 C_{Ai}^{xx} \frac{df(R_{i,mnl})}{dR} \nabla R_{i,mnl}, \quad (46)$$

where

$$\frac{df(R_{i,mnl})}{dR} = -\frac{1}{R^2} \left\{ \frac{2ER}{\sqrt{\pi}} e^{-E^2 R^2 + \frac{k^2}{4E^2}} + \text{Re} \left[(1 + jkR) e^{-jkR} \text{erfc} \left(ER - \frac{jk}{2E} \right) \right] \right\}$$

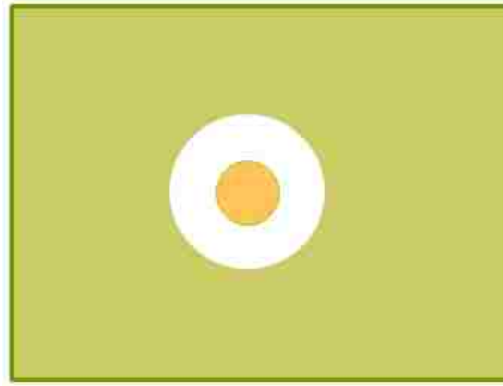
and

$$\nabla R_{i,mnl} = \frac{X_i + 2ma}{R_{i,mnl}} \hat{x} + \frac{Y_i + 2nb}{R_{i,mnl}} \hat{y} + \frac{Z_i + 2lc}{R_{i,mnl}} \hat{z}.$$

IV. RESULTS AND VALIDATIONS

The simple one via structure in Fig. 10 is used for the validation of the proposed method. The via radius is defined as 9 mils or 25 mils, and the antipad radius is defined as 30 mils. The cavity dimension is 200 x 200 x 10 mils and the via is located at the center of the cavity. The permittivity of the dielectric in the cavity is 4.0. Ports are defined in the antipad region on the top and the bottom of the cavity. The Z-parameters are calculated at two frequency points (low frequency -- 100 MHz, high frequency -- 20 GHz) using both the proposed method and commercial finite element solver HFSS [25].

The results are compared in Table I. “Rv” denotes the radius of the via and “PEEC” denotes the results of the proposed PEEC method. The voltage drop from the via to the plane is calculated using (18) in the proposed method.



(a) Top view



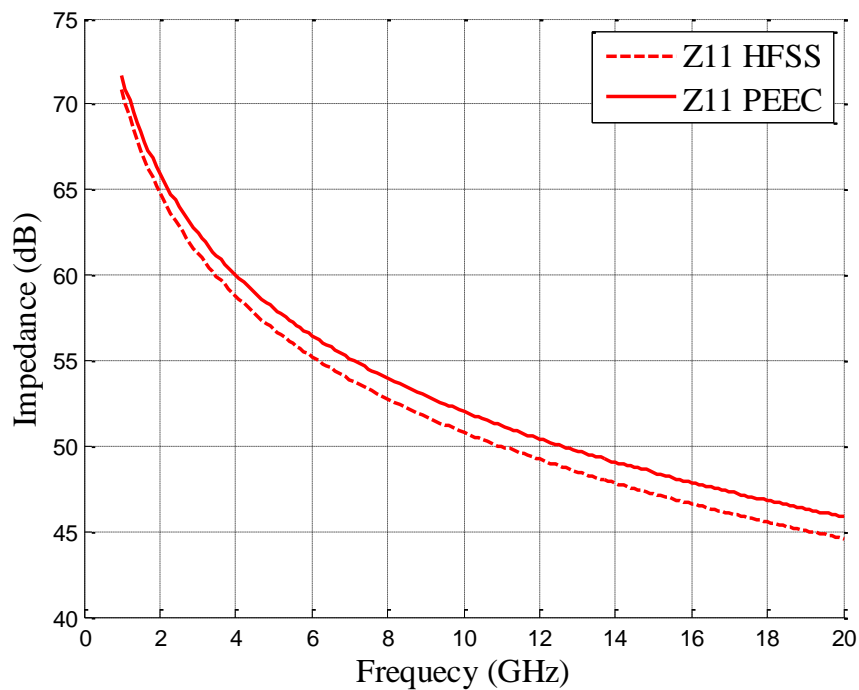
(b) Side view

Fig. 10 Simple one via structure with circular antipad

Table I
Results Comparison for One Via Structure

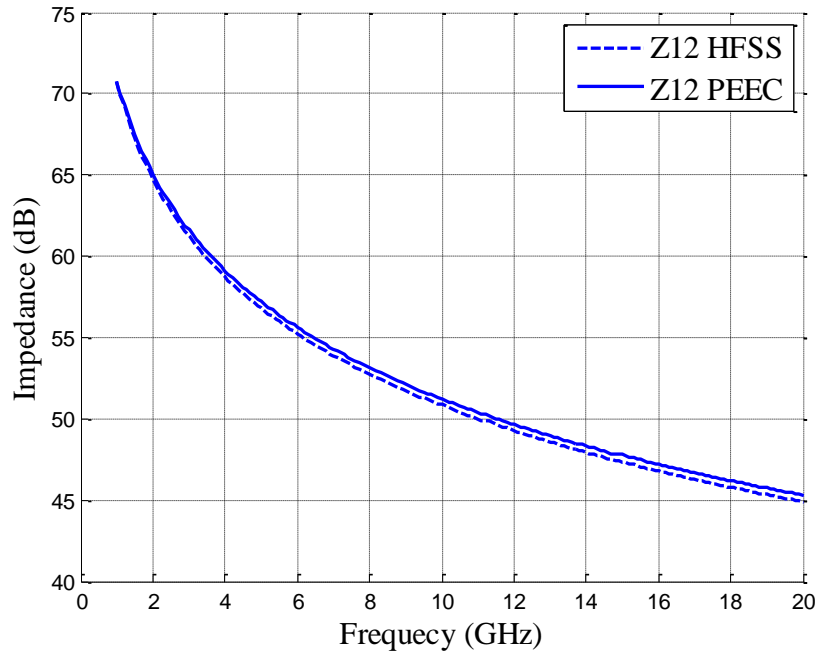
		PEEC	HFSS
20 GHz (Rv=9 mils)	Z11 (dB)	45.9	44.6
20 GHz (Rv=9 mils)	Z12 (dB)	45.3	44.9
100 MHz (Rv=25 mils)	Z11 (dB)	78.6	76.3
100 MHz (Rv=25 mils)	Z12 (dB)	75.9	76.0

The results show a strong agreement between the two methods, which validates the proposed method. Such strong correlation is achieved by using a relatively sparse mesh in the proposed method: two mesh nodes in the radial direction, and six mesh nodes in the azimuthal direction in the antipad region; two nodes in the z-direction on the via surface. The comparison for a frequency span of 1 GHz ~ 20 GHz with 0.1 GHz step is also shown in Fig. 11 to further validate the proposed method.



(a)

Fig. 11 Z-parameter comparison for one-via structure



(b)

Fig. 11 Z-parameter comparison for one-via structure (cont.)

The shared antipad structure in Fig. 1 is also simulated using the proposed method and HFSS. The differential Z-parameters are compared in Table II. The via radius is 9 mils and the antipad radius is 30 mils. The pitch size between the two vias is 40 mils. The cavity has the same dimension and dielectric constant value as in the one-via structure in Fig. 10. Mixed-mode ports are defined in the antipad region at the top and bottom of the cavity.

These results also show a strong agreement. The differential voltage is calculated using a similar method as discussed in Section II.D. As illustrated in Fig. 12, the voltage drop from the left via to the plane is defined as K_5-K_{19} and the one from the right via to the plane is $K_{25}-K_{33}$. Thus, the differential voltage is defined as $VDD = (K_5-K_{19})-(K_{25}-K_{33})$. The differential Z-parameters can then be calculated by dividing the VDD by a 1A

current since a simulated 1A current is injected into the left via and a simulated -1A current is injected into the right via in this simulated model. The mesh in the antipad region is also shown in Fig. 12. The mesh on the via surface has the same size as the one-via structure. The close results in Table II are also achieved by using a relatively sparse mesh for the shared-antipad structure.

Table II
Results Comparison for Shared-Antipad Via Structure

		PEEC	HFSS
20 GHz	ZDD11 (dB)	51.3	49.8
20 GHz	ZDD12 (dB)	50.6	50.0
100 MHz	ZDD11 (dB)	97.4	97.1
100 MHz	ZDD12 (dB)	96.4	97.1

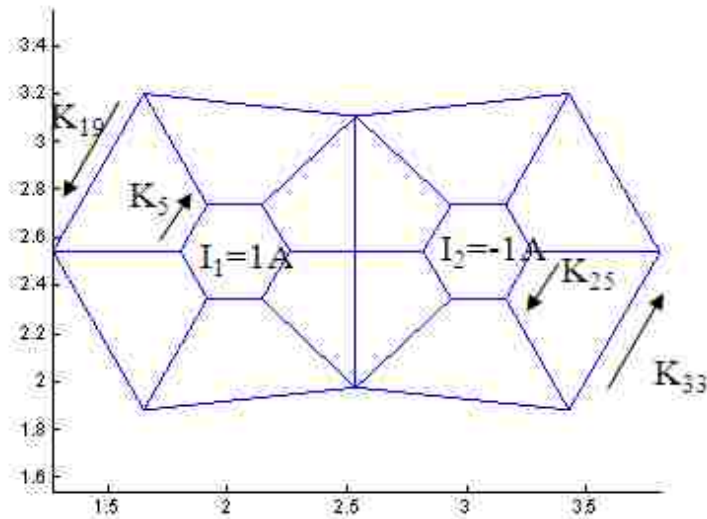
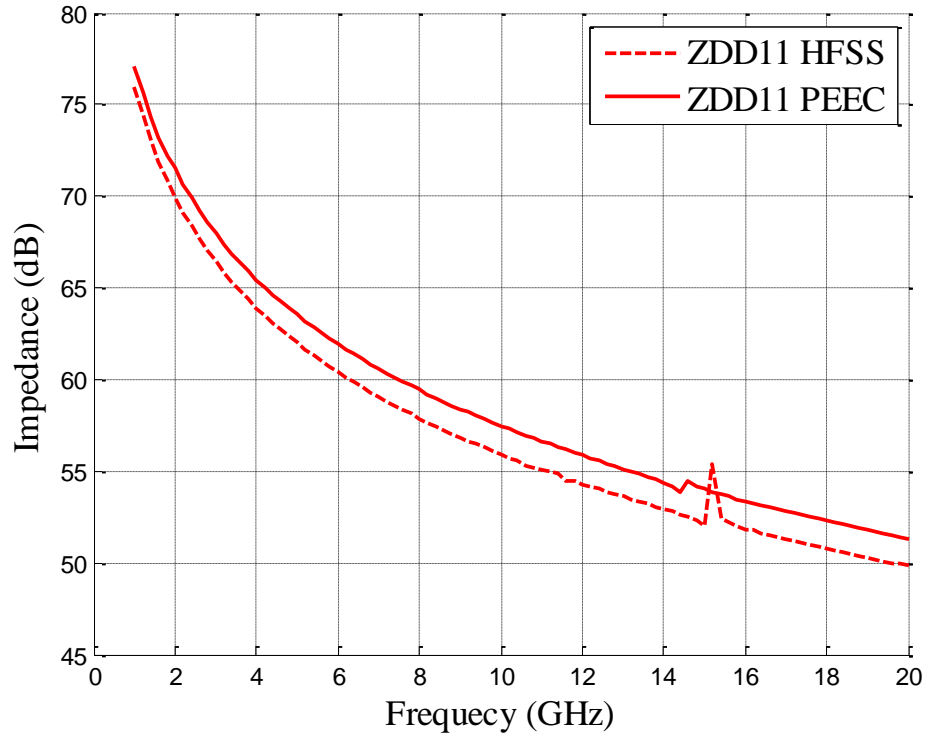


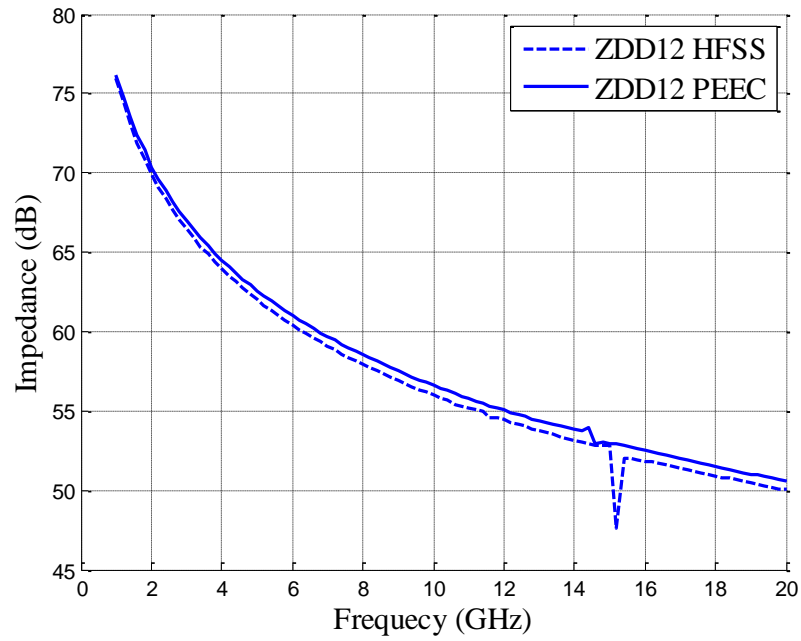
Fig. 12 Illustration of the differential voltage calculation for shared-antipad structure

The comparison for a frequency span of 1 GHz ~ 20 GHz with 0.2 GHz step is also shown in Fig. 13 and Fig. 14 for differential and common Z-parameters to further validate the proposed method.



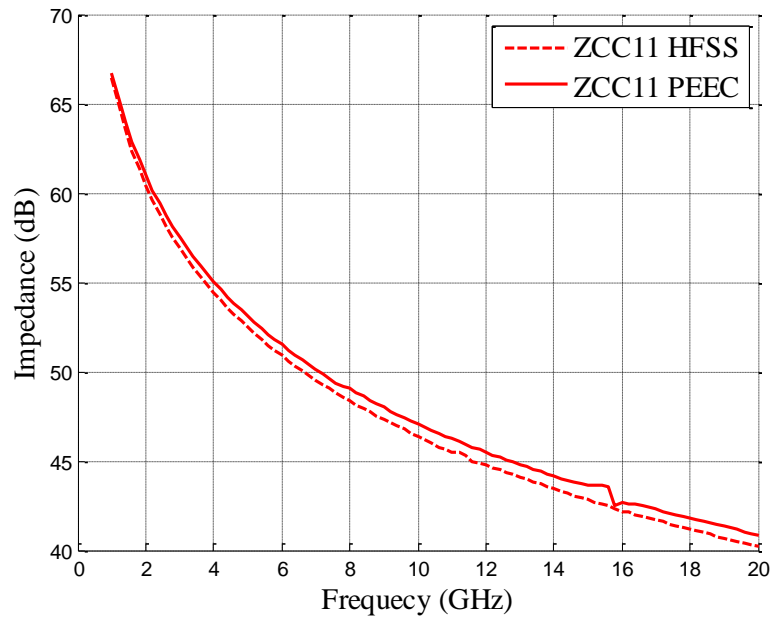
(a)

Fig. 13 Differential Z-parameter comparison for shared-antipad structure



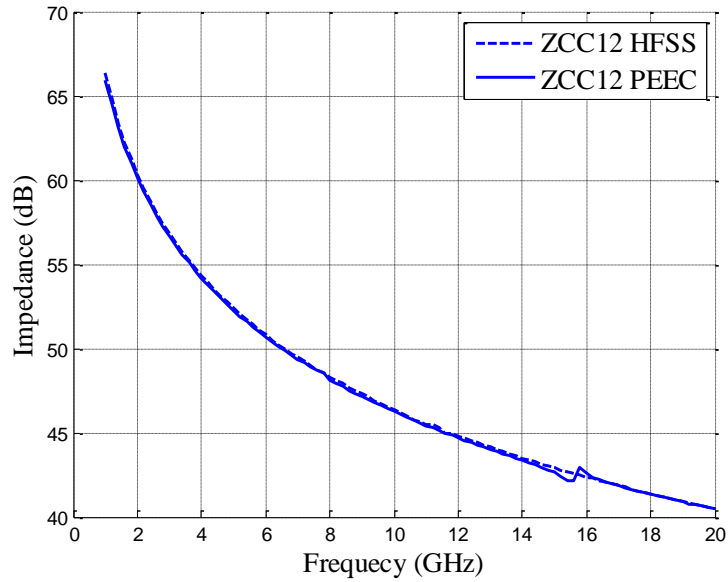
(b)

Fig. 13 Differential Z-parameter comparison for shared-antipad structure (cont.)



(a)

Fig. 14 Common Z-parameter comparison for shared-antipad structure



(b)

Fig. 14 Common Z-parameter comparison for shared-antipad structure (cont.)

V. CONCLUSIONS

A rigorous modeling method of a shared-antipad via structure is developed using surface PEEC with the cavity Green's function. The advantage of using the cavity Green's function is that much fewer mesh cells are needed for the via structure. The values of the equivalent circuit elements are derived based on the non-orthogonal mesh in the antipad region and the rectangular mesh on the via surface. In order to characterize the via transition parameters, a novel wave port excitation method is developed to stimulate the equivalent circuit.

The proposed method is validated using a commercial finite element solver. Strong correlation of Z-parameter results are achieved for both the traditional, simple one-via structure and the shared-antipad structure which, is widely used in differential via design.

The PEEC calculated by the proposed method can be further used to connect to either the parallel plane model or other transmission line models of the trace to do the circuit simulation of the whole system. Multiple PEEC's of the proposed method can also be stacked together to model the multi-layer PCB problems; this modeling can be the future work of this study.

APPENDICES

The calculation of all the equivalent circuit elements is implemented in “main_function.m” for the two vias shared-antipad case and “test_circular_apad.m” is for the one via traditional circular antipad case.

A. Non-Orthogonal Quadrilateral and Local Coordinates

Non-orthogonal quadrilateral mesh is used on the antipad region and rectangular mesh is used on the via surface. However, the rectangular can also be treated as a special type of quadrilateral. The formulation utilizes a *global* as well as a *local* coordinate system. The key *global* coordinate system uses conventional orthogonal coordinates where a global vector \mathbf{F} is of the form $\mathbf{F} = F_x\hat{\mathbf{x}} + F_y\hat{\mathbf{y}} + F_z\hat{\mathbf{z}}$. Therefore, the global unit vectors $\hat{\mathbf{x}}$, $\hat{\mathbf{y}}$ and $\hat{\mathbf{z}}$ are position independent. We mark a vector in the global coordinates as \mathbf{r} for a clear distinction from the local coordinates. The *local* coordinates a, b are used to separately represent each specific possibly non-orthogonal quadrilateral. We call the unit vectors \hat{a}, \hat{b} . First, we very briefly introduce the local coordinate system we use for a quadrilateral element shown in Fig. 15. The purpose of the local coordinates is to identify the location of any point belonging to the quadrilateral in terms of the variables a, b where $a, b \in [-1, +1]$. The purpose of all this is to uniquely map a point a, b into a point in the global coordinates \mathbf{r} . We accomplish this by specifying four vectors \mathbf{r}_i where $i=0\sim 3$

with the coordinates x_i, y_i, z_i . It will be clear that the corners of the quadrilateral are reached when $a, b = \pm 1$.

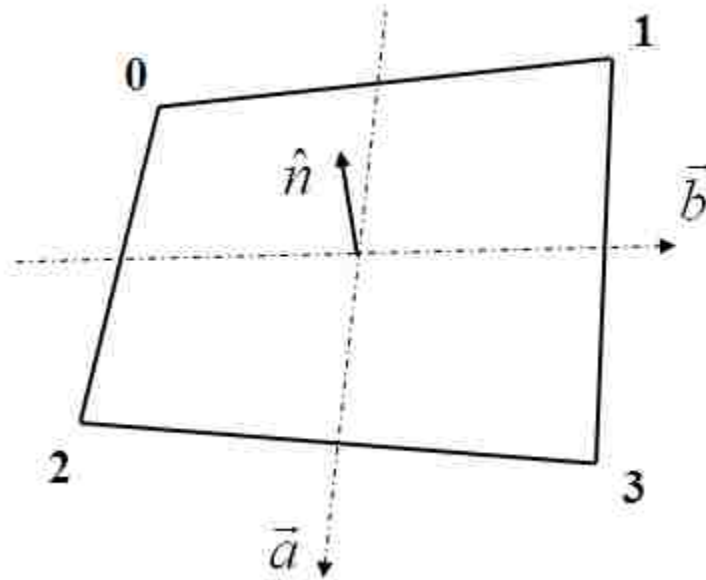


Fig. 15 Local coordinates of a quadrilateral

Next, we create clean assignment of the corner indices in Fig. 15, for the quadrilateral using a binary code for the symbols a, b , where the -1 coordinates map into logical zeros, and 1 coordinates map into logical ones. The order of the logical variables is ab . Hence, for example, the binary code $ab=01$ corresponds to the corner $a=0, b=0$ and its decimal equivalent is 1 for corner 1 as can be verified in Fig. 15. This makes the assignment unique and easy to remember. As indicated above, all local coordinates have to relate back to the global coordinates. Therefore, a unique representation is needed for the mapping from a local point a, b on a quadrilateral to the global point \mathbf{r} . Mapping a point in the above quadrilateral from a local coordinate point a, b into a global coordinate point x, y, z is described by

$$\begin{aligned}
x &= \sum_{i=0}^3 N_i(a,b) x_i \\
y &= \sum_{i=0}^3 N_i(a,b) y_i, \\
z &= \sum_{i=0}^3 N_i(a,b) z_i
\end{aligned} \tag{47}$$

where the coefficients are given by

$$\begin{aligned}
N_0 &= \frac{1}{4}(1-a)(1-b) \\
N_1 &= \frac{1}{4}(1-a)(1+b) \\
N_2 &= \frac{1}{4}(1+a)(1-b) \\
N_3 &= \frac{1}{4}(1+a)(1+b)
\end{aligned} \tag{48}$$

With this, we are in a position to also express the tangential vectors with respect to the local coordinates as

$$\begin{aligned}
\frac{\partial \mathbf{r}}{\partial a} &= \frac{\partial x}{\partial a} \hat{\mathbf{x}} + \frac{\partial y}{\partial a} \hat{\mathbf{y}} + \frac{\partial z}{\partial a} \hat{\mathbf{z}} \\
\frac{\partial \mathbf{r}}{\partial b} &= \frac{\partial x}{\partial b} \hat{\mathbf{x}} + \frac{\partial y}{\partial b} \hat{\mathbf{y}} + \frac{\partial z}{\partial b} \hat{\mathbf{z}}
\end{aligned} \tag{49}$$

where the derivatives are found from (47) and (48). Finally, the magnitude of the tangential vector is shown as

$$h_{a,b} = \left| \frac{\partial \mathbf{r}}{\partial a, b} \right|, \tag{50}$$

where the position dependent unit vectors can be determined as

$$\hat{\mathbf{a}}, \hat{\mathbf{b}} = \frac{\partial \mathbf{r} / \partial a, \partial b}{h_{a,b}}. \tag{51}$$

The above formulation gives the conversion formula from local coordinates to global coordinates and is implemented in “local2Glob.m”. The opposite direction, which is the conversion formula from global coordinates to local coordinates, can be obtained by solving the following set of equations

$$\begin{bmatrix} x \\ y \\ z \end{bmatrix} = \frac{1}{4} \begin{bmatrix} -x_0 - x_1 + x_2 + x_3 & -x_0 + x_1 - x_2 + x_3 & x_0 - x_1 - x_2 + x_3 \\ -y_0 - y_1 + y_2 + y_3 & -y_0 + y_1 - y_2 + y_3 & y_0 - y_1 - y_2 + y_3 \\ -z_0 - z_1 + z_2 + z_3 & -z_0 + z_1 - z_2 + z_3 & z_0 - z_1 - z_2 + z_3 \end{bmatrix} \begin{bmatrix} a \\ b \\ ab \end{bmatrix} + \frac{1}{4} \begin{bmatrix} \sum_{i=0}^3 x_i \\ \sum_{i=0}^3 y_i \\ \sum_{i=0}^3 z_i \end{bmatrix}. \quad (52)$$

There are totally three equations to solve two unknowns a, b . Thus, any two of the non-zero equations can be used to solve the unknowns. Take the first two equations as an example, (52) can be re-arranged as

$$\begin{pmatrix} X \\ Y \end{pmatrix} = \left(4 \begin{bmatrix} x \\ y \end{bmatrix} - \begin{bmatrix} \sum_{i=0}^3 x_i \\ \sum_{i=0}^3 y_i \end{bmatrix} \right) = \begin{bmatrix} X_a & X_b & X_{ab} \\ Y_a & Y_b & Y_{ab} \end{bmatrix} \begin{bmatrix} a \\ b \\ ab \end{bmatrix}, \quad (53)$$

where $X_a = -x_0 - x_1 + x_2 + x_3$, $X_b = -x_0 + x_1 - x_2 + x_3$, and $X_{ab} = x_0 - x_1 - x_2 + x_3$; $Y_a = -y_0 - y_1 + y_2 + y_3$, $Y_b = -y_0 + y_1 - y_2 + y_3$, and $Y_{ab} = y_0 - y_1 - y_2 + y_3$.

Finally, a, b can be solved by the following quadratic equations derived from (53)

$$\begin{aligned} (X_{ab}Y_a - X_aY_{ab})a^2 + (X_bY_a - X_aY_b + XY_{ab} - X_{ab}Y)b + XY_b - X_bY &= 0 \\ (X_bY_{ab} - X_{ab}Y_b)b^2 + (X_bY_a - X_aY_b + X_{ab}Y - XY_{ab})b + X_aY - XY_a &= 0 \end{aligned} \quad (54)$$

The conversion from global coordinates to local coordinates is implemented in “Glob2local.m”.

B. Mesh Creation

All the surfaces in the via structure, including antipad, via outer surface, are meshed into quadrilaterals. The quadrilateral mesh is stored in two matrices: “nodes” and “quads”, where “nodes” stores the coordinates of all the nodes of the quadrilaterals and “quads” stores the indices of the vertices of all the quadrilaterals.

For the traditional circular antipad, the shape of the antipad is like a ring. The number of mesh in azimuthal direction “tnum” and the number of mesh in radial direction “rnum” need to be specified to generate the mesh. The circular antipad is finally approximated as a polygon shown as in Fig. 7. This is implemented in “createRing.m”.

For the shared-antipad structure, the same “tnum” and “rnum” are used to define the mesh density in the antipad region. The antipad surface is divided into two by the center line between the two vias, and at each half of the antipad, quadrilateral mesh is created similarly as the traditional circular antipad. The duplicated nodes of the right half at the center line will be assigned the value “nan”. One example of the mesh is shown in Fig. 3 when tnum=6 and rnum=2. Other examples are shown in Fig. 16 with different “tnum” and “rnum”. This is implemented in “createApad.m”.

The circular via is first approximated as an n-edges polygon defined by “tnum”, and then the outer surface of the via can be discretized into rectangular mesh. The mesh density in z-direction is defined by “znum”. This is implemented in “createVia.m”.

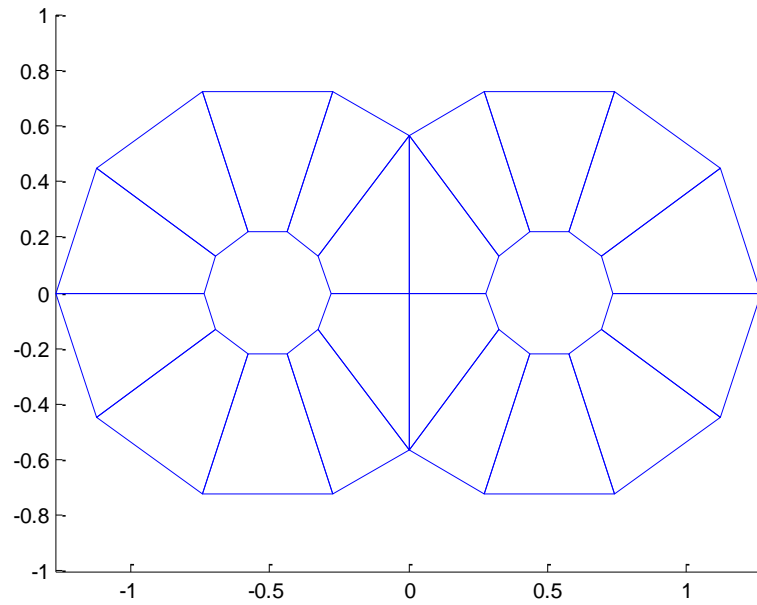
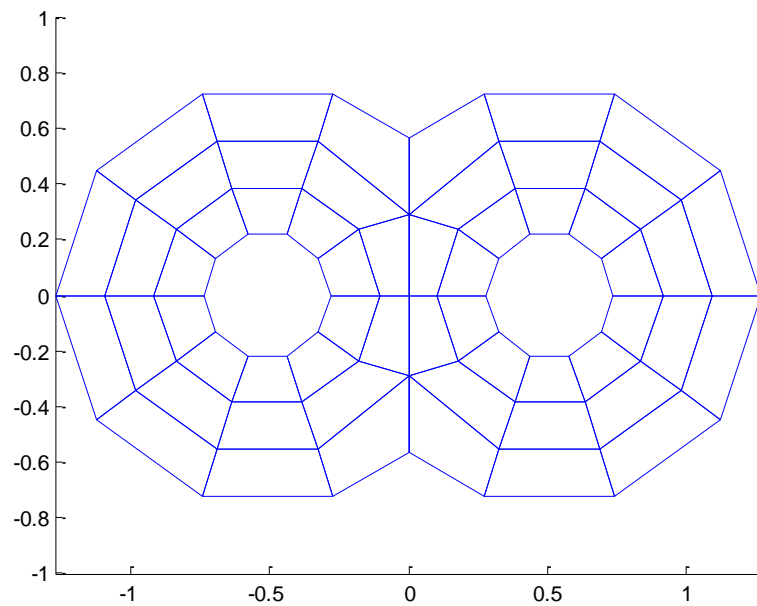
(a) $tnum=10, rnum=2$ (b) $tnum=10, rnum=3$

Fig. 16 Illustrations of different mesh density in the shared-antipad

C. Generate Capacitance Cells and Inductance Cells

After creating the base mesh, which defines the circuit nodes (vertices) and current branches (edges), capacitance cells and inductance cells are further generated. Capacitance cells are generated based on the circuit nodes and inductance cells are generated based on the current branches.

Each quadrilateral is divided into four parts in the following way shown as in Fig. 17: four vertices of each part include a vertex of the quadrilateral, the center point and two middle points of the connecting edges of that vertex. Every part corresponds to a quarter capacitance cell (shown as in Fig. 3) associated with the vertex belonging to this part. Thus, every node may have 1, 2 or 4 quarter capacitance cells attached to it. Each row of the matrix used to store the capacitance cells includes the information of the number of the sub quarter capacitance cell and the coordinates of the vertices of these sub cells. The generation of the capacitance cells is implemented in “gen_capcells.m”. If the quadrilateral is rectangle, the sub cells may be able to combined together to form a big rectangle as a half capacitance cell or a full capacitance cell. This is implemented in “mergeCap2Cells.m” and “mergeCap4cells.m”, respectively.

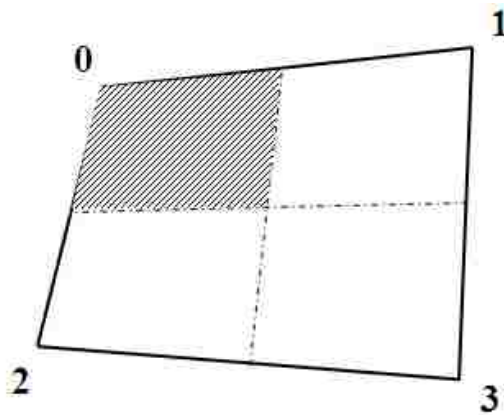


Fig. 17 Illustration of a quarter capacitance cell in a quadrilateral

Each quadrilateral is also divided into four parts in the following way shown as in Fig. 18: four edges of each part include one edge of the quadrilateral, center line in the same direction as that edge and two half edges between them. Every part corresponds to a half inductance cell (shown as in Fig. 3) associated with the edge belonging to this part. Thus, every edge may have 1 or 2 half inductance cells attached to it. Each row of the matrix used to store the inductance cells includes the information of the number of the sub half inductance cell, the coordinates of the vertices of these sub cells and the current direction of the sub cells. The information of all the edges is stored in a sparse matrix, which is generated by “gen_conn_mat.m”. The generation of the inductance cells is implemented in “gen_indcells.m”. If the quadrilateral is rectangle, the sub cells may be able to combined together to form a big rectangle as a full inductance cell. This is implemented in “mergeInd2Cells.m”.

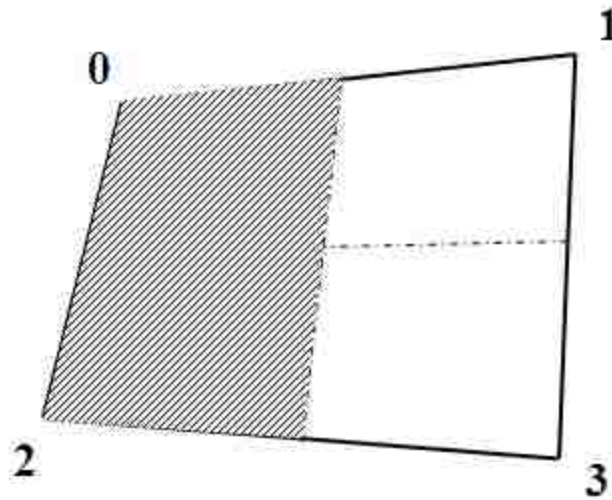


Fig. 18 Illustration of a half inductance cell in a quadrilateral

D. Derivation of Equivalent Circuit Elements

1) Equivalent Partial Inductance L_p

The current density and current relationship in the local coordinates of the non-orthogonal quadrilateral is defined as (take the a -direction current for example)

$$J_a \hat{a} \cdot \left(2 \frac{\partial \mathbf{r}}{\partial b} \times \hat{n} \right) = I_a. \quad (55)$$

Using the vector identity $(\hat{a} \times \hat{b}) \cdot \hat{c} = (\hat{c} \times \hat{a}) \cdot \hat{b}$, the following relationship between current density J_a and current I_a can be obtained

$$J_a = \frac{h_a I_a}{2 \left| \frac{\partial \mathbf{r}}{\partial a} \times \frac{\partial \mathbf{r}}{\partial b} \right|} = w_a I_a, \quad (56)$$

where $w_a = \frac{h_a}{2 \left| \frac{\partial \mathbf{r}}{\partial a} \times \frac{\partial \mathbf{r}}{\partial b} \right|}$.

The electric field is connected with the circuit voltage through the inner product

$$V_a = \iint_{a \ b} w_a \hat{a} \cdot \mathbf{E} \left| \frac{\partial \mathbf{r}}{\partial a} \times \frac{\partial \mathbf{r}}{\partial b} \right| da db. \quad (57)$$

Each of the three terms on the rhs of (1) yields a voltage drop across a circuit element by applying the inner product operation (57). The first term corresponds to the partial inductor voltage drop shown as

$$V_a^L = j\omega \iint_{a \ b} w_a \hat{a} \cdot \mathbf{A}(J_{a'}) \left| \frac{\partial \mathbf{r}}{\partial a} \times \frac{\partial \mathbf{r}}{\partial b} \right| da db. \quad (58)$$

Substituting the value of the vector potential from (3) into (58) yields

$$V_a^L = j\omega\mu \iint_{a \ b} w_a \hat{a} \cdot \iint_{a' \ b'} w_{a'} I_{a'} \bar{\bar{G}}^A \hat{a}' \left| \frac{\partial \mathbf{r}'}{\partial a'} \times \frac{\partial \mathbf{r}'}{\partial b'} \right| da' db' \left| \frac{\partial \mathbf{r}}{\partial a} \times \frac{\partial \mathbf{r}}{\partial b} \right| da db, \quad (59)$$

where the inner product of \hat{a} and $\bar{\bar{G}}^A \hat{a}'$ can be evaluated as

$$\hat{a} \cdot \bar{\bar{G}}^A \hat{a}' = \begin{bmatrix} x_a \\ y_a \\ z_a \end{bmatrix} \cdot \begin{bmatrix} G_{xx} & & \\ & G_{yy} & \\ & & G_{zz} \end{bmatrix} \begin{bmatrix} x_{a'} \\ y_{a'} \\ z_{a'} \end{bmatrix} = G_{xx}^A x_{a'} x_a + G_{yy}^A y_{a'} y_a + G_{zz}^A z_{a'} z_a, \quad (60)$$

where $\hat{a} = x_a \hat{x} + y_a \hat{y} + z_a \hat{z}$ and $\hat{a}' = x_{a'} \hat{x} + y_{a'} \hat{y} + z_{a'} \hat{z}$. From (59) we can get the electric partial inductor expression as in (7). The derivation of the magnetic partial inductor expression in (10) is similar as the electric partial inductor. The quadruple integral is evaluated using 3-points Gaussian quadrature if no singularity is involved

$$Lp_{aa'} = (\mu, \varepsilon) \sum_{i=1}^3 \sum_{j=1}^3 \sum_{m=1}^3 \sum_{n=1}^3 \frac{1}{4} w_i w_j w_m w_n f(\xi_i, \eta_j, \mu_m, \nu_n), \quad (61)$$

where w_i, w_j, w_m, w_n are the weighting coefficient of the Gaussian quadrature; $\xi_i, \eta_j, \mu_m, \nu_n$ are the sampling points of the quadrature method; and the function f corresponds to

$$f(a, b, a', b') = h_a \hat{a} \cdot h_{a'} \bar{\bar{G}}^{A,F}(\mathbf{r}(a, b), \mathbf{r}'(a', b')) \hat{a}'. \quad (62)$$

The calculation of the equivalent partial inductance is implemented in “Eval_ind.m” with the dyadic Green’s function implemented in “GF_dyadic.m”. The Gaussian quadrature points and weighting coefficient is generated by “lgwt.m”

2) Equivalent Partial Coefficients of Potential Pp

The charge density and the total charge on one cell can be expressed as

$$q_s = \frac{Q_j}{4 \left| \frac{\partial \mathbf{r}'}{\partial a'} \times \frac{\partial \mathbf{r}'}{\partial b'} \right|}, \quad (63)$$

since

$$Q_j = \int_{S'} q_s ds' = \int_{a'} \int_{b'} \frac{Q_j}{4 \left| \frac{\partial \mathbf{r}'}{\partial a'} \times \frac{\partial \mathbf{r}'}{\partial b'} \right|} \left| \frac{\partial \mathbf{r}'}{\partial a'} \times \frac{\partial \mathbf{r}'}{\partial b'} \right| da' db' = Q_j, \quad (64)$$

where a' and b' are integrated from -1 to 1.

The potential at the point \mathbf{r} and the charge density on the source cell is related by the scalar Green's function for both electric and magnetic capacitance cell as

$$\Phi(\mathbf{r}) = \frac{1}{\varepsilon, \mu} \int_{s'} \frac{Q_j}{4 \left| \frac{\partial \mathbf{r}'}{\partial a'} \times \frac{\partial \mathbf{r}'}{\partial b'} \right|} G^{q, q_m}(\mathbf{r}, \mathbf{r}') ds' = \frac{1}{\varepsilon, \mu} Q_j \int_{a'} \int_{b'} \frac{1}{4} G^{q, q_m}(\mathbf{r}, \mathbf{r}') da' db'. \quad (65)$$

If the potential is further averaged over the observation cell using the Galerkin's method, which is expressed as

$$\Phi_i = \int_s \frac{\Phi(\mathbf{r})}{4 \left| \frac{\partial \mathbf{r}}{\partial a} \times \frac{\partial \mathbf{r}}{\partial b} \right|} ds = \int_a \int_b \frac{1}{4} \Phi(\mathbf{r}) dadb, \quad (66)$$

The partial coefficients of potential Pp , which relates the averaged potential on the observation cell and the total charge on the source cell, can be derived from (65) and (66) to get (8) and (11). The quadruple integrals can also be similarly solved by using the 3-point Gaussian quadrature method if no singularity is involved

$$Pp = \frac{1}{\varepsilon, \mu} \sum_{i=1}^3 \sum_{j=1}^3 \sum_{m=1}^3 \sum_{n=1}^3 \frac{1}{16} w_i w_j w_m w_n f(\xi_i, \eta_i, \mu_m, \nu_n), \quad (67)$$

where the function f corresponds to

$$f(a, b, a', b') = G^{q, q_m}(\mathbf{r}(a, b), \mathbf{r}'(a', b')). \quad (68)$$

The calculation of the equivalent partial coefficients of potential is implemented in "Eval_cap.m" with the scalar Green's function implemented in "GF_scalar.m".

3) Equivalent EM Coupling Terms

The third term on the rhs of (1) yields the EM-coupling voltage drop by applying the inner product operation (57)

$$V_a^{E-M} = \int_a \int_b w_a \hat{a} \cdot \left[\frac{1}{\varepsilon} \nabla \times \mathbf{F}(K_{a'}) \right] \left| \frac{\partial \mathbf{r}}{\partial a} \times \frac{\partial \mathbf{r}}{\partial b} \right| dadb. \quad (69)$$

Substituting the value of the vector potential from (4) into (69) yields

$$V_a^{E-M} = \int_a \int_b w_a \hat{a} \cdot \nabla \times \int_{a'} \int_{b'} w_{a'} K_{a'} \bar{\bar{G}}^F \hat{a}' \left| \frac{\partial \mathbf{r}'}{\partial a'} \times \frac{\partial \mathbf{r}'}{\partial b'} \right| da' db' \left| \frac{\partial \mathbf{r}}{\partial a} \times \frac{\partial \mathbf{r}}{\partial b} \right| dadb, \quad (70)$$

which can be simplified to (9). (12) can be similarly derived. These are implemented in “Eval_EM.m”.

The derivation of the curl terms in (9) and (12) is shown in Section III.E and is implemented in “GF_dyadic_gradient.m”, which calculates the gradient of the dyadic Green’s function.

4) Singularity Extraction

The derivation of the singularity extraction is shown in Section III.C-D. Several sub functions are used in the evaluation of some of the terms in the derivation: (33) is implemented in “Scalar_RemoveRp.m”; (36) is implemented in “Integral_InverseR.m”; (41) and (42) is implemented in “Dyadic_RemoveRp.m”.

Several geometry related sub functions are also used to help to handle the singularity extraction. In order to judge if there is singularity in the calculation, we need to judge if the quadrature point of the observation cell is inside the source cell, which is implemented in “inquad3d.m”. The corresponding parallelogram also needs to be generated, which is implemented in “Find_parallelogram.m”. The area of the quadrilateral is calculated in “quad_area.m”, which can be used to evaluate (35).

The final expression of Pp and Lp as in (37) and (43), when singularity is involved, is implemented in “Eval_cap.m” and “Eval_ind.m”, respectively.

Special care needs to be taken when the source cell and the observation cell partially overlap with each other, which only occurs for the partial inductance evaluation. 3-point Gaussian quadrature is not enough to get reciprocal results for the mutual partial

inductance. Numerical experiments found 7-point Gaussian quadrature is needed to get reciprocal results. Thus, “if_overlap.m” is used to judge if the two cells are overlapped with each other and if so, 7 point Gaussian quadrature is used.

5) *Equivalent Magnetic Voltage Source Due to Wave Port Excitation*

The description of the wave port excitation method is shown in Section II.D. The 2D finite element analysis is processed in the antipad region using the MATLAB PDE Toolbox. “Waveport_EvalInductance.m” is first implemented to evaluate the inductance matrix of the two vias of the shared-antipad case in Fig. 1. Then, using the calculated inductance matrix, “Waveport_EvalHfield.m” is implemented to evaluate the H-field distribution in the antipad region for the specific current injection into two vias.

“Waveport_EvalInductance_ring.m” and “Waveport_EvalHfield_ring.m” have the same functionality for the one via test case in Fig. 10.

After getting the H-field, the equivalent voltage source is calculated through (13) using Gaussian quadrature, which is implemented in “Eval_Vsource.m” with the sub function “GetHfield.m” to get the H-field value at the specific point.

E. Approximation Study

Approximate calculation methods can be used to evaluate equivalent circuit elements when the cells are far apart. The distance to size ratio is defined as in Fig. 19 and (71). This is implemented in “dist2size.m”.

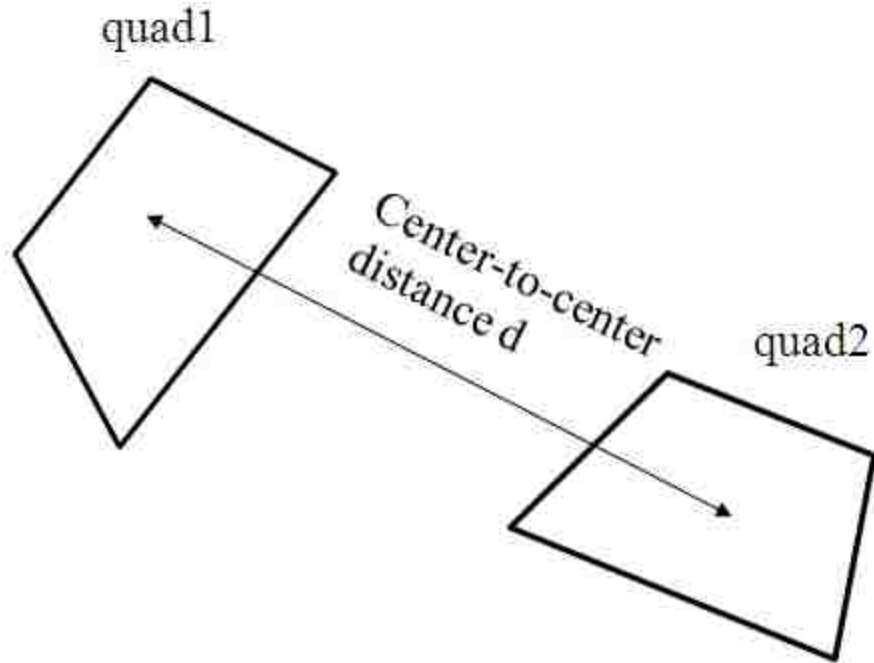


Fig. 19 Distance to ratio definition

$$d2s = \frac{d}{\max(\max_edge(quad1), \max_edge(quad2))}. \quad (71)$$

1) *Equivalent partial inductance L_p*

If all the current directions in one cell are perpendicular to the ones inside the other cell, the partial inductance is zero. In addition, numerical experiments give the following approximation criteria.

For the electric inductance cells whose currents are not in z-direction, when $d2s > 2$, the mutual partial inductance is 10^{-4} of the self partial inductance, and can be approximated as 0.

In addition to the above approximation, for the cells on the side walls, when $d2s > 5$, point-to-point approximation can be used for the mutual inductance calculation, which means Green's function value is assumed to be constant across the quadrilateral

cells as the value evaluated at the center of the quadrilateral. For the cells on the via surface, the criterion is $d2s > 2$. For the mutual inductance between the cell on the via surface and the cell on the side walls, the criterion is $d2s > 8$. The point-to-point approximation is expressed as

$$\begin{aligned} Lp_{aa'} &= (\mu, \varepsilon) \int_a \int_b \int_{a'} \int_{b'} \frac{1}{4} h_a \hat{a} \cdot h_{a'} \bar{\bar{G}}^{A,F}(\mathbf{r}, \mathbf{r}') \hat{a}' da' db' dadb \\ &\approx (\mu, \varepsilon) \int_a \int_b \int_{a'} \int_{b'} \frac{1}{4} h_a \hat{a} \cdot h_{a'} \bar{\bar{G}}^{A,F}(\mathbf{r}_c, \mathbf{r}_c') \hat{a}' da' db' dadb \end{aligned} \quad (72)$$

where \mathbf{r}_c and \mathbf{r}_c' is the position vectors of the centers of the two cells. These approximations are implemented inside “Eval_ind.m”.

2) Equivalent partial coefficients of potential Pp

Similarly as the partial inductance, the mutual term of Pp can also be significantly smaller than the self term when the $d2s$ becomes larger. For the electric cells on the side walls, the criteria, for the mutual term being 10^{-4} of the self term, is $d2s > 2$. The mutual term thus can be set to 0 under this criterion. For the electric cells on the via surface, the criterion is $d2s > 4$. The mutual term between the cell on the via surface and the one on the side walls are all below 10^{-6} of the self term.

The point-to-point approximation can be used for the magnetic capacitance cell in the antipad region. The criterion is $d2s > 1.5$ and the approximation is expressed as

$$Pp = \frac{1}{\varepsilon, \mu} \int_a \int_b \int_{a'} \int_{b'} \frac{1}{16} G^{q,q_m}(\mathbf{r}, \mathbf{r}') da' db' dadb \approx \frac{1}{\varepsilon, \mu} G^{q,q_m}(\mathbf{r}_c, \mathbf{r}_c'). \quad (73)$$

These approximations are implemented inside “Eval_cap.m”.

3) EM coupling term

If all the current directions in one cell are parallel to the ones inside the other cell, the EM coupling term is zero.

When $d2s > 2$ and the current of the electric cell is not in z direction, the absolute value of EM coupling term is smaller than 10^{-5} and can be ignored as well.

F. Create SPICE Netlist File

After get all the equivalent circuit elements, SPICE netlist file is created. The naming rule of the nodes and elements in the inductance branch is shown in Fig. 20 using the electric circuit as an example. The magnetic circuit is similarly created.

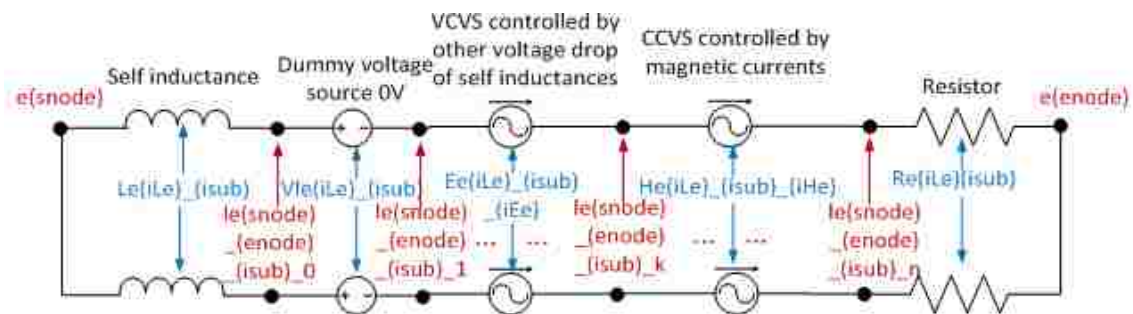


Fig. 20 Illustration of naming rule of the inductance branch

Notes for Fig. 20:

- Dummy voltage source (0V) is inserted for the CCVS definition in other inductance branches, for magnetic circuits with excitations, this voltage source has the corresponding value
- Red shows the node definition:
 - “le” means electric inductance
 - “snode” means node index of the starting node
 - “enode” means node index of the ending node

- n+1 additional circuit nodes are inserted between the starting and ending nodes depending on the number of the CCVS terms and VCVS terms
- Blue shows the circuit element definition:
 - “iLe” is the index of inductance cell
 - “iEe” is the index of VCVS, will increase by 1 for any additional controlled source
 - “iHe” is the index of CCVS, will increase by 1 for any additional controlled source
- Resistor equals to 0 for lossless case and magnetic circuit
- “isub” is the index of the sub cell

The self inductance, the coefficients for the VCVS and CCVS are expressed as

$$\begin{aligned}
 L_{self} &= L_{pe}\{iLe, iLe\}(isub, isub) \\
 E_{ee} &= \frac{L_{pe}\{iLe, jLe\}(isub, jsub)}{L_{pe}\{jLe, jLe\}(jsub, jsub)} \cdot \\
 H_{em} &= -EM\{jLm, iLe\}(jsub, isub)
 \end{aligned} \tag{74}$$

The inductance branch creation is implemented in “write_Lmut_EM.m” and ”write_Lself.m”.

The naming rule of the nodes and elements in the inductance branch is shown in Fig. 21 using the electric circuit as an example. The creation of the magnetic circuit is similar.

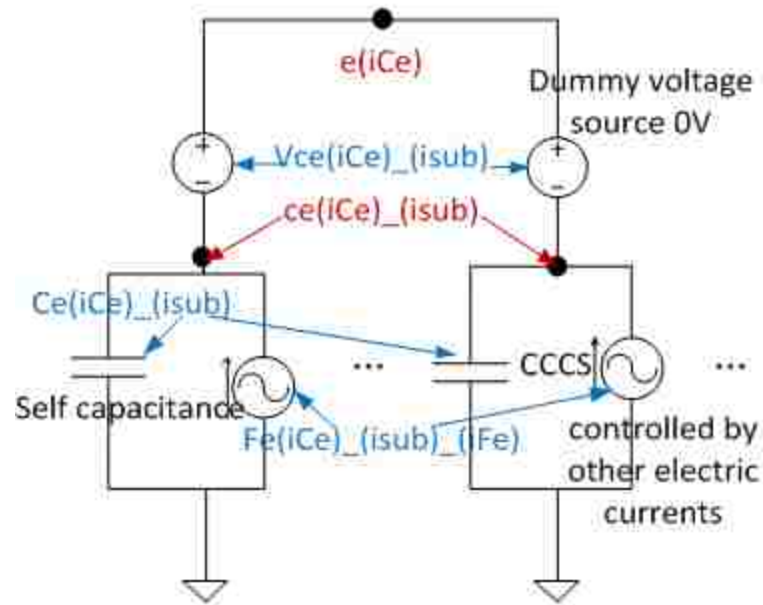


Fig. 21 Illustration of naming rule of the capacitance branch

Notes for Fig. 21:

- Dummy voltage source (0V) is inserted for the CCCS definition in other capacitance branches.
- Red shows the node definition:
 - “ce” means electric capacitance;
 - “iCe” is the node index .
- Blue shows the circuit element definition:
 - “iFe” is the index of CCCS, will increase by 1 for any additional controlled source.
- “isub” is the index of the sub cell.

The self capacitance, the coefficient for the CCCS is expressed as

$$C_{self} = \frac{1}{Pne\{iCe, iCe\}(isub, isub)}$$

$$F_{ee} = \frac{Pne\{iCe, jCe\}(isub, jsub)}{Pne\{iCe, iCe\}(isub, isub)}$$
(75)

The capacitance branch creation is implemented in “write_C.m”. “create_sp_files.m” is the main function to create the SPICE netlist files. The batch running of the SPICE netlist files are implemented in “run_sp.m”.

REFERENCES

- [1] Kam, D.G.; Ritter, M.B.; Beukema, T.J.; Bulzacchelli, J.F.; Pepeljugoski, P.K.; Kwark, Y.H.; Lei Shan; Xiaoxiong Gu; Baks, C.W.; John, R.A.; Hougham, G.; Schuster, C.; Rimolo-Donadio, R.; Boping Wu; , "Is 25 Gb/s On-Board Signaling Viable?," *Advanced Packaging, IEEE Transactions on* , vol.32, no.2, pp.328-344, May 2009.
- [2] V. Stojanovic and M. Horowitz, “Modeling and analysis of high-speed links,” in *Proc. IEEE Custom Integr. Circuits Conf.*, 2003, pp. 589–594.
- [3] C. Schuster, Y. H. Kwark, G. Selli, and P. Muthana, “Developing a physical model for vias,” in *Proc. IEC Designcon Conf.*, Santa Clara, CA, Feb. 2006, pp. 1–24.
- [4] G. Selli, C. Schuster, Y. Kwark, M. Ritter, and J. L. Drewniak, “Model-to-hardware correlation of physics based via models with the parallel plate impedance included,” in *Proc. IEEE Electromagn. Compat. Symp.*, Portland, OR, Aug. 2006, pp. 781–785.
- [5] S. Pan, J. Fan, and J. L. Drewniak, “Equivalent characteristic impedance and propagation constant for multi-layer via structures,” *2009 International Symposium on Electromagnetic Compatibility*, Kyoto, Japan, July 20-24, 2009.
- [6] Siming Pan; Jun Fan; , "Equivalent mixed-mode characteristic impedances for differential signal vias," *Electromagnetic Compatibility, 2009. EMC 2009. IEEE International Symposium on* , vol., no., pp.74-79, 17-21 Aug. 2009.
- [7] Yao-Jiang Zhang; Jun Fan; , "A Generalized Multiple Scattering Method for Dense Vias With Axially Anisotropic Modes in an Arbitrarily Shaped Plate Pair," *Microwave Theory and Techniques, IEEE Transactions on* , vol.60, no.7, pp.2035-2045, July 2012.
- [8] B. Wu and L. Tsang, "Full-wave modeling of multiple vias using differential signaling and shared antipad in multilayered high speed vertical interconnects," *Progress In Electromagnetics Research*, Vol. 97, 129-139, 2009.
- [9] Yao-Jiang Zhang; Jun Fan; , "An Intrinsic Circuit Model for Multiple Vias in an Irregular Plate Pair Through Rigorous Electromagnetic Analysis," *Microwave Theory and Techniques, IEEE Transactions on* , vol.58, no.8, pp.2251-2265, Aug. 2010.
- [10] Ruehli, A.E.; , "Equivalent Circuit Models for Three-Dimensional Multiconductor Systems," *Microwave Theory and Techniques, IEEE Transactions on* , vol.22, no.3, pp. 216- 221, Mar 1974.
- [11] G. T. Lei, R. W. Techentin, P. R. Hayes, D. J. Schwab, and B. K. Gilbert, “Wave model solution to the ground/power plane noise problem,” *IEEE Trans. Instrum. Meas.*, vol. 44, no. 2, pp. 300–303, Apr. 1995.

- [12] G. Antonini, S. Cristina, and A. Orlandi, "PEEC modeling of lightning protection system and coupling to coaxial cables," *IEEE Trans. Electromagn. Compat.*, vol. 40, pp. 481–491, Nov. 1998.
- [13] J. Fan, H. Shi, A. Orlandi, J. L. Knighten, and J. L. Drewniak, "Modeling DC power-bus structures with vertical discontinuities using a circuit extraction approach based on a mixed-potential intergral equation formulation," *IEEE Trans. Adv. Packag.*, vol. 24, pp. 143–157, May 2001.
- [14] B. Archambeault and A. E. Ruehli, "Analysis of power/ground-plane EMI decoupling performance using the partial-element equivalent circuit technique," *IEEE Trans. Electromagn. Compat.*, vol. 43, pp. 437–445, Nov. 2001.
- [15] W. Pinello, A. C. Cangellaris, and A. E. Ruehli, "Hybrid electromagnetic modeling of noise interactions in packaged electronics based on the partial-element equivalent circuit formulation," *IEEE Trans. Microwave Theory Tech.*, vol. 45, pp. 1889–1896, Oct. 1997.
- [16] Gang Feng; Jun Fan; , "An Extended Cavity Method to Analyze Slot Coupling Between Printed Circuit Board Cavities," *Electromagnetic Compatibility, IEEE Transactions on* , vol.53, no.1, pp.140-149, Feb. 2011.
- [17] Gope, D.; Ruehli, A.E.; Chuanyi Yang; Jandhyala, V.; , "(S)PEEC: Time- and frequency-domain surface formulation for modeling conductors and dielectrics in combined circuit electromagnetic simulations," *Microwave Theory and Techniques, IEEE Transactions on* , vol.54, no.6, pp.2453-2464, June 2006.
- [18] Ruehli, A.E.; Antonini, G.; Esch, J.; Ekman, J.; Mayo, A.; Orlandi, A.; , "Nonorthogonal PEEC formulation for time- and frequency-domain EM and circuit modeling," *Electromagnetic Compatibility, IEEE Transactions on* , vol.45, no.2, pp. 167-176, May 2003.
- [19] Kai Yang; Ke-Li Wu; , "Generalized Partial-Element Equivalent-Circuit Analysis for Planar Circuits With Slotted Ground," *Microwave Theory and Techniques, IEEE Transactions on* , vol.57, no.7, pp.1734-1742, July 2009.
- [20] Myun-Joo Park; Jongkuk Park; Sangwook Nam; , "Efficient calculation of the Green's function for the rectangular cavity," *Microwave and Guided Wave Letters, IEEE* , vol.8, no.3, pp.124-126, Mar 1998.
- [21] Kustepeli, A.; Martin, A.Q.; , "On the splitting parameter in the Ewald method," *Microwave and Guided Wave Letters, IEEE* , vol.10, no.5, pp.168-170, May 2000.
- [22] Notaros, B.M.; , "Higher Order Frequency-Domain Computational Electromagnetics," *Antennas and Propagation, IEEE Transactions on* , vol.56, no.8, pp.2251-2276, Aug. 2008.
- [23] Borji, A.; Safavi-Naemi, S.; , "Fast convergent Green's function in a rectangular enclosure," *Antennas and Propagation Society International Symposium, 2003. IEEE* , vol.4, no., pp. 950- 953 vol.4, 22-27 June 2003.
- [24] I. Hanninen, M. Taskinen, and J. Sarvas, "Singularity subtraction integral formulae for surface integral equations with rwg, rooftop and hybrid basis functions," *Progress In Electromagnetics Research*, Vol. 63, 243-278, 2006.
- [25] ANSYS HFSS 13. [Online]. Available: <http://www.ansys.com/Products/Simulation+Technology/Electromagnetics/High-Performance+Electronic+Design/ANSYS+HFSS>.

[26] Constantine A. Balanis, Advanced Engineering Electromagnetics, John Wiley and Sons, pp.255-259. USA. 1989.

III. Estimating Radio-Frequency Interference to an Antenna Due to Near-Field Coupling Using Divide-and-Conquer Method Based on Reciprocity

Hanfeng Wang, *Student Member, IEEE*, Victor Khilkevich, *Member, IEEE*, Yao-Jiang Zhang, *Senior Member, IEEE*, and Jun Fan, *Senior Member, IEEE*

Abstract— In mixed radio-frequency (RF) and digital designs, noise from high-speed digital circuits can interfere with RF receivers, resulting in RF interference issues such as receiver desensitization. In this paper, an effective methodology is proposed to estimate the RF interference received by an antenna due to near-field coupling, which is one of the common noise coupling mechanisms, using divide-and-conquer based on reciprocity. The proposed methodology is validated through comparisons with full-wave simulations, fits well with engineering practice, and is particularly suitable for pre-layout wireless system design and planning.

Index Terms— Divide-and-conquer, mixed RF/digital design, near-field coupling to antenna, pre-layout system design and planning, radio-frequency interference, reciprocity.

I. INTRODUCTION

As a special type of intra-system electromagnetic compatibility (EMC) problem, radio-frequency (RF) interference from digital circuits to RF receivers is becoming increasingly critical in the design of mixed RF/digital systems, such as notebook PCs, cell phones, portable media players, etc. [1], due to the increasing speed in digital integrated circuits (ICs) and the decreasing form factor of the systems.

There are many possible mechanisms for digital noise to couple to RF receivers. RF antennas/receivers can pick up digital noise through direct field coupling inside a metal chassis, such as from high-speed printed circuit board (PCB) traces, connectors, flex cables, and integrated circuit (IC) heat sinks. Digital noise can also couple to RF

antennas/receivers through power distribution networks and other conducted paths such as chassis and ground planes.

In this study, the focus is on the direct field coupling from a digital noise source to an RF antenna, as shown in Fig. 1. Similar to a conventional noise-coupling problem [2], there are three major components: digital IC as the noise source, electromagnetic field coupling as the noise coupling mechanism, and RF antenna as the victim. Due to the small dimensions in many mixed RF/digital systems, such noise coupling could occur in the near-field region. The main contribution of this paper is to propose an efficient method to estimate the near-field coupling for RF interference evaluations.

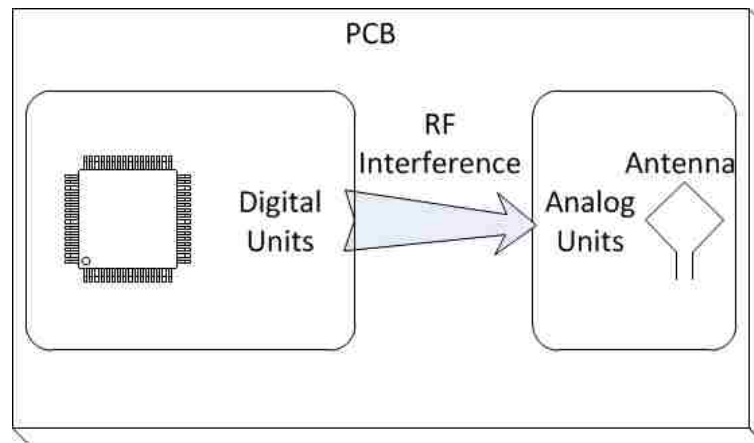


Fig. 1 RF interference from digital units to analog units

When the noise coupling occurs in the far field region, some conventional antenna theories can be used to estimate the induced noise power at the RF antenna port by treating the digital noise source as a transmitting “antenna”, such as the Friis transformation equation as [3]

$$\frac{P_r}{P_t} = e_{cdt} e_{cdr} (1 - |\Gamma_t|^2) (1 - |\Gamma_r|^2) \left(\frac{\lambda}{4\pi R} \right)^2 D_t(\theta_t, \phi_t) D_r(\theta_r, \phi_r) |\hat{\mathbf{p}}_t \cdot \hat{\mathbf{p}}_r|^2, \quad (1)$$

where P_r , P_t are the receiving power of the RF antenna and the transmitting power of the noise-source “antenna”, respectively; e_{cdr} and e_{cdt} are their radiation efficiency; Γ_r and Γ_t are the reflection coefficients looking into the load and looking into the noise source “antenna” at the antenna ports, respectively; λ is the wavelength; R is the distance between the two antennas; D_r and D_t are the directivity of the two antennas; and, $\hat{\mathbf{p}}_r$ and $\hat{\mathbf{p}}_t$, are the polarization unit vectors of the two antennas. The Friis transformation equation is a straightforward way to evaluate the receiving power (noise power in this case) at the RF antenna port. However, it only works for the far-field coupling. In compact mobile devices, the coupling between the IC noise source and the RF antenna is mostly in the near-field region. Thus, the Friis transformation is not suitable anymore for this kind of problem, which will be demonstrated using numerical simulations in Section IV.

Then, to estimate the noise power coupled to the RF antenna port from the digital circuit in near-field region, full-wave simulation of the entire structure including the noise source, the RF receiving antenna, and all the relevant scatters/materials is the straightforward, brute-force solution. However, this approach is not suitable for practical applications such as the pre-layout system design and optimization in terms of the minimized RF interference. A more practical strategy is to generate “libraries” for digital noise source (IC) and antenna models, where interference estimation between the noise source and antenna models in a specific mechanical design can be efficiently obtained without the need to run lengthy full-wave simulations whenever a model, its location, or a mechanical feature changes.

In this paper, a divide-and-conquer method based on reciprocity is introduced for estimating the received digital noise power at the RF antenna port, which fits very well with the engineering practice described earlier. First, a Huygens box is introduced to enclose the RF antenna so that it can be removed from the original structure. Then, the tangential electromagnetic fields on the Huygens box for the original structure with the RF antenna removed are obtained through a full-wave simulation (the noise source model obtained in [4] or similar ones can be used as the excitation). Next, the RF antenna alone is simulated as a transmitting antenna and the tangential electromagnetic fields on the same Huygens box are obtained. In other words, an antenna model is generated. Lastly, the induced noise power at the RF antenna port is obtained by using the two sets of the tangential electromagnetic fields on the Huygens box based on the reciprocity theorem. The benefit of the proposed method is that the noise source and the antenna models remain the same as long as the same digital ICs and the same RF antenna are used. When component position changes or other mechanical design changes, only the electromagnetic fields on the Huygens box due to the noise source need to be recalculated, which hopefully is more efficient and faster than the full-wave simulation of the entire structure. Similarly, if several antenna designs are to be evaluated and compared, only individual antenna models need to be constructed (all other steps only need to be run once). This makes the pre-layout design and optimization more flexible and efficient.

II. DIVIDE AND CONQUER METHOD

A simplified model in Fig. 2 is used to illustrate the divide and conquer method. Two small probes are created above a large ground plane. The dimensions of the ground

plane are 4"x 2", and the distance between the two probes is 2000 mils. The ground plane has a thickness of 1 mil and the probes have a height of 100 mils. Two ports are defined between the probes and the ground plane for either excitation or termination. One probe is used to represent a simplified digital noise source and the other probe represents an RF antenna.

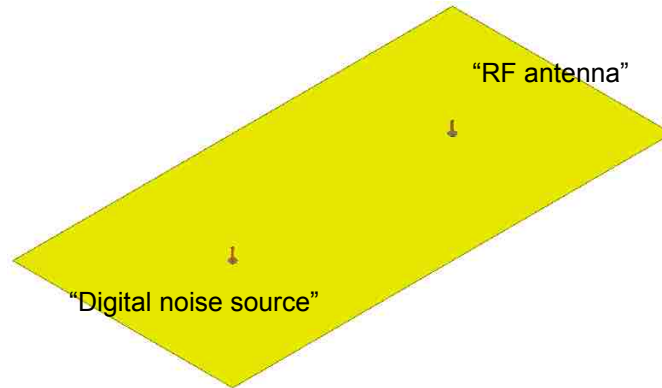
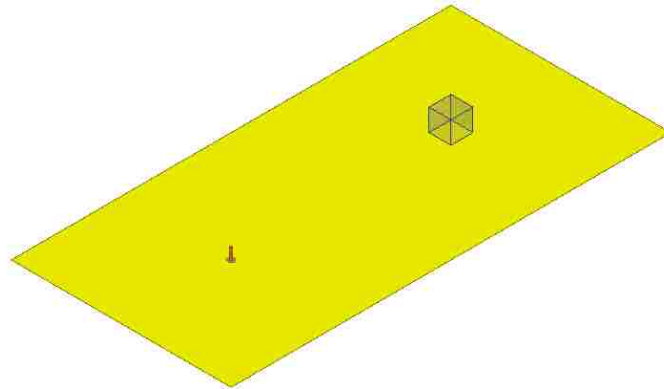


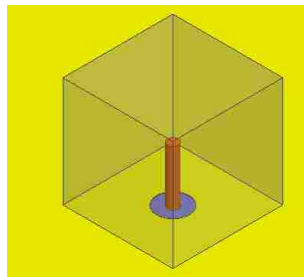
Fig. 2. Simplified model to illustrate the divide-and-conquer method

The ultimate goal is to estimate the induced noise power on the “RF antenna” port generated from the “digital noise source”. One straightforward way to estimate this induced noise on the antenna port is to run the simulation of the entire model in a full-wave simulation tool such as HFSS [5]. For the reasons discussed earlier, an alternative method is proposed herein. In this method, the entire geometry is divided into two parts by creating an observation box that surrounds the “RF antenna”, as shown in Fig. 3. The observation box is a cubic with a side length of 200 mils in this example. Then, the original structure with the “RF antenna” removed, as shown in Fig. 3(a), is studied, and simulated using HFSS in this work, to obtain the tangential electromagnetic fields on the observation box. This set of the tangential fields will be used as the excitation to the “RF antenna” when it is in the receiving mode. The step to calculate the antenna output using

the field excitation is referred to as the “forward” problem herein. Next, as shown in Fig. 3(b), only the “RF antenna” is studied as a transmitting antenna, again using HFSS in this work, to obtain the tangential electromagnetic fields on the same observation box. This step is referred to as the “reverse” problem herein. The induced noise output at the “RF antenna” can then be calculated from these two sets of tangential electromagnetic fields on the observation box. The detailed algorithm will be introduced in the following section.



(a) Part 1 including “Digital noise source” and coupling path



(b) Part 2 including “RF antenna” only

Fig. 3. Divide the whole model into two parts

III. RECIPROCITY THEOREM AND INTERFERENCE ESTIMATION

An efficient and fast method of calculating transfer functions between equivalent current sources and antenna was introduced in [6] based on the reciprocity theorem. In this work, similar derivations are extended to calculate the induced antenna output from

the two sets of the tangential electromagnetic fields on the observation box obtained using the divide and conquer method.

The reciprocity theorem can be expressed using the field and source quantities in the forward and reserve problems as [7]

$$\begin{aligned} & -\int_S (\bar{\mathbf{E}}^{rev} \times \bar{\mathbf{H}}^{fwd} - \bar{\mathbf{E}}^{fwd} \times \bar{\mathbf{H}}^{rev}) \cdot d\mathbf{s} \\ & = \int_V (\bar{\mathbf{E}}^{rev} \times \bar{\mathbf{J}}^{fwd} + \bar{\mathbf{H}}^{fwd} \times \bar{\mathbf{M}}^{rev}) dV - \int_V (\bar{\mathbf{E}}^{fwd} \times \bar{\mathbf{J}}^{rev} + \bar{\mathbf{H}}^{rev} \times \bar{\mathbf{M}}^{fwd}) dV, \end{aligned} \quad (2)$$

where $\bar{\mathbf{J}}$ is the electric current source and $\bar{\mathbf{M}}$ is the magnetic current source. The superscript denotes the problem type, “*fwd*” for the forward problem and “*rev*” for the reverse one. If the integral is evaluated over the entire space (which means the boundary surface S is at infinity), the left side of (2) is zero. Thus, (2) can simplified as

$$\int_V (\bar{\mathbf{E}}_c^{rev} \cdot \bar{\mathbf{J}}_c^{fwd} - \bar{\mathbf{H}}_c^{rev} \cdot \bar{\mathbf{M}}_c^{fwd}) dV = \int_V (\bar{\mathbf{E}}_a^{fwd} \cdot \bar{\mathbf{J}}_a^{rev} - \bar{\mathbf{H}}_a^{fwd} \cdot \bar{\mathbf{M}}_a^{rev}) dV, \quad (3)$$

where the subscript denotes the location of the source and field quantities: “*c*” for cells on observation box and “*a*” for the RF antenna port. Therefore, in the reverse problem, sources at the antenna port are defined as $\bar{\mathbf{J}}_a^{rev}$ and $\bar{\mathbf{M}}_a^{rev}$, and the resulting fields on the observation box are defined as $\bar{\mathbf{E}}_c^{rev}$ and $\bar{\mathbf{H}}_c^{rev}$. In the forward problem, equivalent sources on the observation box are defined as $\bar{\mathbf{J}}_c^{fwd}$ and $\bar{\mathbf{M}}_c^{fwd}$, and the resulting fields on the antenna port are defined as $\bar{\mathbf{E}}_a^{fwd}$ and $\bar{\mathbf{H}}_a^{fwd}$.

The electric term at the left side of (3) can be derived as

$$\int_V \bar{\mathbf{J}}_c^{fwd} \cdot \bar{\mathbf{E}}_c^{rev} dV = \int_{S_c} \bar{\mathbf{J}}_c^{fwd} \cdot \bar{\mathbf{E}}_c^{rev} dS = \sum_{cells} \bar{\mathbf{J}}_c^{fwd} \cdot \bar{\mathbf{E}}_c^{rev} S_{cell} = \sum_{cells} \hat{\mathbf{n}} \times \bar{\mathbf{H}}_c^{fwd} \cdot \bar{\mathbf{E}}_c^{rev} S_{cell}, \quad (4)$$

where S_c is the surface of the observation box. The volume integral becomes a surface integral since the equivalent electric current densities in (4) only reside on the surface of

the observation box. If the surface of the box is meshed into uniform square cells, and the meshed cells are small enough so that the fields are approximately uniform inside each cell, the integral can be transformed into summations where S_{cell} is the area of each mesh cell. Finally, the equivalent electric current densities on the surface of the observation box can be calculated from the H-field, where \hat{n} is the inward unit vector normal to the surface of the observation box.

Similarly, the magnetic term at the left side of (3) can be derived as

$$\int_V \bar{M}_c^{fwd} \cdot \bar{H}_c^{rev} dv = \int_{S_c} \bar{M}_c^{fwd} \cdot \bar{H}_c^{rev} ds = \sum_{cells} \bar{M}_c^{fwd} \cdot \bar{H}_c^{rev} S_{cell} = \sum_{cells} \bar{E}_c^{fwd} \times \hat{n} \cdot \bar{H}_c^{rev} S_{cell} . \quad (5)$$

The electric term at the right side of (3) can be derived similarly as in [8] as

$$\int_V \bar{E}_a^{fwd} \cdot \bar{J}_a^{rev} dv = - \int_{S_a} \bar{E}_a^{fwd} J_a^{rev} ds = -I_a^{rev} U_a^{fwd} , \quad (6)$$

where the volume integral is transformed into a surface integral at the antenna port surface. The negative sign is because \bar{E}_a^{fwd} and \bar{J}_a^{rev} have opposite directions. S_a is the cross-sectional surface of the antenna port. U_a^{fwd} and I_a^{rev} are the voltage and current at the antenna port in the forward and reverse problems, respectively.

The magnetic term at the right side of (3) is first converted to an electric term as

$$\int_V \bar{H}_a^{fwd} \cdot \bar{M}_a^{rev} dv = \int_V (\bar{E}_a^{rev} \times \hat{n}) \cdot \bar{H}_a^{fwd} dv = \int_V \bar{E}_a^{rev} \cdot (\hat{n} \times \bar{H}_a^{fwd}) dv = \int_V \bar{E}_a^{rev} \cdot \bar{J}_a^{fwd} dv . \quad (7)$$

Then (7) can be similarly derived as in (6) as

$$\int_V \bar{E}_a^{rev} \cdot \bar{J}_a^{fwd} dv = \int_{S_a} J_a^{fwd} E_a^{rev} ds = I_a^{fwd} U_a^{rev} , \quad (8)$$

Substituting (4)~(8) back into (3) results in

$$\sum_{cells} \bar{n} \times \bar{H}_c^{fwd} \cdot \bar{E}_c^{rev} S_{cell} + \sum_{cells} \bar{n} \times \bar{E}_c^{fwd} \cdot \bar{H}_c^{rev} S_{cell} = -I_a^{rev} U_a^{fwd} - I_a^{fwd} U_a^{rev} = - \left(\frac{1}{Z_{in}} + \frac{1}{Z_L} \right) U_a^{fwd} U_a^{rev} , \quad (9)$$

where Z_{in} is the input impedance of the RF antenna in the transmitting mode in the reverse problem; Z_L is the load impedance at the antenna port in the receiving mode (50 Ω in our case) in the forward problem. U_a^{rev} is the excitation voltage of the RF antenna in the transmitting mode (1 V in our case). From (9), the voltage induced at the RF antenna port, U_a^{fwd} , can be solved from the tangential E and H fields on the observation box in both the reverse and the forward problems.

It needs to point out that the simple divide and conquer method proposed in this work assumes the multiple scattering effect between the noise source and the RF antenna is negligible.

IV. RESULTS AND VALIDATIONS

A. *Simple model*

The simple probe model in Fig. 2 is firstly used to prove the necessity of the study of near-field coupling. The Friis transformation equation [3] is used to estimate the induced power at the port of the receiving “RF antenna”, and it will be shown that this equation only works when the noise-source antenna and the “RF antenna” are located sufficiently far away to each other.

In this example, since both the noise-source and the “RF” antennas have the same probe structure. Their parameters, such as the directivity, the gain and the input impedance, can be obtained by simulating one probe antenna alone in HFSS. The peak gain of the probe antenna is 2.97 and the input impedance is (3.719-161.5j) Ω . The peak gain is the multiplication of the peak directivity and the radiation efficiency. The reflection coefficient can be calculated as

$$|\Gamma| = \left| \frac{Z_{in} - 50}{Z_{in} + 50} \right|, \quad (10)$$

where Z_{in} is the input impedance of the probe antenna, assuming both probes are either terminated with a 50Ω load, or connected with a source with a 50Ω source resistance. Since the two probe antennas are aligned in their maximum radiation direction and are also polarization-matched, the receiving power at the “RF antenna” can be easily calculated from (1). A sinusoidal wave of magnitude of 1 V is assumed as the source voltage for the transmitting antenna in the results shown below.

Meanwhile, the power induced at the port of the receiving antenna can also be obtained from the full wave simulation of the entire structure with both probes, and from the proposed divide-and-conquer method using (9). The mesh size on the observation box, when using the proposed method, is 5 mils, which was found to be a sufficiently small number to obtain the converged results in this example. The results of the three methods are compared in Table I, with the distance between the two probes changing from 500 mils to 2000 mils.

Table I
Comparison of Friis Transformation, Full-wave Simulation, and the proposed divide-and-conquer method

Distance (mils)	Friis Transformation Equation (dBm)	Full-wave Simulation (dBm)	Proposed Method (dBm)
2000	-98.5	-99.7	-99.7
1000	-86.4	-90.7	-90.7
500	-74.4	-79.0	-79.0

It can be clearly seen that the difference between the Friis transformation and the full-wave simulation becomes larger when the distance between the two probes becomes smaller. That means the Friis transformation equation can only be used to estimate the receiving power for far-field coupling. However, for the RF interference problems in compact mobile devices, near-field coupling could be dominant. Then, the Friis transformation is no longer suitable in these cases. The results of the direct full wave simulation and the proposed divide-and-conquer method show a strong agreement for all the cases. The frequency under study in this example is 10 GHz.

Further, the same model in Fig. 2, when the distance between the two probes is 1000 mils, is used to validate the proposed method at different frequencies. The induced power at the receiving antenna port at each frequency point was calculated using (9) first, and then obtained from the full-wave simulation of the entire structure. The two sets of results are compared at 10 different frequency points from 1 GHz to 10GHz in Fig. 4.

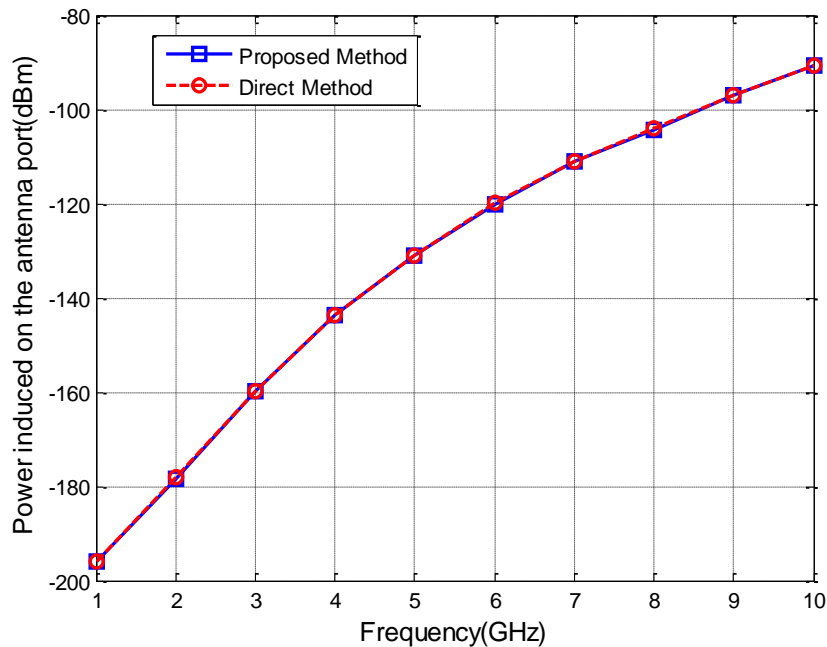


Fig. 4. Output power comparison between the proposed method and the direct full-wave simulation for the simplified model shown in Fig. 2

The calculated results using the proposed method show good agreement of the induced noise power at the RF antenna port with those from the direct simulation of the original geometry. Since the probe is very small compared to the wavelength, the simulated frequency range excludes the resonant frequency of the antenna. Thus, the coupled power to the antenna port is very small. Two more practical examples are used to validate the proposed method in the following subsections.

B. *Trace+ PIFA*

A more practical case, with a section of microstrip trace and a Planar Inverted-F Antenna (PIFA) [9], is shown in Fig. 5. The ground plane size is 4"x2" and the thickness of the plane is 1 mil. The patch of the PIFA has dimensions of 500 mils x 500 mils and is 10 mils above the ground plane. The radius of the short via and feeding probe of the PIFA is 10 mils, and the antipad radius of the feeding port is 30 mils. The trace (digital

noise source) is excited with a 1 V voltage source with a 50Ω source resistance at one end and terminated with a 50Ω at the other end. The detailed dimensions for the trace can be found in [4]. The distance between the trace and the PIFA is 2000 mils. This example represents a typical near-field coupling problem from a digital trace to an RF antenna in modern mobile devices.

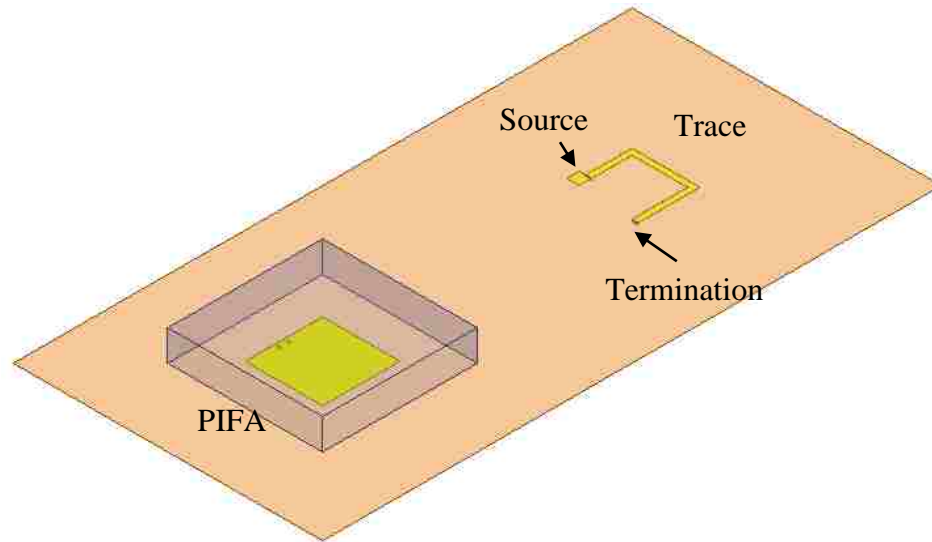


Fig. 5. Near-field coupling from a microstrip trace to a PIFA antenna

The proposed divide-and-conquer method is used to calculate the induced power at the PIFA port. An observation box with the dimensions of 1000 mils x 1000 mils x 200 mils is created to enclose the PIFA antenna. The mesh size on the observation box is 10 mils. The calculated power is validated through the comparisons with the full-wave simulation of the entire structure, as shown in Fig. 6.

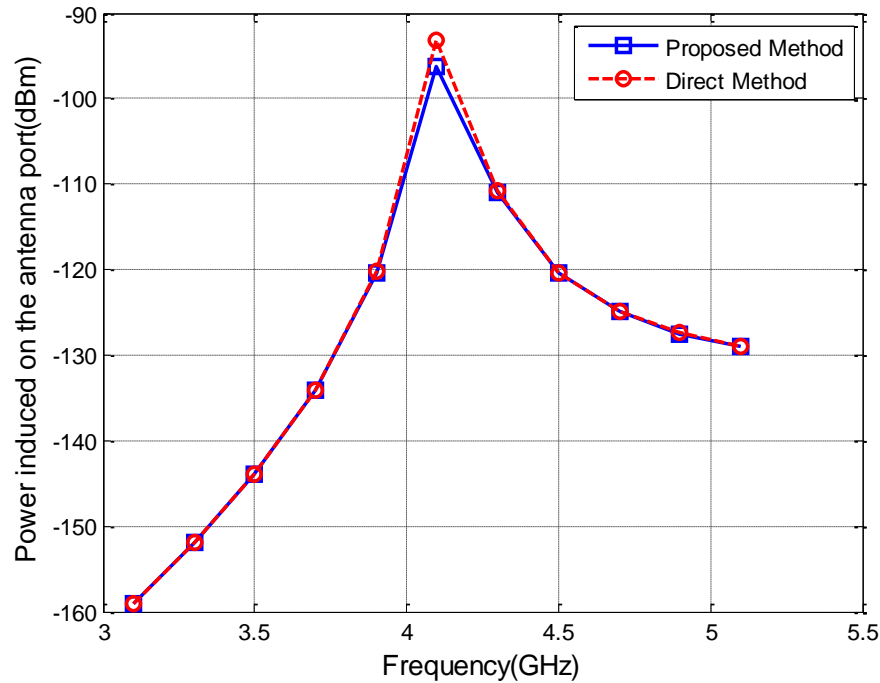


Fig. 6. Output power comparisons between the proposed method and the direct method for the trace+PIFA structure shown in Fig. 5

The agreement between the two methods is excellent in general in the entire frequency range from 3.1 GHz to 5.1 GHz, with some small discrepancies close to 4.1 GHz, the resonant frequency of the PIFA antenna.

Several factors that may influence the accuracy of the proposed divide-and-conquer method are studied as well. Based on the derivation of the reciprocity theorem, the observation box only needs to be big enough to enclose the RF antenna. Numerical experiments have also validated this conclusion. The distance between the noise source and the antenna is varied, and results have shown excellent agreement of the proposed method compared with the full-wave simulation of the entire structure, even for the very closely coupled cases as long as the noise source does not influence the radiation pattern of the antenna and the multiple scattering effects between the noise source and the antenna can be neglected. The mesh size on the observation box has been found very

critical for the proposed method. Since the integral is approximated using the summation, the tangential components of the fields need to be approximately constant in each mesh cell. Thus, the size of the mesh cell is determined by both the wavelength and the variation of the fields on the observation box. The mesh cell size needs to be smaller than $1/10$ of the wavelength. Furthermore, if the box is at the very near field of the antenna (meaning the field is changing dramatically on the surface of the box), the mesh cell size needs to be further smaller.

C. *DECT + IC*

The last example to validate the proposed method is extracted from a real product [10]. The near-field coupling between a Digital Enhanced Cordless Telecommunications (DECT) antenna and an IC is studied as shown in Fig. 7. The DECT antenna is on the edge of a printed circuit board and one I/O port of the IC is excited as the noise source. The detailed dimensions of the DECT antenna are shown in Fig. 8, and the thickness of the antenna is 0.018mm. The distance between the center of the IC to the DECT antenna is 49.5 mm. The size of the die of the IC is 3.6 x 11 mm, and it has 27 x 2 pins. The detailed modeling information of the IC is described in [10]. The induced power on the DECT antenna port is evaluated using both the proposed divide-and-conquer method and the full-wave simulation method of the entire structure. The dimensions of the observation box enclosing the DECT antenna are 14 mm x 44 mm x 14 mm, and the mesh size on the observation box is 1 mm. The results are compared in Fig. 9.

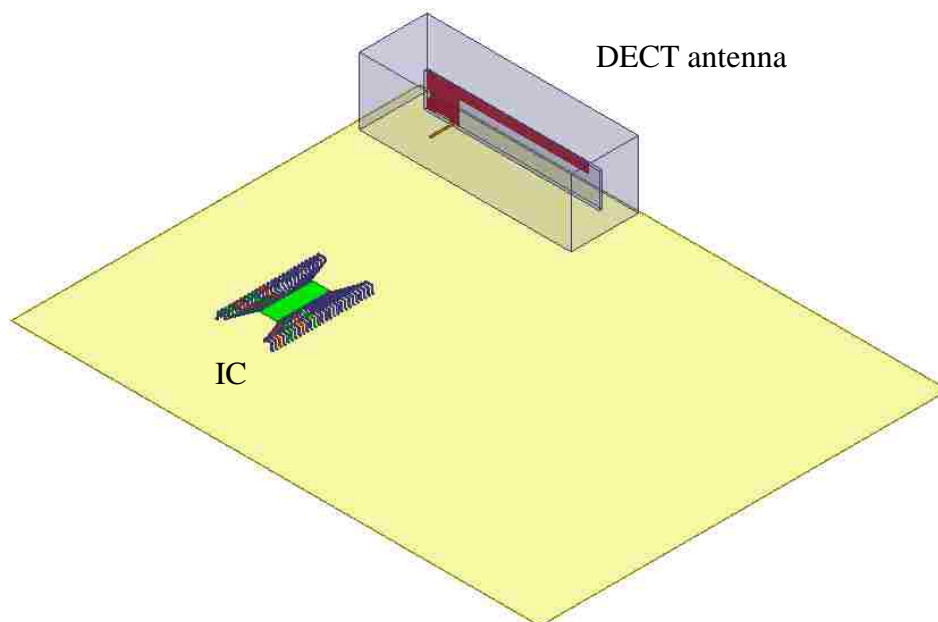


Fig. 7 Near-field coupling from an IC to a DECT antenna on a real printed circuit board

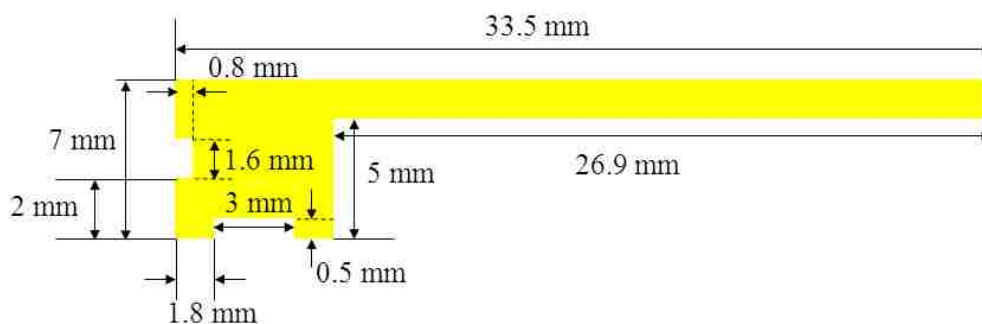


Fig. 8. Detailed dimensions of the DECT antenna

The resonant frequency of the DECT antenna is 1840 MHz. The results of the output power at the antenna port from the two methods from 1340 MHz to 2340 MHz with a 100 MHz step are compared in Fig. 9. The results again show excellent agreement, which demonstrates that the proposed method is valid even when the antenna is at the edge of the board.

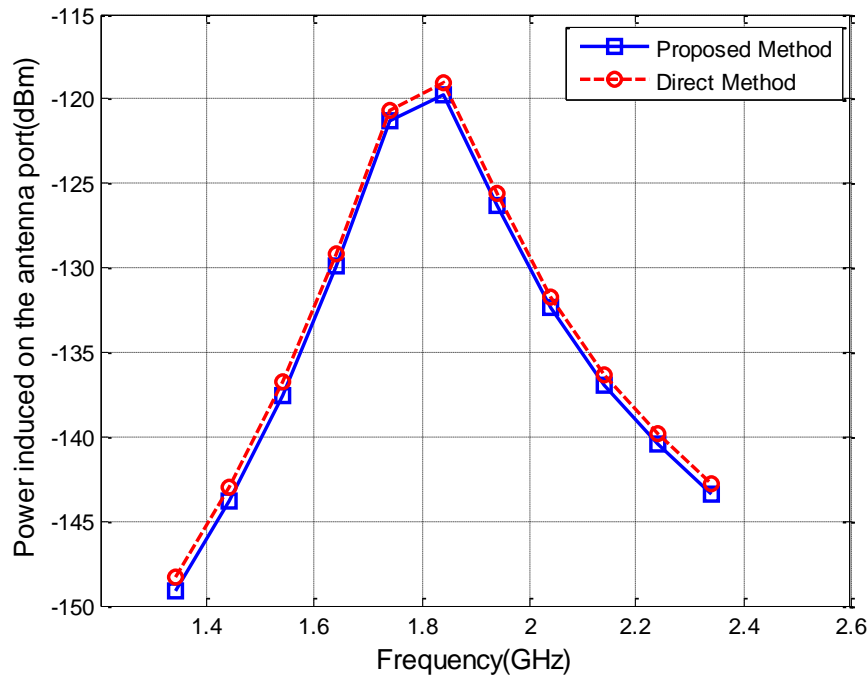


Fig. 9. Output power comparisons between the proposed method and the direct method for the DECT+IC structure shown in Fig. 7.

V. CONCLUSIONS

A divide-and-conquer method is introduced for estimating the near-field noise coupling from a digital noise source to an RF antenna. The reciprocity theorem is used to obtain the antenna noise output based on the modeling of the forward and reverse problems. Three examples, from a simplified model to a practical model extracted from a real product, are used to validate the proposed method. The calculated results using the divide-and-conquer method based on the reciprocity theorem show excellent agreement of the induced noise at the RF antenna port with the direct full-wave simulations of the original geometry. The proposed method fits well with typical engineering practice, and can be used for efficient pre-layout design and optimization. The multiple scattering effects between the antenna and other scatters/sources in the system are neglected in this work.

ACKNOWLEDGMENT

The authors would like to thank Mr. Hongyu Li with the Electromagnetic Compatibility Laboratory, Missouri University of Science and Technology, Rolla, MO, for his kind support of providing the DECT+IC HFSS model for the noise coupling study in this paper.

REFERENCES

- [1] Kevin Slattery; Harry Skinner, *Platform Interference In Wireless Systems: Models, Measurement, and Mitigation*, Newnes, USA. 2008.
- [2] Clayton R. Paul, *Introduction to Electromagnetic Compatibility*, John Wiley & Sons, USA. 2006.
- [3] Constantine A. Balanis, *Antenna Theory: Analysis and Design, 3rd Edition*, John Wiley and Sons, pp.94-96. USA. 2005.
- [4] Zhenwei Yu; Jason A. Mix; Soji Sajuyigbe; Kevin P. Slattery; Jun Fan, “An Improved Dipole-Moment Model Based on Near-Field Scanning for Characterizing Near-Field Coupling and Far-Field Radiation from an IC”, *IEEE Trans. Electromagnetic Compatibility*, to be published.
- [5] ANSYS HFSS 13. [Online]. Available: <http://www.ansys.com/Products/Simulation+Technology/Electromagnetics/High-Performance+Electronic+Design/ANSYS+HFSS>.
- [6] V.Khilkevich, “An efficient and fast method of calculating transfer functions between equivalent current sources and antennas”, to be submitted.
- [7] Constantine A. Balanis, *Advanced Engineering Electromagnetics*, John Wiley and Sons, pp.323-325. USA. 1989.
- [8] J. H. Richmond, “A reaction theorem and its applications to antenna impedance calculations,” *IRE Trans. Antennas Propagat.*, vol. 9, pp. 515-520, Nov. 1961.
- [9] Kin-Lu Wong, *Planar Antennas for Wireless Communications*, John Wiley and Sons, pp.3-48. USA. 2003.
- [10] Hongyu Li, Victor Khilkevich, David Pommerenke, “Identification and Visualization of Electromagnetic Coupling Path – Part II: Practical Application”, to be submitted.

2. CONCLUSIONS

In the first paper of this dissertation an integral equation method based on partial capacitance is introduced in this paper to calculate the via-to-plane capacitance of different via structures. The axially symmetric structure is analyzed first and then the method is extended to the axially asymmetric via geometry. The image theory is used to deal with the inhomogeneous dielectric media which is common for PCB applications. The via-to-plane capacitances are extracted for several different via geometries and the results are validated with the finite element solution using Q3D. The accuracy of the proposed method is also validated through the comparison of the physics-based via modeling and the full wave simulation. The main advantage of the proposed capacitance calculation method is that very few mesh cells are needed which leads to a low computational time and memory cost.

In the second paper, a rigorous modeling method of a shared-antipad via structure is developed using surface PEEC with the cavity Green's function. The advantage of using the cavity Green's function is that much fewer mesh cells are needed for the via structure. The values of the equivalent circuit elements are derived based on the non-orthogonal mesh in the antipad region and the rectangular mesh on the via surface. In order to characterize the via transition parameters, a novel wave port excitation method is developed to stimulate the equivalent circuit.

The proposed method is validated using a commercial finite element solver. Strong correlation of Z-parameter results are achieved for both the traditional, simple one-via structure and the shared-antipad structure which, is widely used in differential via design.

The PEEC calculated by the proposed method can be further used to connect to either the parallel plane model or other transmission line models of the trace to do the circuit simulation of the whole system. Multiple PEEC's of the proposed method can also be stacked together to model the multi-layer PCB problems; this modeling can be the future work of this study of the second paper.

In the third paper, a divide-and-conquer method is introduced for estimating the near-field noise coupling from a digital noise source to an RF antenna. The reciprocity theorem is used to obtain the antenna noise output based on the modeling of the forward and reverse problems. Three examples, from a simplified model to a practical model extracted from a real product, are used to validate the proposed method. The calculated results using the divide-and-conquer method based on the reciprocity theorem show excellent agreement of the induced noise at the RF antenna port with the direct full-wave simulations of the original geometry. The proposed method fits well with typical engineering practice, and can be used for efficient pre-layout design and optimization. The multiple scattering effects between the antenna and other scatters/sources in the system are neglected in this work.

VITA

Hanfeng Wang was born in Wuxi, Jiangsu Province, P. R. China. He received the Bachelor of Science degree in Electronics Engineering (2005) and the Master of Science degree in Electronics Engineering (2008) from Tsinghua University, Beijing, P. R. China. He was a summer intern at Apple, Cupertino, CA, in 2010, and was a Co-op at Cisco, San Jose, CA, in 2011. His research interests include signal integrity, radio frequency interference mitigation, and electromagnetic modeling. In December, 2012, he received his Ph. D. in Electrical Engineering from Missouri University of Science and Technology.